

The Pennsylvania State University  
The Graduate School  
Department of Materials Science and Engineering

**TUNGSTEN DITELLURIDE (WTe<sub>2</sub>): AN ATOMIC LAYERED SEMIMETAL**

A Thesis in  
Materials Science and Engineering  
by  
Chia-Hui Lee

© 2015 Chia-Hui Lee

Submitted in Partial Fulfillment  
of the Requirements  
for the Degree of

Master of Science

December 2015

The thesis of Chia-Hui Lee was reviewed and approved\* by the following:

Joshua A. Robinson  
Professor of Materials Science and Engineering  
Thesis Advisor

Thomas E. Mallouk  
Head of the Chemistry Department  
Evan Pugh University Professor of Chemistry, Physics, Biochemistry and  
Molecular Biology

Mauricio Terrones  
Professor of Physics, Chemistry and Materials Science & Engineering

Suzanne Mohny  
Professor of Materials Science and Engineering and Electrical Engineering  
Chair, Intercollege Graduate Degree Program in Materials Science and  
Engineering

\*Signatures are on file in the Graduate School

## ABSTRACT

Tungsten ditelluride ( $\text{WTe}_2$ ) is a transition metal dichalcogenide (TMD) with physical and electronic properties that make it attractive for a variety of electronic applications. Although  $\text{WTe}_2$  has been studied for decades, its structure and electronic properties have only recently been correctly described. We explored  $\text{WTe}_2$  synthesis via chemical vapor transport (CVT) method for bulk crystal, and chemical vapor deposition (CVD) routes for thin film material. We employed both experimental and theoretical techniques to investigate its structural, physical and electronic properties of  $\text{WTe}_2$ , and verify that  $\text{WTe}_2$  has its minimum energy configuration in a distorted 1T structure (Td structure), which results in metallic-like behavior. Our findings confirmed the metallic nature of  $\text{WTe}_2$ , introduce new information about the Raman modes of Td- $\text{WTe}_2$ , and demonstrate that Td- $\text{WTe}_2$  is readily oxidized via environmental exposure. These findings confirm that, in its thermodynamically favored Td form. From our approach of developing  $\text{WTe}_2$  thin film materials via CVD processes, we have noticed that more reactive tungsten precursors could be the key to carry out  $\text{WTe}_2$  growth due to hydrogen reduction is the dominant reaction for tungsten trioxide ( $\text{WO}_3$ ) tellurization process. We successfully obtain Td- $\text{WTe}_2$  thin film on various substrates from changing tungsten precursor to tungsten hexacarbonyl ( $\text{W}(\text{CO})_6$ ). We verify the  $\text{WTe}_2$  film in Td structure by confirming Raman signature with synthesized  $\text{WTe}_2$  from CVT process. Further characterization and optimization of the growth process may be needed to understand  $\text{WTe}_2$  growth mechanism, substrate effects and growth conditions and achieve large area atomic layered growth of  $\text{WTe}_2$ . All of these findings will help the utilization of  $\text{WTe}_2$  in electronic device architectures such as field effect transistors (FETs) may be reevaluated. More application should be explored for this special 2D layered  $\text{WTe}_2$  materials.

# TABLE OF CONTENTS

LIST OF FIGURES .....	vi
LIST OF TABLES .....	x
Chapter 1 .....	1
Introduction and Literature Review .....	1
Two-dimensional Materials and Their Applications .....	1
1.2 Fundamental Information of Transitional Metal Dichalcogenides (TMDs) .....	6
1.3 Synthetic Routes for Tungsten Ditelluride ( $\text{WTe}_2$ ) .....	10
1.3.1 Chemical Vapor Transport (CVT) Method .....	10
1.3.2. Chemical Vapor Deposition (CVD) Method .....	12
Chapter 2 .....	18
Computational and Experimental Procedures .....	18
2.1 Experimental Materials and Substrate Preparation Processes .....	18
2.2 Tungsten Ditelluride Bulk Crystal Synthesis .....	19
2.3 Mechanical Exfoliation Process .....	20
2.4 CVD Furnace Design and Operation .....	21
2.5 Characterization Techniques .....	23
Chapter 3 .....	27
Properties of CVT-grown Bulk Tungsten Ditelluride ( $\text{WTe}_2$ ) .....	27
3.1 Crystal Structure of Bulk Tungsten Diterlluride .....	27
3.2 Bonding Information of Tungsten Ditelluride .....	28
3.3 Raman Signature of Tungsten Ditelluride .....	31
3.4 Layered Thickness .....	33
3.5 Electronic Properties .....	34
3.6 Stability of Tungsten Ditelluride .....	36
3.6.1 XPS Analysis .....	36
3.6.2 Raman Analysis .....	39

Chapter 4.....	41
Theoretical Calculation of Tungsten Diterlluride ( $\text{WTe}_2$ ) .....	41
4.1 Theoretical Calculation Setup.....	41
4.1.1 Tungsten Ditelluride Model .....	41
4.1.2 Convergence Study .....	46
4.3 Calculation Results and Discussion.....	48
4.3.1 Crystal Structures .....	48
4.4 Materials Properties Calculation.....	55
4.4.1 X-ray Diffraction Patterns.....	55
4.4.2 Raman Vibration Modes .....	56
4.5 Phase Transition of 2H- and Td- $\text{WTe}_2$ .....	58
Chapter 5.....	60
Tungsten Ditelluride Thin Film Deposition.....	60
5.1 $\text{WTe}_2$ Thin Film Materials .....	60
5.2 Tellurization via Chemical Vapor Deposition Method .....	60
5.2.1 Control Factors for Tellurization.....	63
5.3 Thin Film $\text{WO}_3$ Tellurization .....	66
5.4 Vapor Phase Tellurization .....	70
Chapter 6.....	75
Conclusion and Future Work .....	75
References.....	78

## LIST OF FIGURES

Figure 1.1.1. The transitional metals and three chalcogen elements compounds which crystallize in layered structure. The half-highlighted elements means only some of the dicalcogenides with these elements are in layered structures. <sup>21</sup>	1
Figure 1.1.2. Field-effect mobility and on/off ratios of TMD materials in comparison with other unconventional semiconductor materials. <sup>29</sup>	2
Figure 1.1.3. (a) Experimental subthreshold swing (SS) as a function of drain current compared with simulated results from Ghosh and Mahapatra <sup>30</sup> for MoTe <sub>2</sub> , MoS <sub>2</sub> , and WS <sub>2</sub> materials. (b) Simulated tunneling current versus electric field for various TMD homojunctions showing the potential of low-power TMD TFET transistors. <sup>31</sup>	3
Figure 1.1.4. Band alignment and band gap information of bulk and monolayer 2D TMDs. The grey area indicates the band gaps for bulk TMDs materials, and the slash green blocks indicates the band gaps for monolayer TMDs. The blue horizontal line is the Fermi level for each materials. <sup>11</sup>	4
Figure 1.1.5. (a) TFETs device schematic design plot using double-gated MX <sub>2</sub> TMD materials simulated in Lam et al. <sup>7</sup> Band offsets data were calculated and similar to Figure 1.1.2. (b), (c) and (d) showed the current vs. surface potential simulation data for (b) p-type; (c) n-type TFETs and (d) for paired TMD materials.	5
Figure 1.2.1. Crystal structures of bulk TMD materials in different stacking sequence. It demonstrates the MX <sub>2</sub> hexagonal structure of M and X sandwiched layers, and the side and top view of 1T, 2H and 3R layers stacking. <sup>36,37</sup>	7
Figure 1.2.2. The configuration and <i>d</i> -orbital splitting of two dominant coordination of TMD crystals.	8
Figure 1.2.3. Band structure change from bulk to monolayered MoS <sub>2</sub> . The arrow from top valence band (blue line) to lowest conduction band (green line) indicates the transition from indirect bandgap to direct bandgap of MoS <sub>2</sub> . <sup>37,40</sup>	9
Figure 1.2.4. Band structure for bulk(2H)-WTe <sub>2</sub> and single layer(1H)-WTe <sub>2</sub> . The indirect bandgap of bulk-WTe <sub>2</sub> changes to direct bandgap near K point for single layered-WTe <sub>2</sub> .	10
Figure 1.3.1. Phase diagram of Tungsten (W) – Tellurium (Te) with temperature T against tungsten percentage. <sup>53,54,60</sup>	12
Figure 1.3.2. Summary of techniques for monolayer TMD material synthesis. Methods including chemical vapor transport (CVT) for bulk TMD single crystals,	

powder vaporization carried out with flowing transfer gases in chemical vapor deposition (CVD) furnace, and metal-organic chemical vapor deposition (MOCVD) using metal-organic or metal-halogen precursors. <sup>84</sup>	16
Figure 2.2.1. Schematic plot for chemical vapor transport (CVT) for synthesizing tungsten ditelluride (WTe <sub>2</sub> ) single crystal. Bromide (Br <sub>2</sub> ) was chosen as a transport agent in the sealed quartz tube and expedite crystal formation.....	20
Figure 2.4.1. Schematic plot for CVD furnace employed in this work. ....	22
Figure 2.5.1. Schematic plot for the properties investigation plan for the exfoliated flakes of synthesized bulk WTe <sub>2</sub> with various characterization techniques. ....	26
Figure 3.1.1. Synthesized WTe <sub>2</sub> that observed its (a) large bulk crystals by bare eyes and (b) smaller crystallites by SEM. ....	27
Figure 3.1.2. X-ray powder diffraction (XRD) patterns confirms that WTe <sub>2</sub> crystallizes in space group Pmn2 <sub>1</sub> (C <sub>2v</sub> ) in orthorhombic Td structure. ....	28
Figure 3.2.1. High-resolution XPS spectrum from a freshly exfoliated WTe <sub>2</sub> flake. The full range spectrum in (a) shows no residue from transport agent from lack of peaks from Br element; (b) shows the high-res elemental spectra of Td 3d and W 4d region that is used to calculate Td-WTe <sub>2</sub> stoichiometry. ....	30
Figure 3.3.1. (a) Raman spectra of Td-WTe <sub>2</sub> using 647 (red), 514nm (green) and 488 nm (blue) laser excitation. The peaks in the spectra can be assigned to in-plane and out-of-plane (b) Raman-active vibrational modes obtained from vibration analysis done by DFT calculation. The major peaks were processed with Lorentzian peak fitting in both spectra, and the two distinct in-plane vibrational modes at 162 and .....	32
Figure 3.5.1. SEM and AFM images of (a) 129-Layer (129L), (b) 37-Layer (37L) and (c) 9-layer (9L) Td-WTe <sub>2</sub> Resistivity measurements as a function of temperature (d) confirm that Td-WTe <sub>2</sub> is metallic in nature (resistivity proportional to temperature), rather than the semiconducting behavior recently suggested <sup>27,31,34,35</sup> . ....	35
Figure 3.6.1. Stability testing of WTe <sub>2</sub> flakes in ambient air by high-resolution elemental XPS spectra. XPS analysis reveals an increase in Te-O bonding in the Td 3d and O 1s spectra with minor changes in the W 4d spectra, indicating the formation of TeO <sub>2</sub> on the surface. ....	38
Figure 3.6.2. The Raman spectrum after 13 days of air exposure for aged WTe <sub>2</sub> samples in (a) shows the small intensities change in for bulk surface and a large increase for thin-layered samples for the two in-plane modes in the 160-167cm <sup>-1</sup> region. The Raman spectrum of a laser-degraded sample in (b) suggests that	

photon-assisted oxidation can lead to rapid degradation of $\text{WTe}_2$ via the formation of $\text{TeO}_2$ .....	40
Figure 4.1.1. Single crystal structures, side view and plane view of (a) hexagonal 2H- $\text{WTe}_2$ ; (b) orthorhombic Td- $\text{WTe}_2$ theoretical models. ....	44
Figure 4.1.3. The convergence results from low to high cutoff energy with small to large k-points grid for (a) 2H- $\text{WTe}_2$ and (b) Td- $\text{WTe}_2$ .....	47
Figure 4.3.1. Te-W-Te bond angles in the (a) 2H- $\text{WTe}_2$ and (b) Td- $\text{WTe}_2$ structures. ....	49
Figure 4.3.3. The electronic band structures (a) and (b) density of states both indicate that bulk $\text{WTe}_2$ in the 2H structure has an indirect 0.702 eV bandgap. Bulk $\text{WTe}_2$ in the Td structure (c) has a 0.21eV band overlap in $\Gamma$ -X, and the density of states (d) reaches a minimum, but never goes to zero near Fermi level.....	52
Figure 4.3.4. Comparison of the band structure in different Brillouin Zone Path (a) $\Gamma$ -X and (b) $\Gamma$ -S with LDA and LDA plus DFT-D for Td- $\text{WTe}_2$ . Band separation from LDA to LDA plus DFT-D along different path can be observed when comparing (c) and (d) with (e) and (f).....	54
Figure 4.4.1. X-ray Diffraction Patterns for (a) experimental $\text{WTe}_2$ bulk crystal; (b) theoretical Td- $\text{WTe}_2$ ; (c) theoretical 2H- $\text{WTe}_2$ .....	55
Figure 4.5.1. DFT calculation results indicates that the enthalpy of formation of the Td- $\text{WTe}_2$ phase is lower than that of the 2H phase, regardless of pressure, indicating it is the most stable form of bulk Td- $\text{WTe}_2$ . ....	58
Figure 4.5.2. Summary of pressure-induced superconductivity of Td- $\text{WTe}_2$ . By applying a high pressure from 2.5GPa which causes lattice distortion and fermi level change, $\text{WTe}_2$ reached critical temperature around 2-3K at 2-4GPa, and increase to $T_c$ of 7K at 16.8GPa. ....	59
Figure 5.2.1. Experiments design and CVD furnace setting for $\text{WTe}_2$ synthesis by tellurization processes. The reaction took place at the hot-zone (T2), which is at the center of the furnace. Reaction temperature T2 at hot-zone, carrier gases $\text{H}_2$ :Ar ratio and growth time are the designed variables for $\text{WTe}_2$ growth. $\text{WO}_3$ was chosen tungsten precursor for this particular schematic plot due to it can be either sublimed at upstream or pre-deposited on substrates for tellurization processes. ....	62
Figure 5.3.1. The (a) AFM images for 10nm amorphous and 10nm and 50nm annealed $\text{WO}_3$ after tellurization, The rods formed lateral aggregates in dendrite structure for 10nm amorphous sample, while only small rods spreading on annealed sample. 50nm annealed $\text{WO}_3$ after tellurization seemed to form larger crystalline without dendrite structure. (b) SEM images shows the full	



- picture of the dendrite structure formed on 10nm amorphous  $\text{WO}_3$  after tellurization. (c) Raman spectra comparison between the amorphous  $\text{WO}_3$  and annealed  $\text{WO}_3$  thin film after tellurization showed they have different crystalline aggregates after tellurization. .... 66
- Figure 5.3.2. The (a) Raman Spectrum for the tellurized 10nm amorphous  $\text{WO}_3$  with the comparable range with (c)  $\text{WO}_2$  Raman in the literature. The peaks at 286.2, 342.7, 511.8 and 599.8  $\text{cm}^{-1}$  for our  $\text{WO}_3$  after tellurization were corresponding to the 288.7, 347.8, 516.9, and 603.2 $\text{cm}^{-1}$  for  $\text{WO}_2$  nanocrystalline.<sup>117</sup> (b) XPS confirmed that there was no Te exist on the surface in any way, which indicated that no tellurization but thermal reduction happened for  $\text{WO}_3$  thin film. .... 68
- Figure 5.3.3. The XRD patterns of 10nm  $\text{WO}_3$  after tellurization and overlay with the lattice planes of  $\text{WO}_2$  crystal in the ICDD database. .... 69
- Figure 5.3.4. The Raman spectra of oxidation on Te surface after etching process. Te oxidation happened right after wet etch process and form a layer of  $\text{TeO}_2$  on the surface. Raman signature indicates that the  $\text{TeO}_2$  layer was  $\alpha\text{-TeO}_2$ .... 70
- Figure 5.4.1. Schematic plot for  $\text{W}(\text{CO})_6$  powder tellurization processes..... 71
- Figure 5.4.2. (a) Raman; (b) OM; (c) FESEM; (d) AFM characterization for vapor phase tellurization of  $\text{W}(\text{CO})_6$ . The particulates were crystallized on sapphire substrates at 750°C with 30min tellurization time. .... 72
- Figure 5.4.3. Raman Spectra comparing the Raman from small crystals in Figure 5.4.2 from  $\text{W}(\text{CO})_6$  tellurization, and two spectra from bulk  $\text{WTe}_2$  obtained by CVT. There are two bulk  $\text{WTe}_2$  Raman spectra for the difference of incident laser would reveal more vibration modes with a lower excitation energy. The unknown peaks at 161 and 211  $\text{cm}^{-1}$  from  $\text{W}(\text{CO})_6$  tellurization are now identified as the combination of  $B_2$  and  $A_1$  modes at 165 $\text{cm}^{-1}$ , and  $B_1$  mode at near 212  $\text{cm}^{-1}$  for bulk- $\text{WTe}_2$ . (Details about vibration modes of bulk- $\text{WTe}_2$  in Figure 3.3.1.) ..... 73
- Figure 5.4.4. MOCVD schematic plot, and the temperature profile for tellurization with controlled  $\text{W}(\text{CO})_6$ . The carrier gas for  $\text{W}(\text{CO})_6$  is always  $\text{H}_2$  gas. The addition of  $\text{N}_2$  gas was useful to carry out some crystal-like particulate deposited on the substrate (not shown here). .... 74

## LIST OF TABLES

Table 1.3.2. Precursors that are used for CVD TMD thin film synthesis. ....	17
Table 2.1.1. Cleaning procedure silicon and sapphire substrates. ....	19
Table 2.4.1. Growth parameters range for CVD-grown WTe <sub>2</sub> processes. ....	23
Table 3.2.1 Binding energies from XPS peak fitting data for freshly exfoliated WTe <sub>2</sub> ....	29
Table 3.2.2 Modified Auger parameter ( $\alpha$ ) for freshly exfoliated WTe <sub>2</sub> .....	29
Table 3.5.1. WTe <sub>2</sub> Resistivity ( $\rho$ ) Data at 300K Compared to the Literature .....	36
Table 3.6. XPS analysis and peak fitting data for WTe <sub>2</sub> and degraded WTe <sub>2</sub> surface. ....	39
Table 4.1.1. Experimental Td-WTe <sub>2</sub> Lattice Parameters from ICDD Database .....	42
Table 4.1.2. 2H- and Td-WTe <sub>2</sub> initial crystal structures. ....	43
Table 4.1.3. DFT Calculation results of WTe <sub>2</sub> in different crystal structures .....	45
Table 4.4.2. Calculated vibrational modes, symmetry classification, IR and Raman activities for 2H- and Td-WTe <sub>2</sub> structures. (A = active) .....	57

## Chapter 1.

### Introduction and Literature Review

#### Two-dimensional Materials and Their Applications

The rise of graphene was a defining point for the discovery and development of stable two-dimensional layered materials (2DLM).<sup>1,2</sup> This breakthrough has stimulated the exploration of 2D materials such as hexagonal boron nitride (hBN)<sup>3</sup> and transition-metal dichalcogenides (TMDs)<sup>4</sup> of formula  $\text{MX}_2$ , where M is a IVB-VIB transition metal atom (IVB: Ti and Zr; V-B: Nb and Ta; VI-B: Mo and W) and X is a chalcogen (S, Se, or Te). Due to the *d*-orbitals involved in their electronic structure, the TMDs exhibit a wide range of electronic properties that have led to advances in practical devices, including field effect transistors,<sup>5–12</sup> photodetectors,<sup>13,14</sup> chemical<sup>15</sup> and biosensors,<sup>16–18</sup> and nano-electromechanical systems (NEMS).<sup>19,20</sup>

H	MX <sub>2</sub> M = Transition metal X = Chalcogen															He	
Li	Be											B	C	N	O	F	Ne
Na	Mg	3	4	5	6	7	8	9	10	11	12	Al	Si	P	S	Cl	Ar
K	Ca	Sc	Ti	V	Cr	Mn	Fe	Co	Ni	Cu	Zn	Ga	Ge	As	Se	Br	Kr
Rb	Sr	Y	Zr	Nb	Mo	Tc	Ru	Rh	Pd	Ag	Cd	In	Sn	Sb	Te	I	Xe
Cs	Ba	La - Lu	Hf	Ta	W	Re	Os	Ir	Pt	Au	Hg	Tl	Pb	Bi	Po	At	Rn
Fr	Ra	Ac - Lr	Rf	Db	Sg	Bh	Hs	Mt	Ds	Rg	Cn	Uut	Fl	Uup	Lv	Uus	Uuo

**Figure 1.1.1. The transitional metals and three chalcogen elements compounds which crystallize in layered structure. The half-highlighted elements means only some of the dicalcogenides with these elements are in layered structures.<sup>21</sup>**

Two-dimensional (2D) TMD systems have been widely explored both experimentally and theoretically for its electronic properties and device capability.<sup>4,21–27</sup> Unlike three-dimensional (3D) materials, they have weak van der waal bonds between layers which is a great feature for device design to avoid shield electric field and electron traps when compare to the defects and broken or dangling bonds on conventional semiconductor (e.g. Si and GaAs) materials. Recent research on single layer single layered MoS<sub>2</sub> FETs has demonstrated its moderate carrier mobility (60-70 cm<sup>2</sup>Ns<sup>79-81</sup>) and up to  $\sim 10^8$  on/off ratio at room temperature.<sup>5,28</sup> Figure 1.1.2. the comparison of field effect mobilities and on/off ratios for all candidate semiconductor materials, and TMDs are comparable to organics, amorphous oxide and carbon nanotube semiconductor materials.<sup>29</sup>

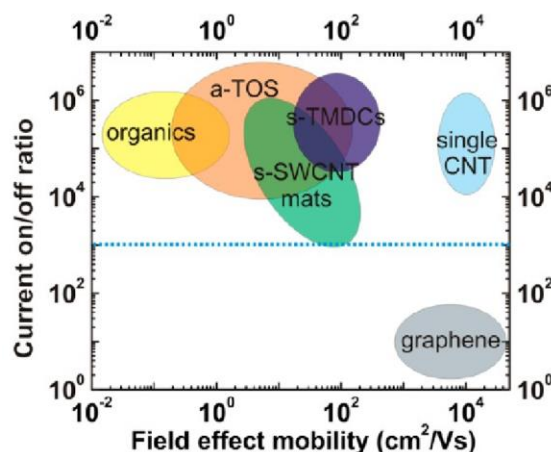


**Figure 1.1.2. Field-effect mobility and on/off ratios of TMD materials in comparison with other unconventional semiconductor materials.<sup>29</sup>**

The relative pristine interface without dangling bonds gives 2D materials great potential moving on ultrathin tunneling field effect transistors (TFETs), while 3D semiconductor materials suffer from interlayer transport properties. TFET is one of the leading candidate for low voltage and low power consumption transistors. By changing the MOSFET

mechanism from field-controlled barrier to band-to-band tunneling, TFETs are expected to achieve subthreshold swing (SS)  $< 60\text{mV/dec}$  for ideal thermionic devices at room temperature. Tunneling effect for bulk semiconductors are often limited abrupt p-n junctions and solubility of dopants in the crystal, while TMDs with energy bandgaps in  $\sim 1\text{--}2\text{eV}$  range and no surface dangling bonds are perfect for lower power TFETs. Figure 1.1.3. shows the experimentally measured TMD TFETs SSs as a function of drain current, as well as the simulated tunneling current of TMDs homojunctions against electric field.

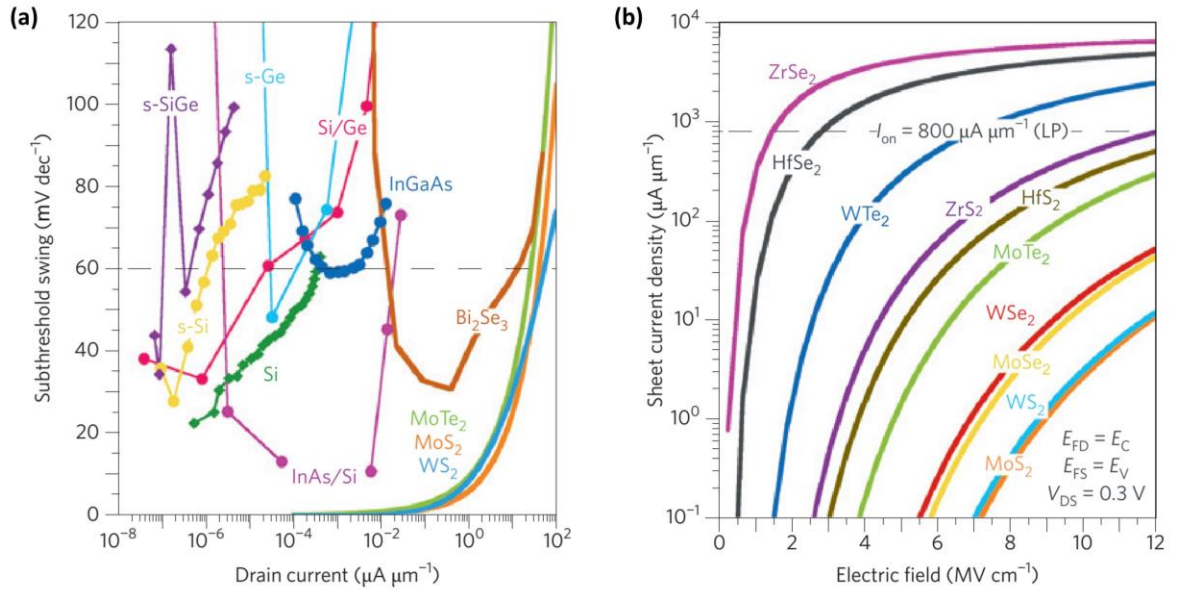


**Figure 1.1.3. (a) Experimental subthreshold swing (SS) as a function of drain current compared with simulated results from Ghosh and Mahapatra<sup>30</sup> for MoTe<sub>2</sub>, MoS<sub>2</sub>, and WS<sub>2</sub> materials. (b) Simulated tunneling current versus electric field for various TMD homojunctions showing the potential of low-power TMD TFET transistors.<sup>31</sup>**

Weak van der waal interlayer bonding and relative low lattice mismatch facilitate 2D materials integration simply by stacking layers in principle. 2D Heterostructures provide a platform for new devices design such as tunneling transistors, memory devices and

ultrathin photodetectors. Monolayered Mo- and W- dichalcogenides heterostructures with direct bandgap are predicted to have type-II band alignment,<sup>10,32,33</sup> while the conduction band minimum and valence band maximum are separated in the stacked materials. In this case, electrons and holes are confined in different materials, and in the valence band of one side can easily tunnel into the conduction band of the other material. This is highly expected with the combination monolayered VIB-TMDs and IVB-TMDs. Figure 1.1.4. shows the bandgap offset for bulk and monolayered TMDs materials and candidates to form this heterojunction. First principal calculation has demonstrated the TFET performance of different TMDs and TMD-combinations in Figure 1.1.5. Among these materials, single-layer 2H-WTe<sub>2</sub> is expected to have the narrowest band gap of the semiconducting VIB-TMDs at ~0.7eV.<sup>11,22,34,35</sup> This suggests a high electron mobility in all TMD candidates that could maximize the efficiency of electron injection in TMD TFETs.<sup>8,12</sup>

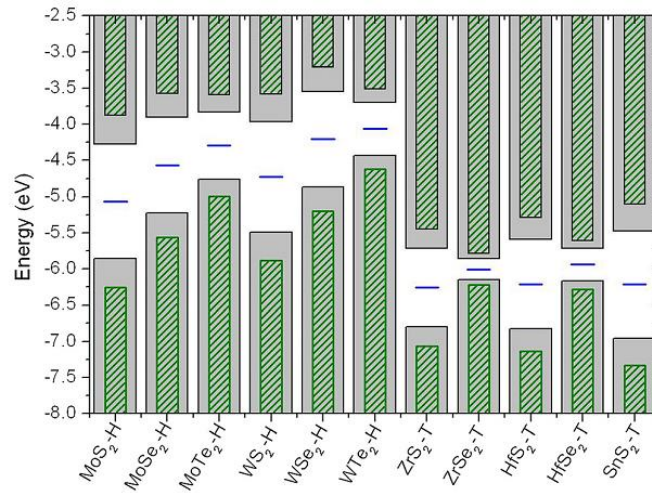


**Figure 1.1.4. Band alignment and band gap information of bulk and monolayer 2D TMDs. The grey area indicates the band gaps for bulk TMDs materials, and the slash green blocks indicates the band gaps for monolayer TMDs. The blue horizontal line is the Fermi level for each materials.<sup>11</sup>**

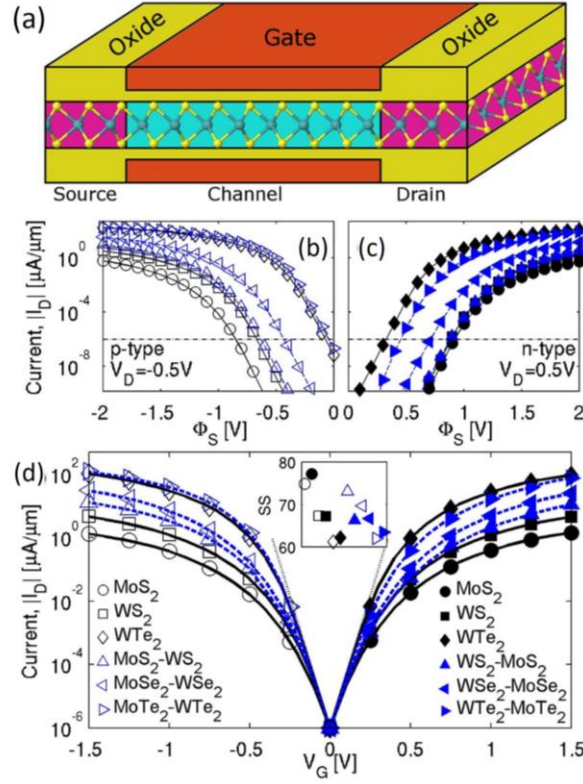


**Figure 1.1.5. (a) TFETs device schematic design plot using double-gated  $\text{MX}_2$  TMD materials simulated in Lam et al.<sup>7</sup> Band offsets data were calculated and similar to Figure 1.1.2. (b), (c) and (d) showed the current vs. surface potential simulation data for (b) p-type; (c) n-type TFETs and (d) for paired TMD materials.**

## 1.2 Fundamental Information of Transitional Metal Dichalcogenides (TMDs)

Transitional metal dichalcogenides (TMDs) in  $\text{MX}_2$  formula have been widely explored for their electronic properties and device performances in recent years. They have graphene/graphite-like layered structure in hexagonal crystal system, where transitional metal atom is sandwiched with two layers of chalcogenide atoms and form  $6\sim 7\text{\AA}$  thick for single layer TMD. The M-X coordination of layered TMD crystals can be either trigonal prismatic or octahedral. Depending on the stacking sequence, there are 2H and 3R structure for trigonal prismatic coordination, and 1T structure for octahedral coordination for bulk TMD crystals, showed in Figure 1.2.1. For single-layer TMD crystals, there are typically two polymorphs: trigonal prismatic coordinated 1H structure, and octahedral coordinated 1T structure.



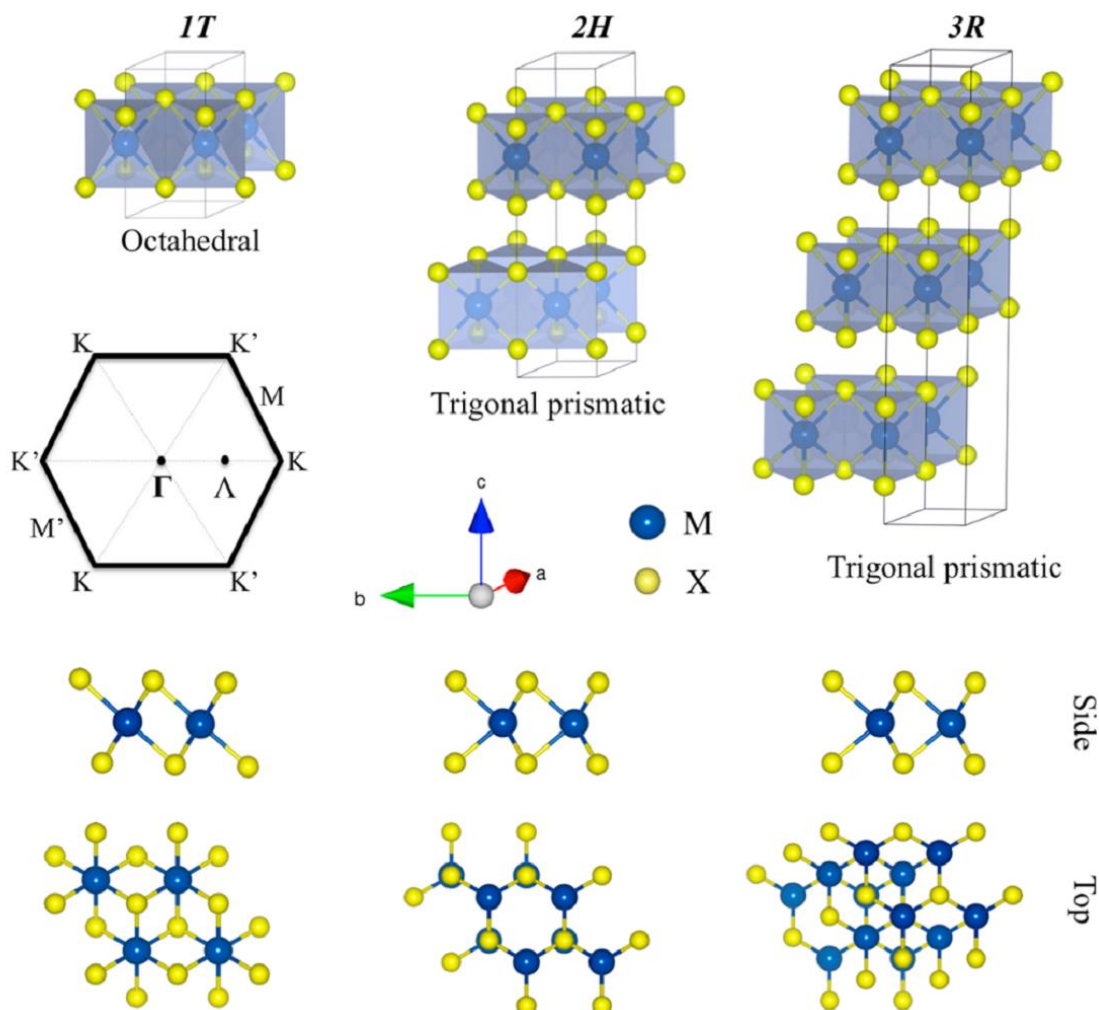


**Figure 1.2.1. Crystal structures of bulk TMD materials in different stacking sequence. It demonstrates the  $\text{MX}_2$  hexagonal structure of M and X sandwiched layers, and the side and top view of 1T, 2H and 3R layers stacking.<sup>36,37</sup>**

Electronic properties of TMDs vary with M-X coordination and their  $d$ -orbitals splitting of the transitional metal. Depending on the number of long-pair electrons of transitional metals filling the  $d$ -orbitals splitting with different coordination, TMDs can be either semiconductors or metallic materials. Due to the character that  $d$ -electrons would aggressively fill the non-bonding orbitals, TMDs with partially filled  $d$ -orbitals will demonstrate metallic conductive feature, while the fully-filled ones will show as

semiconductors. For VI-B groups  $\text{MX}_2$ , which means the  $\text{MoX}_2$  and  $\text{WX}_2$  ( $\text{X}=\text{S}, \text{Se}, \text{Te}$ ), are widely investigated based on 2H structure as semiconductors, and 1T phase as metallic materials.<sup>21</sup>

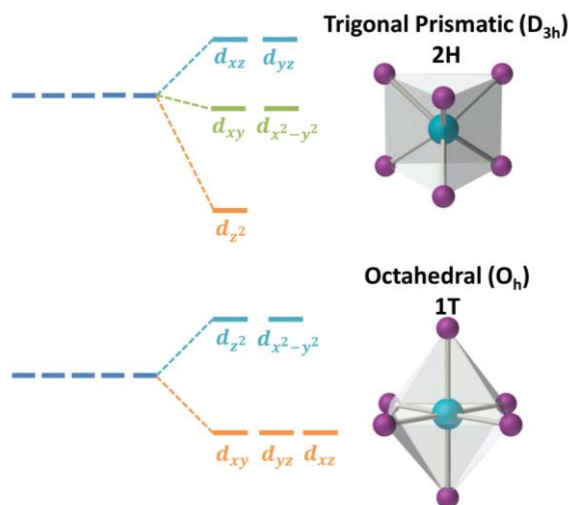


**Figure 1.2.2. The configuration and  $d$ -orbital splitting of two dominant coordination of TMD crystals.**

Change in number of layers may also affect the band structure of TMDs. Because of interlayer coupling and the arise of quantum confinement effects, TMDs have indirect-to-direct bandgap transition from bulk to monolayer.<sup>21</sup> This can be verified by photoluminescence of  $\text{MoS}_2$  from weak emission in bulk form and enhanced in monolayer form.<sup>21,38</sup> It is observed that the bandgap of monolayered  $\text{MoS}_2$ ,  $\text{MoSe}_2$ ,  $\text{WS}_2$ , and  $\text{WSe}_2$  is typically ~50% larger than bulk form.<sup>38,39</sup>

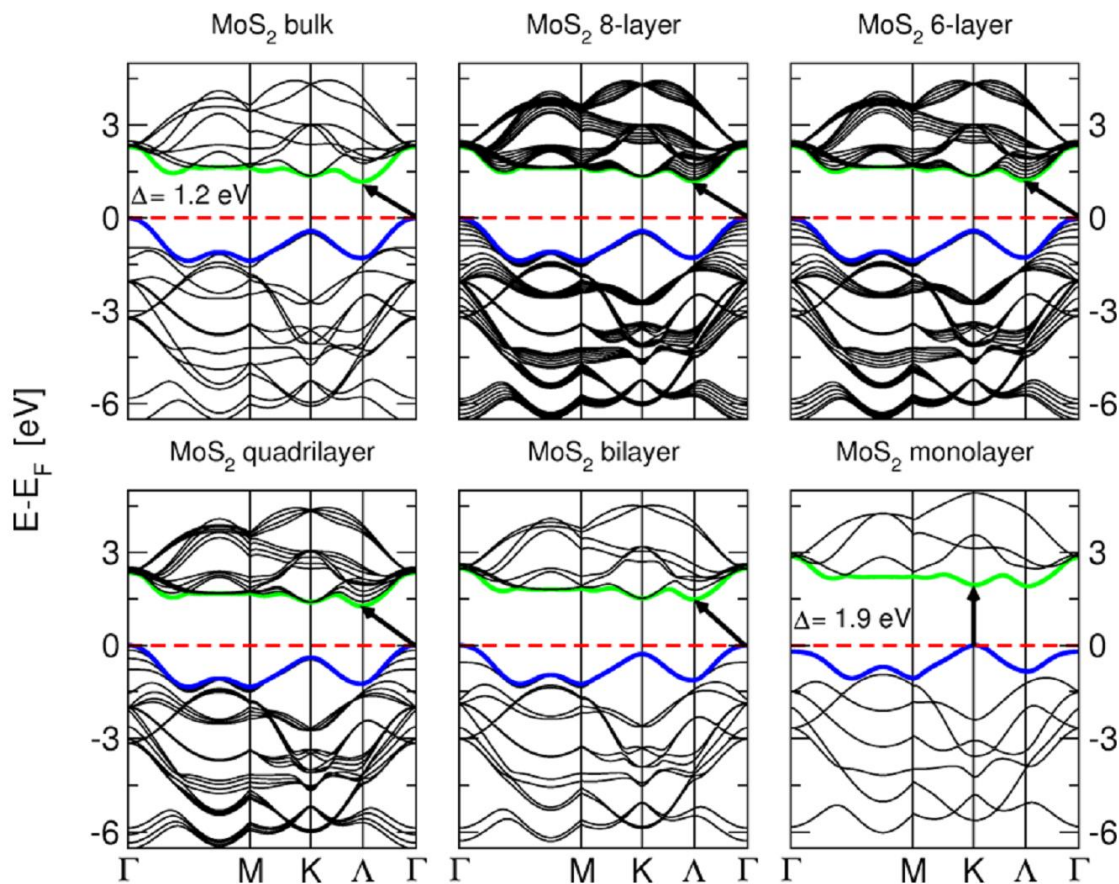


**Figure 1.2.3. Band structure change from bulk to monolayered MoS<sub>2</sub>. The arrow from top valence band (blue line) to lowest conduction band (green line) indicates the transition from indirect bandgap to direct bandgap of MoS<sub>2</sub>.<sup>37,40</sup>**

Base on the assumption of the VIB-dichalcogenide polymorph, plus the fact of indirect-to-direct band structure change with decrease of layer thickness, WTe<sub>2</sub> was expected to crystalize in 2H phase with direct bandgap in single layer that could extract high device efficiency. Figure 1.2.4. shows the band structure of bulk and single layer WTe<sub>2</sub> calculated with first principal calculation. The 0.7eV indirect bandgap for bulk-WTe<sub>2</sub> changes to 1.2eV direct bandgap for single layered-WTe<sub>2</sub>, which demonstrates the potential of designing single layered 2H-WTe<sub>2</sub> for highly efficient and atomically thin transistors.

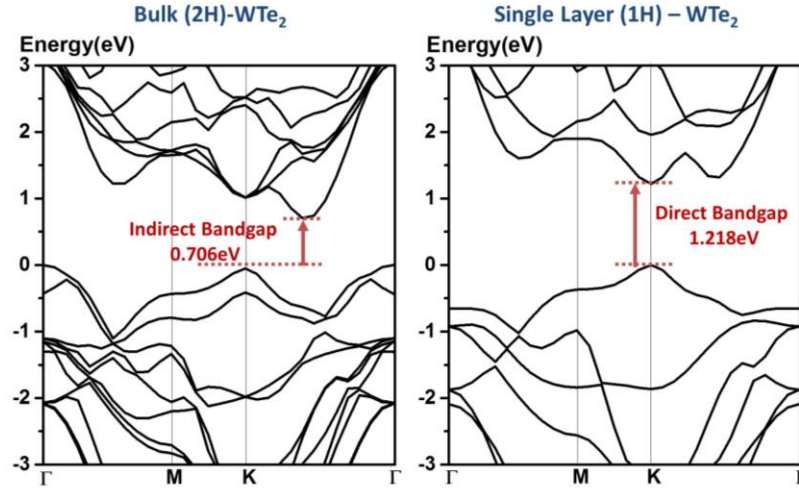


**Figure 1.2.4.** Band structure for bulk (2H)-WTe<sub>2</sub> and single layer(1H)-WTe<sub>2</sub>. The indirect bandgap of bulk-WTe<sub>2</sub> changes to direct bandgap near K point for single layered-WTe<sub>2</sub>.

### 1.3 Synthetic Routes for Tungsten Ditelluride (WTe<sub>2</sub>)

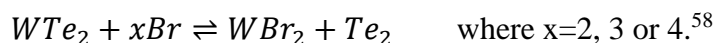
Despite the expectation on single layered 2H-WTe<sub>2</sub> from device-orientated research, the lack of the mineral sources has delayed the development progress of WTe<sub>2</sub> FETs. Synthetic materials is essential to push forward the studies regarding to WTe<sub>2</sub>.

#### 1.3.1 Chemical Vapor Transport (CVT) Method

Chemical vapor transport (CVT) method is one of the promising ways to obtain bulk, high purity crystals, and bulk TMDs crystals are one of them. This method was used to

synthesize a wide range of TMDs that could not be easily find in natural sources, such as TaS<sub>2</sub>, TaSe<sub>2</sub>,<sup>44,45</sup> MoTe<sub>2</sub>,<sup>46–48</sup> NbSe<sub>2</sub>.<sup>49</sup> In this method, accurately weighted transitional metal and chalcogen element powders were mixed and heat up in a vacuum-sealed ampule with a temperature gradient between two ends. A relative long synthesis time usually from days to weeks are needed for insuring obtaining bulk crystals.<sup>50</sup> Typically, a volatile halogens such as chloride (Cl<sub>2</sub>), bromide (Br<sub>2</sub>) and Iodine (I<sub>2</sub>) is needed in CVT method in order to transform the nonvolatile product into gaseous form diffuse in the ampule. The crystalline formation will take place if the conditions of chemical equilibrium is at crystallization rather than volatilization. Depends on the thermodynamic nature of the reaction of gaseous product and transport agent, crystallization may happen at the cold zone while the reaction is endothermic, or hot zone while exothermic.<sup>51,52</sup>

From the tungsten-tellurium binary phase diagram,<sup>53,54</sup> tungsten and tellurium would form liquid alloy in a tellurium-rich phase, which also means the reduction of tungsten melting temperature with tellurium. WTe<sub>2</sub> could possibly form from tungsten and tellurium liquid alloy under a peritectic reaction at 1020°C.<sup>53</sup> Knop and Haraldsen<sup>54</sup> studied W-Te phase diagram<sup>54</sup> and verified that WTe<sub>2</sub> is the only W-Te compound that could be formed obtained by direct synthesis in vacuum ampules with different W:Te element ratio. CVT method was then used for growing single bulk crystals by adding transport agents such as tellurium tetrabromide (TeBr<sub>4</sub>),<sup>55,56</sup> Br<sub>2</sub>,<sup>57,58</sup> tellurium tetrachloride (TeCl<sub>4</sub>)<sup>59</sup>. The chemical equilibrium reaction for synthesis of bulk WTe<sub>2</sub> is



in a two-zone or three-zone furnace for controlling the temperature gradient. Depending on the partial pressure of transport agents, synthesis temperature could range from 973 to 1173K for 15 hours to 5 days.<sup>54,58,59</sup>

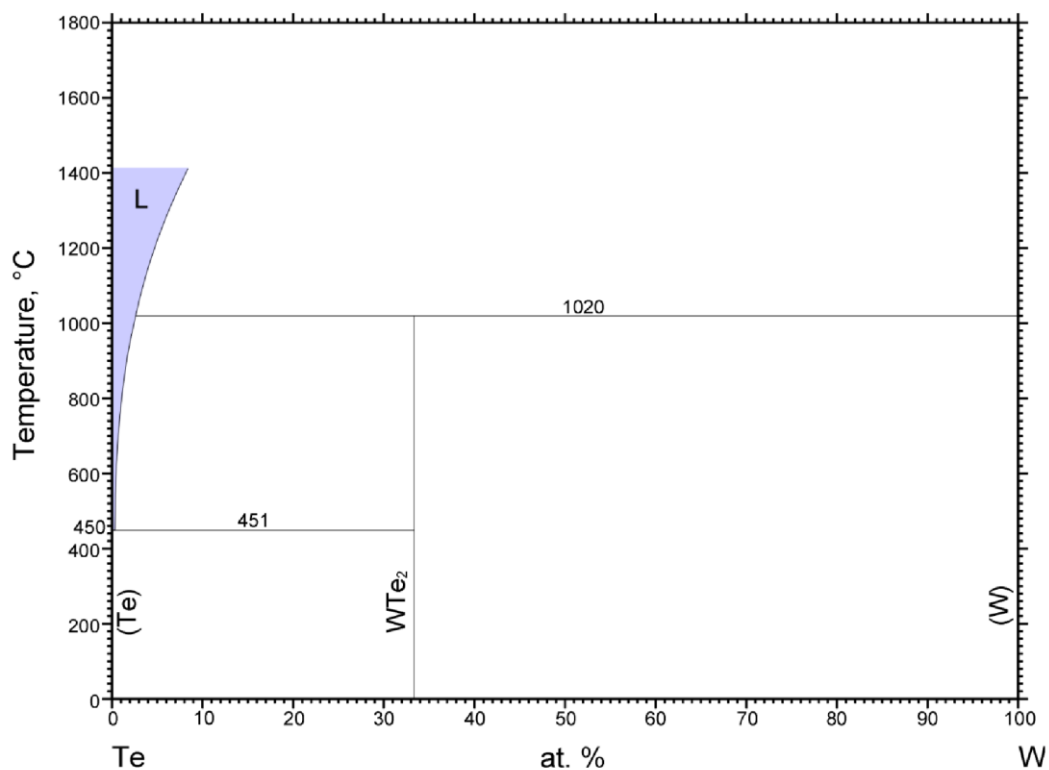


**Figure 1.3.1. Phase diagram of Tungsten (W) – Tellurium (Te) with temperature T against tungsten percentage .<sup>53,54,60</sup>**

### 1.3.2. Chemical Vapor Deposition (CVD) Method

Although high-quality bulk TMD crystals are suitable for studying basic material properties and provide a platform for studying exfoliated TMD materials, they are still ideal for small batches production. The high demand on thin film or single-layered TMD

materials promoted studies of synthesizing TMDs via thin film deposition methods. Among various deposition techniques including pulsed laser deposition,<sup>61</sup> spray pyrolysis,<sup>62</sup> sputtering,<sup>63</sup> dip coating and annealing<sup>64</sup> and atomic layer deposition (ALD),<sup>65</sup> chemical vapor deposition (CVD) method has been very successful to carry out large-area single-layered TMD materials.

Recent research involved CVD growth of monolayer TMD materials are mostly transitional metal sulfides and selenides (formula:  $MX_2$  where M: Mo, W; X: S, Se). Various CVD synthesis routes have been outlined, majority involved thermally-assisted sulfurization or selenization of transitional metals or transitional metal compounds. Considering the high melting and boiling temperature of tungsten (M.P.=3695K, B.P.=6203K) and molybdenum (M.P.=2896K, B.P.=4912K) which makes vapor phase reaction impossible, they were pre-deposited on designed substrates by electron-beam evaporation for sulfurization and selenization.<sup>66–69</sup> Instead of elemental Mo and W sources, transitional metal oxides such as  $MoO_3$ <sup>70–73</sup> and  $WO_3$ <sup>68</sup> were also often chosen as transitional metal sources for their low sublimation temperature ( $MoO_3$ : ~1073K;  $WO_3$ : ~823K). These oxides can be either pre-deposited on the substrates, or used as Mo and W precursors for vapor phase reaction in CVD processes.

It was easy and straight forward to achieve chalcogenization by thermally evaporating pure chalcogenides powders. When considering tellurization, it may be more challenging compare to selenization and sulfurization due to small electronegativity difference between Mo/W and Te, which means weaker bonding energy. This may also affect the stability for Mo and W ditellurides at high temperature.<sup>74</sup> Large-area molybdenum ditelluride ( $MoTe_2$ ) was successfully prepared by CVD tellurization reaction by Lin et al.<sup>74</sup> using  $MoO_3$  and

Te powder evaporation in a flowing argon and hydrogen mixed gas at 700°C. However, there is NO reports via CVD processes on tungsten ditelluride (WTe<sub>2</sub>) to date.

The crystalline quality and coverage of Mo/W dichalcogenide thin film done by solid-vapor deposition was limited due to residue from the impurity in the oxides, and defects from oxygen atoms. In order to improve the crystallinity and control large domain sizes of Mo/W dichalcogenide growth without residue, more sophisticated routes were developed by using metal-organics or metal-halogen precursors. Vapor phase reaction in CVD systems were very often seen for TMD monolayer growth. For transitional metal resources, transitional metal-organic precursors such as Mo(CO)<sub>6</sub><sup>75</sup> and W(CO)<sub>6</sub><sup>75,76</sup> can be used as precursor. Since they are stable in powder form, they can also be thermal evaporated for chalcogenization processes. Other transitional metal sources including transitional metal-halides such as MoF<sub>6</sub>,<sup>77</sup> MoCl<sub>5</sub>,<sup>78</sup> WCl<sub>6</sub>,<sup>79</sup> and oxo-halogen precursors WOCl<sub>4</sub><sup>80</sup> are also successful employed in TMD materials synthesis with proper filtration system in the downstream.

For chalcogen sources, a few selection of chalcogen compounds other than elemental S/Se/Te have successfully applied for CVD growth of TMDs. Simple but highly reactive hydride gas such as H<sub>2</sub>S,<sup>75,76</sup> H<sub>2</sub>Se<sup>81</sup> has been successfully carried out high-quality Mo/W sulfide and selenide monolayer growth. Delicate control of chalcogen precursor is needed for achieving large-area growth, a wide variety of metal-organic precursors including dimethyl-sulfide ((CH<sub>3</sub>)<sub>2</sub>S), 1,2-ethanedithiol (HS(CH<sub>2</sub>)<sub>2</sub>SH),<sup>80</sup> 2-methyl-propanethiol (CH<sub>3</sub>)<sub>3</sub>CSH,<sup>80</sup> and the series of dialkyl-sulfides/selenides like dimethyl-selenide ((CH<sub>3</sub>)<sub>2</sub>Se),<sup>82</sup> diethyl-selenide (C<sub>2</sub>H<sub>5</sub>)<sub>2</sub>Se<sup>81</sup> and di-tert-butylselenide<sup>81</sup> were used for synthesizing thin film Mo/W sulfides and selenides via CVD. Chalcogen chloride



precursors ( $\text{SeCl}_4$ ,  $\text{TeCl}_4$ ) are also effective precursors for CVD method, however, yet being explored for layered TMD synthesis possibly due to their deliquescence.

Up to date, there is no report on CVD-growth  $\text{WTe}_2$  thin film materials yet. Although many tungsten sources have already successfully brought out sulfides and selenides layered growth, proper tellurium sources has not yet be explored for  $\text{WTe}_2$  CVD growth. Tellurium has a higher sublimation temperature at  $450^\circ\text{C}$  than elemental sulfur and selenium, and the W-Te liquid phase at Te-rich region in W-Te binary system could potentially be an issue for  $\text{WTe}_2$  formation in short time CVD processes. On the other hand, the highly reactive hydride for tellurium,  $\text{H}_2\text{Te}$ , is commercially unavailable due to its unstable nature<sup>83</sup>. All of these indicates that controllable and reactive Te sources would be the key to carry out  $\text{WTe}_2$  synthesis by CVD processes.

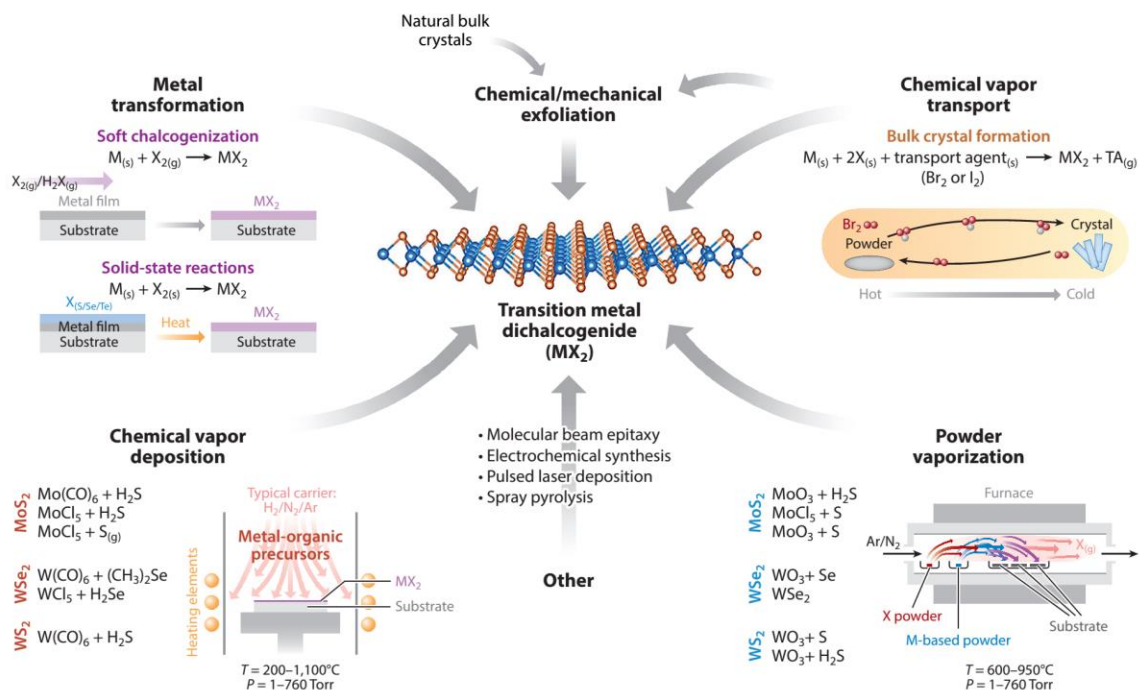


**Figure 1.3.2. Summary of techniques for monolayer TMD material synthesis.** Methods including chemical vapor transport (CVT) for bulk TMD single crystals, powder vaporization carried out with flowing transfer gases in chemical vapor deposition (CVD) furnace, and metal-organic chemical vapor deposition (MOCVD) using metal-organic or metal-halogen precursors.<sup>84</sup>

**Table 1.3.2. Precursors that are used for CVD TMD thin film synthesis.**

<b>Precursors Types</b>	<b>Transitional Metal Sources</b>		<b>Chalcogen Sources</b>	
	Mo	W	S/Se	Te
<b>Pure Element</b>	(Not practical due to high M.P.)		S/Se	Te
<b>Oxides</b>	MoO <sub>3(s)</sub>	WO <sub>3(s)</sub>	-	-
<b>Hydrides</b>	-	-	H <sub>2</sub> S/H <sub>2</sub> Se <sub>(g)</sub>	(Not available)
<b>Metal-Halides</b>	MoCl <sub>5(s)</sub>	WCl <sub>6(s)</sub>	SeCl <sub>4(s)</sub>	TeCl <sub>4(s)</sub>
		WOCl <sub>4(s)</sub>		
<b>Metal-Organics</b>	Mo(CO) <sub>6(s)</sub>	W(CO) <sub>6(s)</sub>	(CH <sub>3</sub> ) <sub>3</sub> CSH <sub>(l)</sub>	(CH <sub>3</sub> ) <sub>2</sub> Te <sub>(l)</sub>
	MoS <sub>4</sub> (NH <sub>4</sub> ) <sub>2(l)</sub>		(CH <sub>3</sub> ) <sub>2</sub> S <sub>(l)</sub> /(CH <sub>3</sub> ) <sub>2</sub> Se <sub>(l)</sub>	(C <sub>2</sub> H <sub>5</sub> ) <sub>2</sub> Te <sub>(l)</sub>
			HS(CH <sub>2</sub> ) <sub>2</sub> SH <sub>(l)</sub>	(C <sub>4</sub> H <sub>7</sub> ) <sub>2</sub> Te <sub>(s)</sub>

## Chapter 2

### Computational and Experimental Procedures

#### 2.1 Experimental Materials and Substrate Preparation Processes

Tungsten ditelluride bulk crystal were synthesized from tungsten and tellurium powders via chemical vapor transport method. Tungsten and tellurium powder used to initiate the synthesis were purchased from Acros Organics and Strem Chemicals with 99.9% purity. Bromine ( $\text{Br}_2$ ) was purchased from Sigma-Aldrich with 99.8+% purity used as the transport agent in the synthesis process.

Tungsten ditelluride thin film growth was also investigated via chemical vapor deposition (CVD) on sapphire and silicon substrates. Tungsten trioxide ( $\text{WO}_3$ ) purchased from Alfa Aesar Company (CAS No. 1314-35-8) with listed 99.8% purity, and  $\text{W}(\text{CO})_6$  (tungsten hexacarbonyl) purchased from Sigma-Aldrich (CAS No. 14040-11-0) with 99.99% purity were used as tungsten precursors for  $\text{WTe}_2$  growth. Tellurium shots with average 2-5mm size (CAS No. 13494-80-9) and a listed 99.9999% purity were purchased from Alfa Aesar Company, used as the tellurium source in all CVD growth processes.

Prior to all CVD growth processes of tungsten ditelluride, silicon and sapphire substrates were cleaned by a cleaning procedure with various solvents, listed in Table 2.1.1. Substrates were sonicated in acetone followed by isopropanol alcohol (IPA) solvents for initial cleaning of organic residues on the substrates. Overnight cleaning by immersing the diced substrates into Optic-clear are required to remove the sealant used for dicing the substrates prior to the solvent and ultrasonic cleaning process. Following solvent cleaning, substrates were placed in Nanostrip 2x solution, a stabilized sulfuric and hydrogen peroxide

solution purchased from Cyantek, to remove organic residue and ionic contamination on the surface. Running DI water cleaning after nanostrip process was necessary to clean out the nanostrip solution left on the substrate. The cleaned substrates were dried using nitrogen gun spraying on the surface right after taking out from DI water.

**Table 2.1.1. Cleaning procedure silicon and sapphire substrates.**

<b>Step</b>	<b>Chemical/Solution</b>	<b>Operating Temp.</b>	<b>Duration</b>
<b>0</b>	Optic-Clear	Room Temp.	Overnight
<b>1</b>	Acetone	Room Temp.	10min
<b>2</b>	IPA	Room Temp.	10min
<b>3</b>	Nanostrip 2x	90°C	20min
<b>4</b>	DI Water	Room Temp.	Running, 15 times
<b>5</b>	Nitrogen Gas	-	Drying

## **2.2 Tungsten Ditelluride Bulk Crystal Synthesis**

Tungsten ditelluride (WTe<sub>2</sub>) bulk crystals were produced by the chemical vapor transport (CVT) method with bromine as the transport agent. A mixture containing stoichiometric amounts of tungsten and tellurium powder were heated at 800°C for 3 days in an sealed quartz ampoule (10 mm ID, 12 mm OD, 150 mm length) evacuated to 10<sup>-3</sup> Torr range. The mixture was slowly heated from room temperature to 800°C for 12 h; slow heating was used to minimize the possibility of explosion due to the strong exothermic reaction that occurs during annealing. Some tellurium sublimed into the cooler zone of

the ampoule ( $\sim 350^\circ\text{C}$ ), so the two ends of the ampoule were kept at  $950^\circ\text{C}$  and  $775^\circ\text{C}$  for another day to ensure that all the tellurium reacted with the tungsten.  $\text{WTe}_2$  single crystals were grown from the synthesized powder by chemical vapor transport with bromine as the transport gas at  $\sim 6 \text{ mg/cm}^3$ . Bulk crystal used the synthesized  $\text{WTe}_2$  powder and transport agent in a sealed quartz ampule for 4 days. The hot and growth zones of which were kept at  $840^\circ\text{C}$  and  $900^\circ\text{C}$ , respectively. The synthesized bulk crystals were pumped under dynamic vacuum at room temperature for 1 day in order to remove any residual bromine.

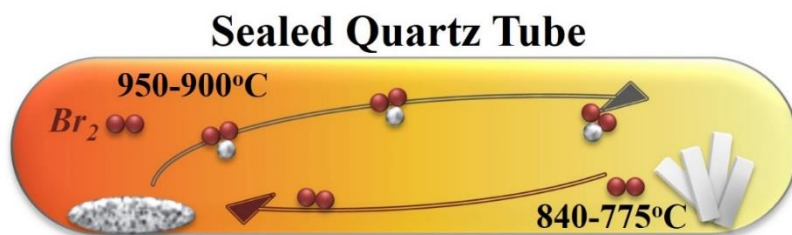


**Figure 2.2.1. Schematic plot for chemical vapor transport (CVT) for synthesizing tungsten ditelluride ( $\text{WTe}_2$ ) single crystal. Bromide ( $\text{Br}_2$ ) was chosen as a transport agent in the sealed quartz tube and expedite crystal formation.**

### 2.3 Mechanical Exfoliation Process

$\text{WTe}_2$  flakes were mechanically exfoliated onto freshly cleaned  $\text{SiO}_2$  substrates via the “scotch-tape” method<sup>53</sup>.  $\text{WTe}_2$  bulk crystals were exfoliated multiple times on the tapes and then transferred to the substrates. Silicon substrates with 285nm to 350nm grown silicon dioxide ( $\text{SiO}_2$ ) were used to carry the exfoliated tungsten ditelluride flakes for further measurements. Each  $\text{WTe}_2$  flakes were imaged by Olympus MX50 optical

microscope under 5x, 10x, 20x, 50x and 100x magnification in order to accurately locate and record their relative positions on SiO<sub>2</sub> substrates.

## **2.4 CVD Furnace Design and Operation**

Tungsten ditelluride growth was carried out by hot-wall tube CVD furnaces with quartz tubes. The CM Furnace (Serial Number: 950167) employed for thin film growth processes in this work is a tube furnace compatible with 3 inch tube and equipped with a 36 inches heating element with a maximum heating temperature of 1200°C, controlled by Honeywell UDC3000 heat controller. This furnace was designed for growth of TMD materials including molybdenum disulfide (MoS<sub>2</sub>), tungsten diselenide (WSe<sub>2</sub>) and WTe<sub>2</sub> on multiple substrates. In order to prevent cross-contamination, liner tubes with 40mm outer diameter (36mm inner diameter) x 48 inches length were used to carry out various growth procedures. In all growth procedures, ultra-high purity (UHP) Argonne (Ar) and UHP hydrogen (H<sub>2</sub>) carrier gas sources with two different mass flow controllers (MFC) are used during growth. Temperature profile was done by controlling the hot zone temperature from 500°C-1100°C to obtain the correlation between the temperature and different sections of the tube furnace.

Pre-annealing process using 100% UHP-H<sub>2</sub> gas flow and heated up to 1000°C (> the actual growth temperature) for one hour was applied prior to each growth process to clean the residue on the liner tube and ceramic/quartz boats left from previous growth. Whole CVD system was checked for the base pressure and gas leak rate prior to each growth process.

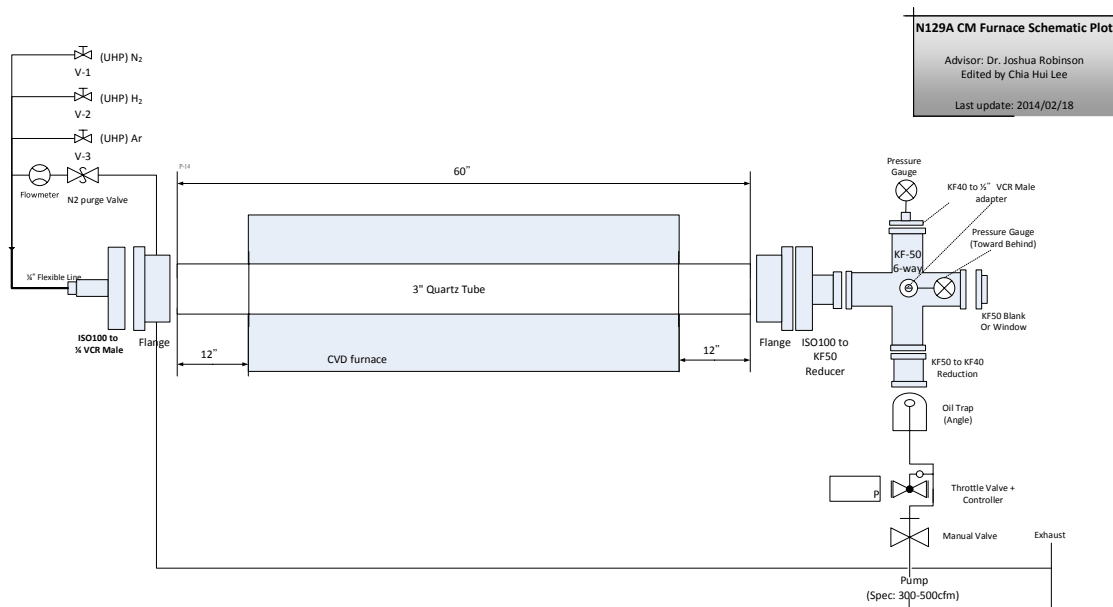


**Figure 2.4.1. Schematic plot for CVD furnace employed in this work.**

After pre-annealing process, cleaned substrates are loaded with designed amount of tellurium shots in a quartz/ceramic boat to the hot zone of the furnace. Substrates can also be loaded in another quartz/ceramic boat at downstream for deposition temperature studies; tellurium shots can also be loaded in different sections in the upstream of the furnace for sublimation temperature studies. The sources of tungsten can either be pre-deposited tungsten trioxide films, or sublimation of tungsten trioxide and tungsten hexacarbonyl. The details of the choices of precursors for growth, the temperature control of the furnace will be discussed in Chapter 5. The ramp rate of the furnace is  $25^{\circ}\text{C}/\text{min}$  below  $500^{\circ}\text{C}$ , and  $9^{\circ}\text{C}/\text{min}$  above  $500^{\circ}\text{C}$  due to the limit of output power of the furnace. Ar and  $H_2$  gas with various ratio flows continuously throughout the growth process. Pressure in the growth was controlled by MKS 651C throttle valve constantly. The growth time, pressure and



temperature are varied to achieve a complete study on  $\text{WTe}_2$  growth via CVD. The parameters are listed in the in Table 2.4.1.

**Table 2.4.1. Growth parameters range for CVD-grown  $\text{WTe}_2$  processes.**

Parameter	Range
Growth Time	30mins – 240mins
Growth Temperature	650 °C - 950°C
Growth Pressure	100mTorr – 600 Torr

## 2.5 Characterization Techniques

All synthesized bulk, exfoliated  $\text{WTe}_2$  samples, and CVD-grown samples were characterized for their structural information, stoichiometry, physical properties and stability. For structural information, it is required to confirm  $\text{WTe}_2$  crystal structure and purity of the synthesized  $\text{WTe}_2$  powder and bulk crystals. X-ray powder diffraction (XRD) can provide the scattering patterns of material from incident x-ray beam interaction with the material lattice. We use PANalytical XPert Pro MPD theta-theta diffractometer with  $\text{Cu } \alpha$  x-ray source to confirm the powder and bulk crystal of  $\text{WTe}_2$ . XRD patterns are further analyzed by JADE (software with XRD databases including ICDD) is used to verify the materials and crystal structures.

For stoichiometry and electron imaging, energy dispersive spectroscopy (EDS) on a FEI Nova NanoSEM 630 FESEM were used to confirm the stoichiometry of both  $\text{WTe}_2$  powders and bulk crystals. The incident photon induce x-ray fluorescence which generated

from transition of electron from outer energy shell to inner shell. The energy dispersive spectrometer collects x-rays fluorescence signal plot them as counts versus energy curve, and can be used to identify the elements. EDS was collect while imaging the crystal with scanning electron microscope (SEM). The clear image and morphology of bulk crystal and thin film  $\text{WTe}_2$  were obtained with a Leo 1530 Field Emission Scanning Electron Microscope (FESEM) operated at 2kV. The size of each exfoliated flake was measured by the measuring scales on Leo 1530 FESEM system.

Raman spectroscopy are commonly used to provide a fingerprint of graphene and many 2D materials. It observes the inelastic scattering or so-called Raman scattering usually induced by a laser in the visible, near infrared to near ultraviolet range. The incident laser interacts with the specimen with molecular vibrations and phonon excitation in the material systems, causing the photons shifts up or down that give information about the vibration modes in the materials. Raman spectra of exfoliated thick and few-layer  $\text{WTe}_2$  flakes on substrates were carried out using a Renishaw inVia confocal microscope-based Raman spectrometer with a spectral resolution less than  $1\text{ cm}^{-1}$ . Raman spectroscopy (WiTec CRM200) with an incident laser wavelength of 488nm was also used to obtain Raman spectra for aged  $\text{WTe}_2$  and laser degraded  $\text{WTe}_2$  studies.  $\text{SiO}_2$  substrates are used for carrying the exfoliated  $\text{WTe}_2$  flakes to provide clear vision under microscopes compared to other substrates such as polished sapphire or silicon substrates, and reduce residual heat from laser excitation as well. Laser power is controlled at 1.4mW for 488nm and at 0.5mW for 514 and 647nm laser excitations. The acquisition time may be different for different laser excitation to effectively avoid burned marks on the surface of exfoliated flakes. All Raman spectra was normalized for analysis.

Layer thickness and number of layers of the exfoliated WTe<sub>2</sub> flakes were determined by atomic force microscopy (AFM) which operate by measuring force between the probe and the sample with a sharp tip. It can measure the vertical and lateral deflections of the cantilever by using the optical lever with reflecting laser. We used Bruker Dimension Icon AFM in tapping mode in air. NanoScope Analysis ver.1.40 software from Bruker Corp. is used to process and analyze the thickness data collected from AFM.

Electrical properties of WTe<sub>2</sub> samples of different thicknesses were tested using two Ti/Au (Ti/Au=20/100nm) contacts made by a lift-off process at both edges of the exfoliated WTe<sub>2</sub> flakes. Total resistance versus temperature measurements were collected by using a Lakeshore Cryo Probe Station, which controlled the temperature from liquid nitrogen temperature 77K to 400K under vacuum. Conductive atomic force microscopy (C-AFM) using a gold-plated probe and contact mode on Bruker Icon was also used to observe the electronic properties of exfoliated WTe<sub>2</sub> flakes on gold substrates.

Surface-sensitive x-ray photoelectron spectroscopy (XPS) based on photoelectric effect irradiated with x-rays was a non-destructive technique used to study elemental composition, bonding information and stability of WTe<sub>2</sub> flakes. The photoelectrons originated in the first 5-10nm of the surface from incident x-rays eject from the surface and captured by the spectrometer. The kinetic energy (K.E.) of the emitted photoelectrons equals to the difference of incident photon energy and the bonding energy (B.E.) of the electron:

$$K.E. = h\nu - B.E. \quad \text{Equation 2.5.1}$$

The XPS spectra we used to investigate WTe<sub>2</sub> stoichiometry and chemical states (oxidation states) of the WTe<sub>2</sub> samples collected by Kratos Analytical Axis Ultra, using

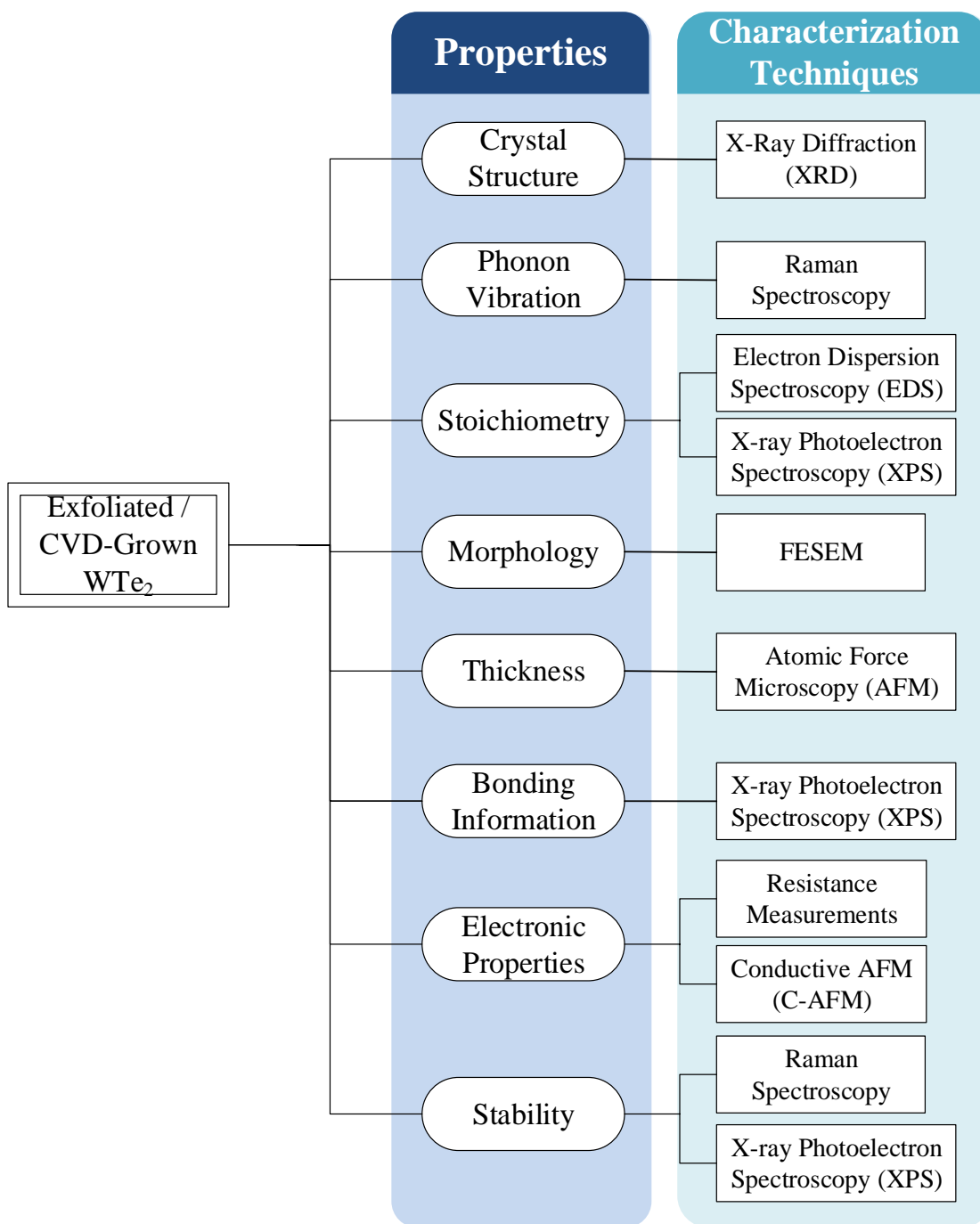


**Figure 2.5.1. Schematic plot for the properties investigation plan for the exfoliated flakes of synthesized bulk WTe<sub>2</sub> with various characterization techniques.**

## Chapter 3

### Properties of CVT-grown Bulk Tungsten Ditelluride ( $\text{WTe}_2$ )

#### 3.1 Crystal Structure of Bulk Tungsten Diterlluride

Bulk  $\text{WTe}_2$  single crystals were obtained from chemical vapor transport (CVT) as described in section 2.1 using tungsten and tellurium powders and bromine as the transport agent. The synthesized single crystals appear metallic in nature as shown in Figure 3.1.1(a). Both the powder and bulk single crystals were characterized by x-ray powder diffraction (XRD) to confirm the crystal structure of the CVT-grown tungsten ditelluride. Scanning electron microscopy (SEM) images and electron dispersive spectroscopy (EDS) results were also used to observe the crystal and verify the tungsten and tellurium ratio.

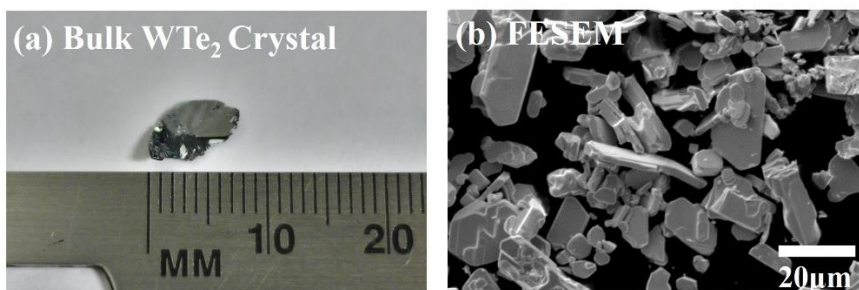


**Figure 3.1.1. (a) Synthesized  $\text{WTe}_2$  crystals are mm sizes and mostly flat. (b) SEM images also showed that  $\text{WTe}_2$  crystallites are mostly plate-structure.**

Single crystals of tungsten ditelluride have platelet structure, and can be exfoliated easily by scotch-tape method described in Chapter 2. SEM images of tungsten ditelluride powder in Figure 3.1.1(b) also reveals a platelet morphology with no apparent angles that

would be expected for hexagonal crystals. XRD (Figure 3.1.2) indicates an atomic arrangement is based on the primitive orthorhombic space group  $Pmn2_1$ , consistent with the formation of the Td-WTe<sub>2</sub> structure. The experimental XRD pattern collected from bulk WTe<sub>2</sub> crystal was compared to simulated XRD patterns based on the Td-WTe<sub>2</sub> and 2H-WTe<sub>2</sub> structures, and will be discussed in chapter 4.4.1. The distinctive reflections of the Td structure are present in the experimental diffractogram.

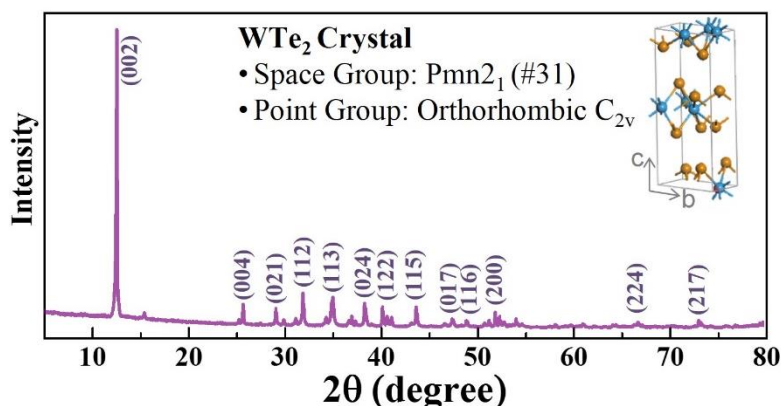


**Figure 3.1.2.** X-ray powder diffraction (XRD) patterns confirms that WTe<sub>2</sub> crystallizes in space group  $Pmn2_1$  ( $C_{2v}$ ) in orthorhombic Td structure.

### 3.2 Bonding Information of Tungsten Ditelluride

To confirm the stoichiometry of the synthesized tungsten ditelluride, x-ray photoelectron spectroscopy (XPS) is used to extract the composition WTe<sub>2</sub> flakes. The full range XPS spectrum in Figure 3.2.1(a) can roughly verify tungsten to tellurium ratio, which is further confirmed by calculating high-resolution elemental XPS spectra from W 4d and Te 3d regions in Figure 3.2.1(b). The calculated results confirms a W:Te ratio of 1:1.9 for bulk WTe<sub>2</sub> crystals, suggesting a slight Te deficiency.

Elemental XPS spectra of Te 3d and W 4d region was used to analyze the binding

energy for WTe<sub>2</sub>. Td 3d (571.80eV) and W 4d (242.30eV) regions were selected based on the peaks not overlapping with the other elemental regions. W 4d was specifically chosen due to overlaps of Te 4d and W 4f region. From peak fitting analysis of high-res spectra, we obtained Td 3d<sub>3/2</sub> and 3d<sub>5/2</sub> at 582.51eV and 572.12eV, and W 4d<sub>3/2</sub> and 4d<sub>5/2</sub> at 255.41eV and 243.10eV, listed in Table 3.2. For binding energy differences smaller than Modified Auger parameters (Equation 3.2.2)<sup>85,86</sup> from Wagner's definition of Auger parameters in Equation 3.2.1<sup>85</sup> is used to extract more information for synthesized WTe<sub>2</sub>:

$$\alpha = KE_{Auger} - KE_{Pe} \quad \text{Equation 3.2.1}^{85}$$

$$\alpha = KE_{Auger} - (h\nu - BE_{Pe})$$

$$\text{Modified } \alpha = \alpha + h\nu = KE_{Auger} + BE_{Pe} \quad \text{Equation 3.2.2}^{86}$$

where  $KE_{Auger}$  is kinetic energy (KE) of Auger electron and  $KE_{Pe}$  is kinetic energy of photoelectron. Auger parameter results calculated from KE of Te MNN Auger and BE of Te 3d<sub>5/2</sub> (Table 3.2.2) and compared to NIST XPS database<sup>86,87</sup>, indicating the difference of Te and WTe<sub>2</sub> which can be used in identifying W-Te bonding.

**Table 3.2.1 Binding energies from XPS peak fitting data for freshly exfoliated WTe<sub>2</sub>.**

Region/Sample	Te 3d				W 4d			
	Te 3d <sub>3/2</sub>		Te 3d <sub>5/2</sub>		W 4d <sub>3/2</sub>		W 4d <sub>5/2</sub>	
	WTe <sub>2</sub>	Te	WTe <sub>2</sub>	Te	WTe <sub>2</sub>	W	WTe <sub>2</sub>	W
<b>Fresh exfoliated WTe<sub>2</sub> surface</b>	582.51	-	572.12	573.1 <sup>8</sup>	255.41	-	243.10	243.50

**Table 3.2.2 Modified Auger parameter ( $\alpha$ ) for freshly exfoliated WTe<sub>2</sub>.**

Te Auger KE	Te 3d BE	Modified $\alpha$ for WTe <sub>2</sub>	Modified $\alpha$ for Te (NIST) <sup>86</sup>
-------------	----------	--	---

<b>Fresh exfoliated WTe<sub>2</sub> surface</b>	491.99	572.12	1064.11	1064.9
---	--------	--------	---------	--------

Full range high-res XPS spectrum in Figure 3.2.1(a) is not only used to obtain the bonding information for the exfoliated WTe<sub>2</sub>, but also to check for transport agent impurities. XPS data verifies that Br is not incorporated in significant quantities into the WTe<sub>2</sub>. Close observation at the Br 3p region (~188.3eV) and the Br 3d region (~68-70eV) shows that there are no Br peaks. Auger spectra in the higher binding energy region (not shown here) were also checked for Br peaks, and verified that Br was below detection limits.

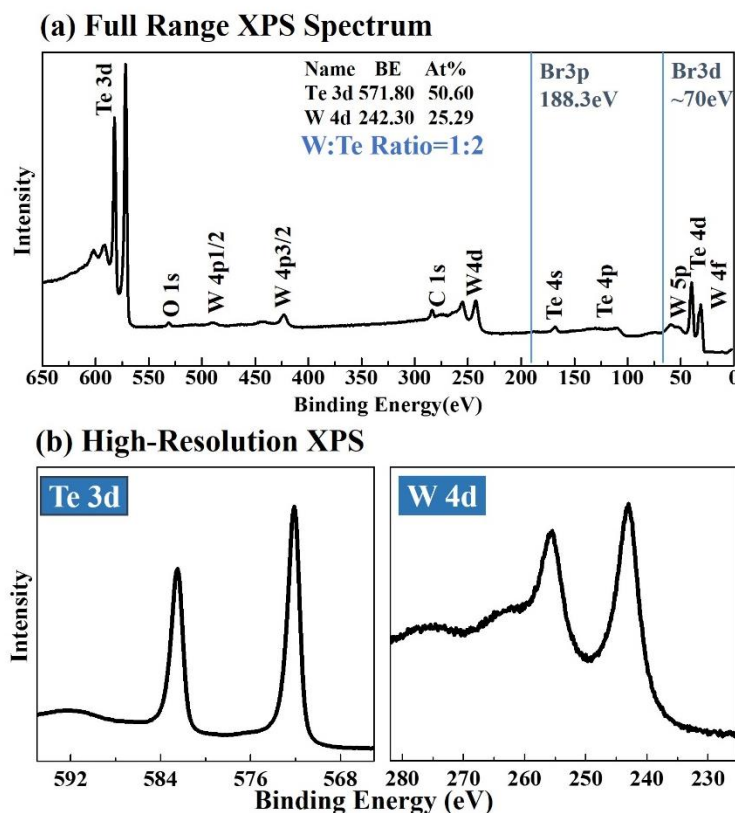


**Figure 3.2.1. High-resolution XPS spectrum from a freshly exfoliated WTe<sub>2</sub> flake. The full range spectrum in (a) shows no residue from transport agent from lack of peaks**



from Br element; (b) shows the high-res elemental spectra of Td 3d and W 4d region that is used to calculate Td-WTe<sub>2</sub> stoichiometry.

### 3.3 Raman Signature of Tungsten Ditelluride

To date, there are no reports on the vibrational properties of 2H- or Td-WTe<sub>2</sub>. We have explored the vibrational properties as a function of incident photon energy via Raman spectroscopy, and the results are shown in Figure 3.3.1. Flakes of Td-WTe<sub>2</sub> were exfoliated onto SiO<sub>2</sub>/Si substrates (each >10 layers thick), and Raman spectra were acquired from 647, 514 and 488 nm laser excitations. With 488 nm excitation, the vibrational modes are dominated by peaks at 112, 118, 133, 163, 165, and 212 cm<sup>-1</sup>. The same vibrational modes are evident with excitation in low energy. But slight frequency shifts at 133-135cm<sup>-1</sup> region and 210-212cm<sup>-1</sup> region, and an additional peak also appears close to 118cm<sup>-1</sup> with both 514 and 647nm excitations. To understand the origin of the Raman peaks, we used density functional perturbation theory (DFPT)<sup>89</sup> to calculate the vibrational modes in Td-WTe<sub>2</sub>. The calculated modes, as well as the symmetry analysis and their infrared and Raman activity are calculated by density functional theory (DFT) in chapter 4 and listed in Table 4.4.2. The phonon modes that correlate to the experimentally observed vibrations (Figure 3.3.1(a)) are shown in Figure 3.3.1(b). Because of the structural distortion induced by metal-metal bonding, the out-of-plane vibrational modes of Td-WTe<sub>2</sub> are not oriented perpendicular to the WTe<sub>2</sub> sheets. The out-of-plane Raman-active modes for Td-WTe<sub>2</sub> are vibrating either along the W-Te bond or at an angle to the vertical line, in contrast to the A<sub>1g</sub> mode of 2H-WTe<sub>2</sub> that involves atomic motion perpendicular to the layer plane. The 118, 133-135, and 212 cm<sup>-1</sup> peaks in experimental Td-WTe<sub>2</sub> Raman spectra are identified as “tilted” out-of-plane A<sub>1</sub> modes at 119, 133, 218

$\text{cm}^{-1}$  and tilted  $B_1$  vibrational modes at 127 and 216  $\text{cm}^{-1}$ . The out-of-plane  $A_1$  mode at 119  $\text{cm}^{-1}$  and in-plane  $B_2$  mode at 121  $\text{cm}^{-1}$  from detailed phonon vibrational analysis result can both contribute to Raman peak showed up near 118  $\text{cm}^{-1}$  in Raman spectra resulted from 514 and 647 nm excitation. On the other hand, the two deconvoluted peaks near 163  $\text{cm}^{-1}$  and 166  $\text{cm}^{-1}$  in the 647 nm Raman spectrum in Figure 3.3.1(a) are identified as the in-plane  $B_2$  and  $A_1$  vibrational modes in different directions; the observed frequencies are close to the calculated 159 and 167  $\text{cm}^{-1}$  frequencies in the model. The calculated results of Raman-active modes in Table 4.4.2 may be too low in intensity (relative to the background) to be observed in the Raman scattering experiments.

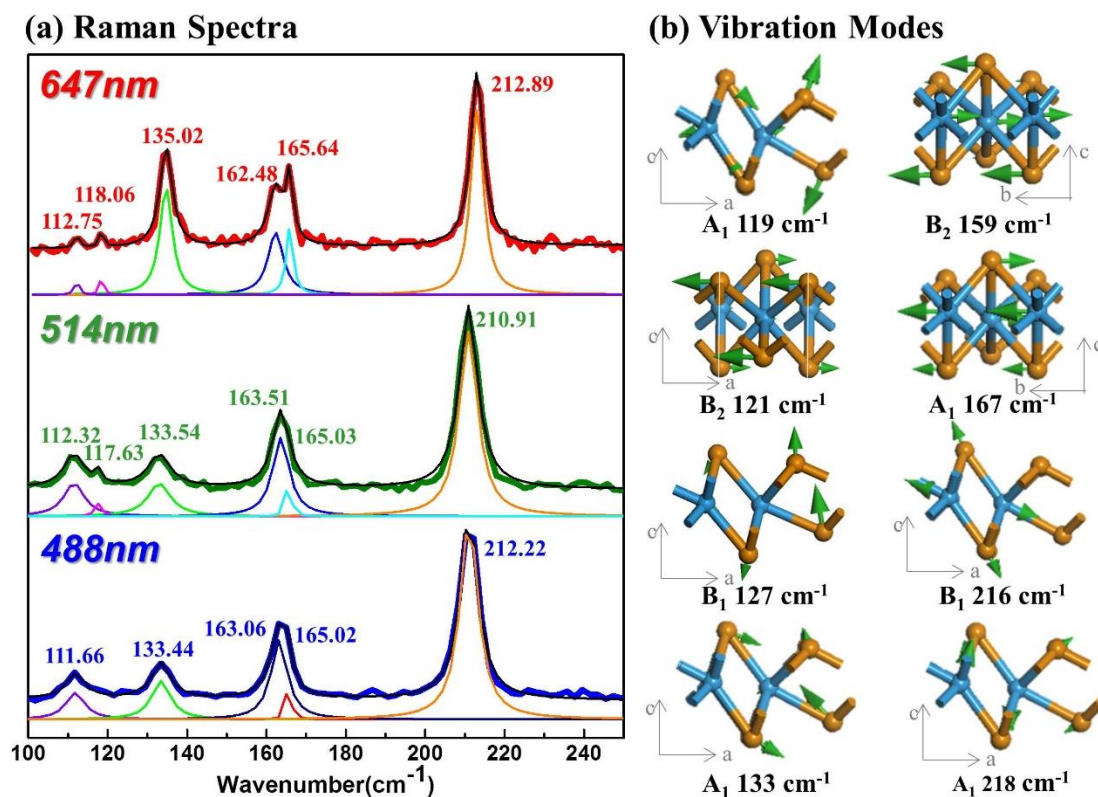


**Figure 3.3.1. (a) Raman spectra of Td-WTe<sub>2</sub> using 647 (red), 514 nm (green) and 488 nm (blue) laser excitation. The peaks in the spectra can be assigned to in-plane and**

out-of-plane (b) Raman-active vibrational modes obtained from vibration analysis done by DFT calculation. The major peaks were processed with Lorentzian peak fitting in both spectra, and the two distinct in-plane vibrational modes at 162 and 167  $\text{cm}^{-1}$  were deconvoluted in the spectrum obtained with 647nm excitation.

### 3.4 Layered Thickness

The single layer thickness of tungsten ditelluride was important to identify the number of layers for exfoliated sample. Although the theoretical models and XRD results can give us a basic ideas about the single layer thickness of  $\text{WTe}_2$ , it is still very important to obtain and confirm the single-layer thickness experimentally. Atomic force microscopy (AFM) obtained from multiple exfoliated  $\text{WTe}_2$  flakes in Figure 3.4.1 have verified the single-layer thickness of  $\text{WTe}_2$  is approximately  $7\text{\AA}$ . This experimental result is comparable to  $6.89\text{\AA}$  from the single-layer thickness of theoretical model and then later is used to identify the amount of layers for exfoliated sample.

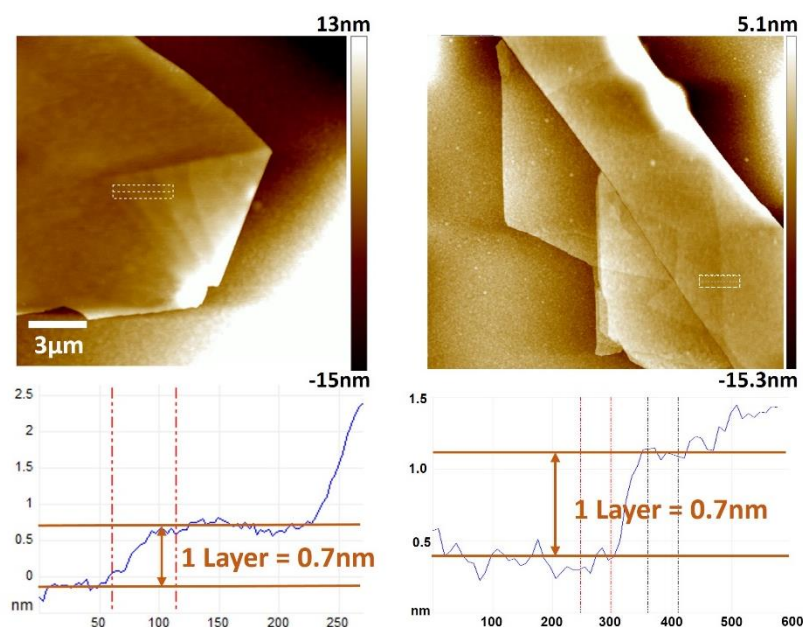


Figure 3.4.1. Atomic force microscopy results from exfoliated tungsten ditelluride flakes. The single-layered thickness of  $\text{WTe}_2$  around 0.7nm (7Å ) was obtained from AFM analysis of multiple exfoliated flakes.

### 3.5 Electronic Properties

Electronic properties of synthetic tungsten ditelluride was confirmed by temperature dependent resistance measurements. Freshly exfoliated thick (9 - 130 layers in Figure 3.5.1) Td- $\text{WTe}_2$  flakes were prepared for resistance versus temperature measurements to avoid degradation. Two-terminal device structures were fabricated using titanium-gold electrodes as shown in SEM images in Figure 3.5.2(a), (b) and (c). The thickness for each flake was measure by AFM (shown in Figure 3.5.2(a), (b) and (c)) after the resistance measurements.

The series contact resistance was found to be  $6.76 \times 10^{-5} \Omega \cdot \text{cm}$  using a transmission line measurement (TLM),<sup>90</sup> and was subtracted from the total measured resistance. Figure 3.5.2(d) shows the temperature-dependent resistivity, which varies between  $1 \times 10^{-3}$  and  $7 \times 10^{-3} \Omega \cdot \text{cm}$  at 300K, depending on the layer thickness. The different values obtained at different layer thicknesses suggest that the layer structure may affect carrier transport though Td- $\text{WTe}_2$ . Importantly, the resistivity of  $\text{WTe}_2$  is strongly correlated to temperature, increasing with increasing temperature over most of the range measured. The positive temperature dependence of the resistivity and the bulk resistivity values, which are  $\sim 2$  orders of magnitude higher than those of ordinary metals at 300K,<sup>91</sup> are consistent with the calculation that Td- $\text{WTe}_2$  is metallic in nature. We note that while two-terminal measurements do not provide direct access to the carrier concentration, and therefore confirmation of semi-metallic  $\text{WTe}_2$ , they are sufficient to verify that Td- $\text{WTe}_2$  is not

semiconducting – a critical point for the device community when considering this material in electronic device architectures.

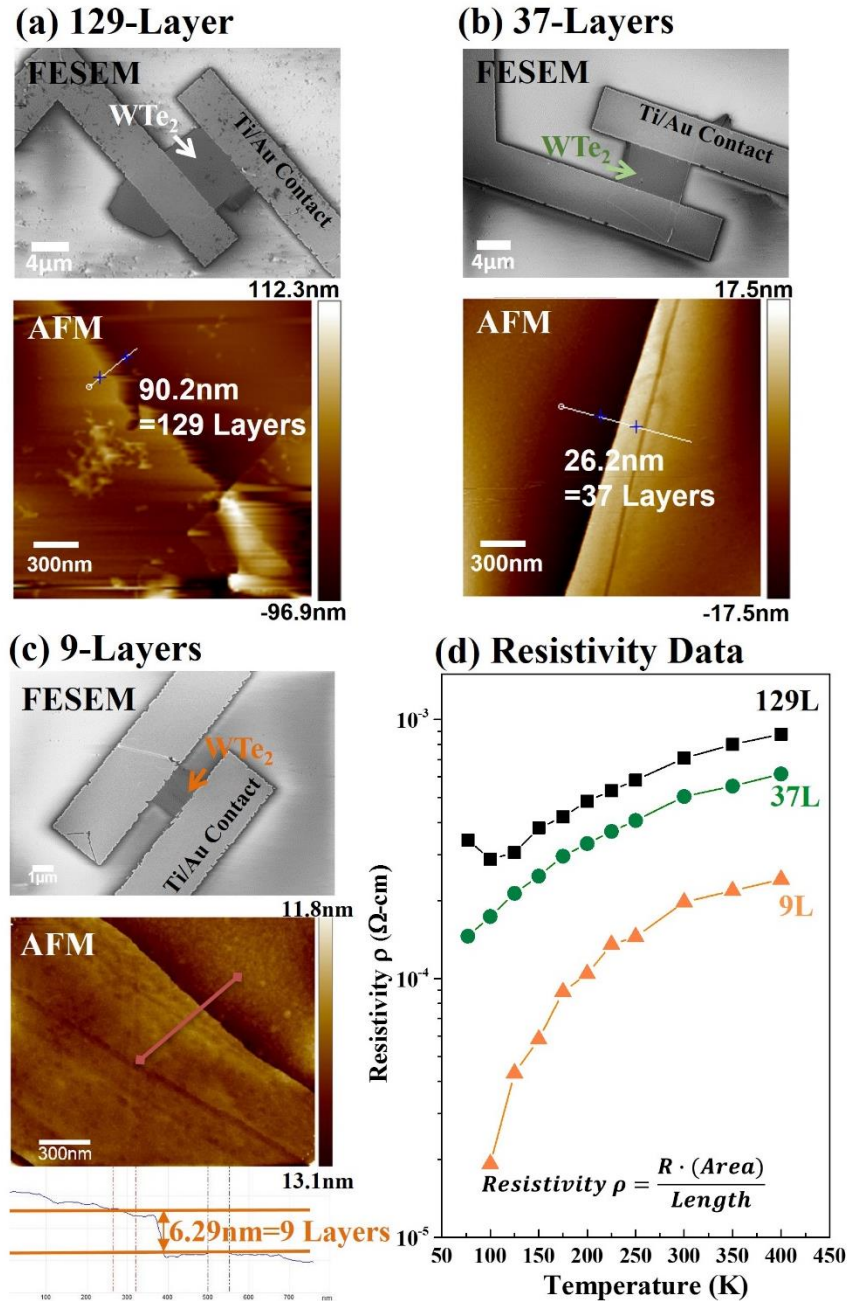


**Figure 3.5.1. SEM and AFM images of (a) 129-Layer (129L), (b) 37-Layer (37L) and (c) 9-layer (9L) Td-WTe<sub>2</sub> Resistivity measurements as a function of temperature (d)**

confirm that Td-WTe<sub>2</sub> is metallic in nature (resistivity proportional to temperature), rather than the semiconducting behavior recently suggested<sup>27,31,34,35</sup>.

The resistivity versus temperature data is the only experimental proof for the metallic-like characteristic of WTe<sub>2</sub>. However, the slope of the resistivity dependence of temperature is not a straight line as it usually is for metallic materials. Our resistivity data at 300K are also comparable to other data reported in the literature, listed in Table 3.5.1.

**Table 3.5.1. WTe<sub>2</sub> Resistivity ( $\rho$ ) Data at 300K Compared to the Literature**

Journal Article, Year	Resistivity Data @300K
	$\rho$ ( $\Omega\cdot\text{cm}$ )
Brixner et al., <i>J. Inorg. Nuci. Chem.</i> , 1962 <sup>92</sup>	$2.87 \times 10^{-3}$
E. Revolinsky et al, <i>J. Appl. Phys.</i> , 1964 <sup>42</sup>	$2.5 \times 10^{-3}$
S. Kabashima, <i>J. Phys. Soc. Japan</i> , 1966 <sup>58</sup>	$0.75 \times 10^{-3}$
S. K. Srivastava et al., <i>J. Mat. Sci.</i> , 1985 <sup>23</sup>	$2.5 \times 10^{-3}$
J. Callanan et al., <i>J. Chem. Thermo.</i> , 1992 <sup>59</sup>	$2.87 \times 10^{-3}$
J. Augustin et al., <i>Phys. Rev. B.</i> , 2000 <sup>93</sup>	$0.44 \times 10^{-3}$
M.N. Ali et al, <i>Nature</i> , 2014 <sup>94</sup>	$6 \times 10^{-4}$
<b>Current Work</b>	<b><math>7.09 \times 10^{-4}</math></b>

### 3.6 Stability of Tungsten Ditelluride

#### 3.6.1 XPS Analysis

Stability of  $\text{WTe}_2$  is a critical aspect of robust operation in a variety of applications. In the case of exfoliated flakes, the Raman spectra evolved with time during the data collection process, indicating that environmental sensitivity must be considered. Surface characterization tools such as XPS and Raman spectroscopy were used to understand surface stability and sensitivity to ambient conditions. Figure 3.6.1 summarizes the high-resolution XPS, which compare fresh exfoliated  $\text{WTe}_2$  with  $\text{WTe}_2$  that was exposed to ambient (air, 1 atmosphere, room temperature) conditions for extended periods of time. The XPS peak positions of the fresh exfoliated and aged  $\text{WTe}_2$  surfaces are listed in Table 3.6. Each XPS spectrum was calibrated with the carbon C 1s binding energy (BE) position and corrected with instrumental relative sensitivity factors (R.S.F.) for each element. For the high resolution elemental XPS spectrum, normalization of intensities was used to compare spectra collected from the same exfoliated  $\text{WTe}_2$  sample with increasing exposure time to air. Note that W 4f region is not used here due to the overlap with Te 4d region at lower BE area. Elemental XPS analysis reveals the evolution of a secondary chemical bond in the Te 3d peaks corresponding to an increase in Te-O binding. The primary degradation appears to be the formation of Te-O bonds, which is accompanied by a significant increase in the intensity of the O 1s peak, and formation of a small energy loss peak at the left shoulder of the W 4d region. This indicates that the  $\text{WTe}_2$  surface is air sensitive, which could affect the surface stability of few-layer exfoliated  $\text{WTe}_2$  flakes, and the oxygen contents keeps increasing with increase of exposure time. This also indicate that for the measurements for exfoliated  $\text{WTe}_2$  flakes, samples would need to be prepared freshly to avoid surface degradation with oxygen or ambient exposure. Table 3.6 lists the binding energies from peak fitting analysis of the Te 3d, O1s and W 4d regions of the spectra of  $\text{WTe}_2$  and surface-degraded (or oxidized)  $\text{WTe}_2$ . There are two sets of Te 3d<sub>3/2</sub> and Te

3d<sub>5/2</sub> binding energies from comparison between normalized high-res Te spectra and our peak fitting analysis, which refer to the Te 3d binding energies of the fresh exfoliated WTe<sub>2</sub> surface and those of TeO<sub>2</sub> from the NIST XPS database.<sup>51</sup> These peak positions correlate well with those of TeO<sub>2</sub>, and confirm the formation of Te-O bonds under accelerated aging, suggesting this as the mechanism of degradation for Td-WTe<sub>2</sub> when exposed to air or a combination of photons and air.<sup>52</sup>

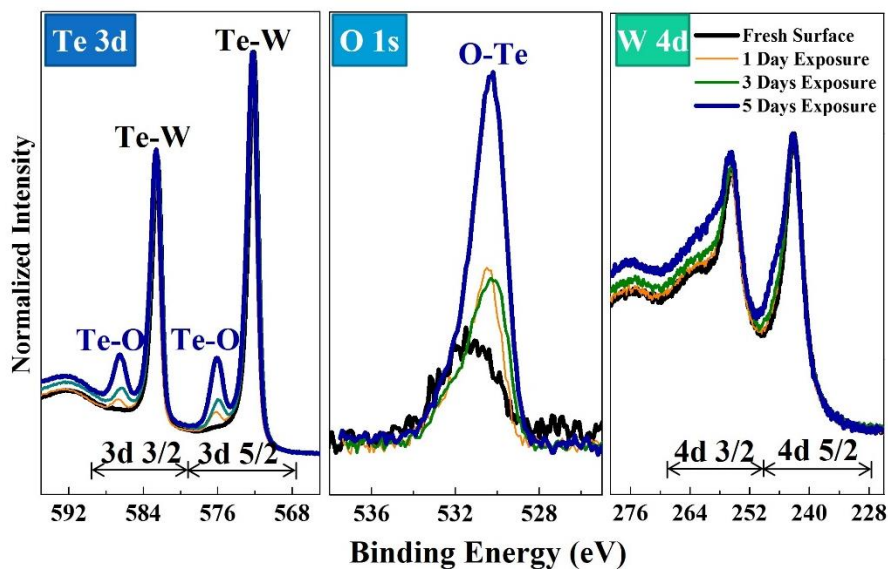


**Figure 3.6.1.** Stability testing of WTe<sub>2</sub> flakes in ambient air by high-resolution elemental XPS spectra. XPS analysis reveals an increase in Te-O bonding in the Td 3d and O 1s spectra with minor changes in the W 4d spectra, indicating the formation of TeO<sub>2</sub> on the surface.



**Table 3.6. XPS analysis and peak fitting data for WTe<sub>2</sub> and degraded WTe<sub>2</sub> surface.**

Region/Sample	Te 3d				O 1s		W 4d	
	Te 3d3/2		Te 3d5/2				W 4d3/2	W 4d5/2
	WTe <sub>2</sub>	TeO <sub>2</sub>	WTe <sub>2</sub>	TeO <sub>2</sub>	-	TeO <sub>2</sub>		
<b>(1) Fresh exfoliated WTe<sub>2</sub> surface</b>	582.51	-	572.12	-	531.43	-	255.41	243.10
<b>(2) WTe<sub>2</sub> surface with 5 days exposure to air</b>	582.64	586.60	572.22	576.10	531.44	530.23	255.80	243.47

### 3.6.2 Raman Analysis

Raman spectra from 647nm laser excitation revealed deconvoluted vibration modes compared to results from 488nm and 514nm laser, it was used to detect the degradation of WTe<sub>2</sub> sample surfaces. All of aged WTe<sub>2</sub> samples were stored in ambient environment and collected Raman spectra using three period of 20 seconds acquisition time under 647nm laser illumination. Figure 3.6.2(a) shows that the aged bulk WTe<sub>2</sub> surface have minor changes in intensities of the in-plane vibrational modes near the 162-167cm<sup>-1</sup> region, whereas the significant increase in intensities of the in-plane modes for the aged thin (~2-4 layers thick) WTe<sub>2</sub> flakes. This results suggest the instability of exfoliated WTe<sub>2</sub> flakes that the surfaces of exfoliated samples may change with time and storage environment.

However, when we correlate our XPS results to Raman results, Raman spectroscopy may not be able offer the degradation correlates to oxygen exposure on the sample surfaces. Hence, degradation of WTe<sub>2</sub> samples was expedited by laser degradation. During our experimental work, it is found that with extended longer illumination time and strong laser illumination (ex. three periods of 45-60 seconds acquisition time using 647nm laser, or

using stronger laser excitation like 488nm or 514nm laser with 2 times of 20-30 acquisition time), WTe<sub>2</sub> surface is visibly modified (with burned holes on the surface). In Figure 3.6.2 (b), two new vibrational modes at 124 and 142cm<sup>-1</sup> which correlate to the formation of tellurium oxide (TeO<sub>2</sub>).

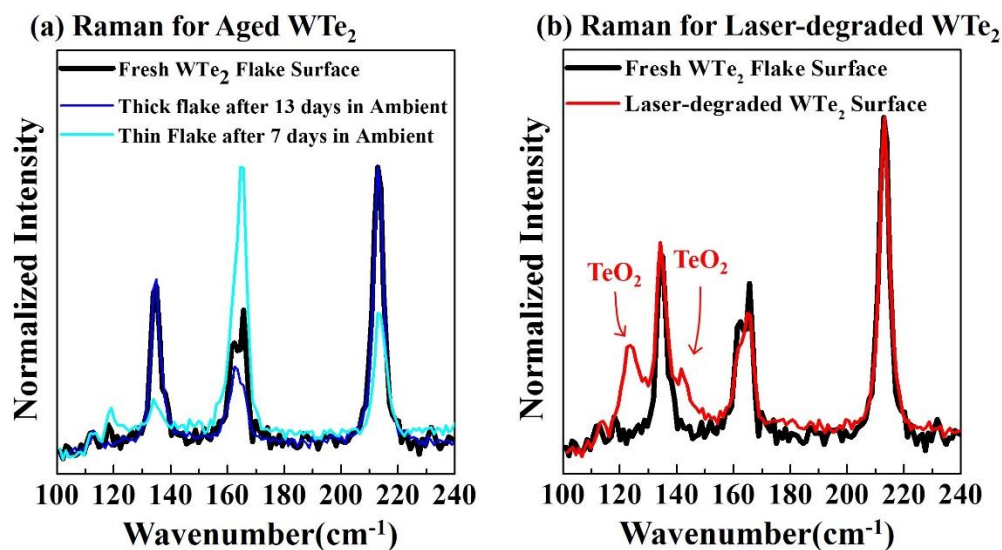


**Figure 3.6.2.** The Raman spectrum after 13 days of air exposure for aged WTe<sub>2</sub> samples in (a) shows the small intensities change in for bulk surface and a large increase for thin-layered samples for the two in-plane modes in the 160-167cm<sup>-1</sup> region. The Raman spectrum of a laser-degraded sample in (b) suggests that photon-assisted oxidation can lead to rapid degradation of WTe<sub>2</sub> via the formation of TeO<sub>2</sub>.

## Chapter 4.

### Theoretical Calculation of Tungsten Diterlluride (WTe<sub>2</sub>)

#### 4.1 Theoretical Calculation Setup

##### 4.1.1 Tungsten Ditelluride Model

Theoretical modeling of Tungsten ditelluride (WTe<sub>2</sub>) was essential to elucidate the electronic band structure and provide comparable details for experimental work. Hypothetical 2H-WTe<sub>2</sub> in hexagonal crystal structure P6<sub>3</sub>/mmc (point group D<sub>6h</sub>) was built based on the lattice parameters and atomic positions provided in Kumar et al.<sup>34,35</sup> and Ding et al<sup>25</sup> which were originally transferred from 2H-MoS<sub>2</sub> models. Td-WTe<sub>2</sub> models in orthorhombic crystal structure Pmn2<sub>1</sub> (point group C<sub>2v</sub>) used in this work were based on calculated atomic coordinates of WTe<sub>2</sub> XRDdata reported by multiple articles<sup>55,57,96</sup> in Table 4.1.1 collected from The International Centre for Diffraction Data (ICDD) Database.<sup>97</sup> The early papers by Brixner L. H. et al<sup>92</sup> and Brown B.E.<sup>57</sup> reported and calculated the atomic positions of synthesized WTe<sub>2</sub> crystals, while Mentzen B.F. et al<sup>96</sup> and Mar A., et al<sup>55</sup> from ICDD database further updated the space group to Pmn2<sub>1</sub> by following priority rule of Hermann-Mauguin notation.<sup>98</sup> This priority rule in crystallography indicates that a mirror plane has priority over an n-glide plane, whereas the point group remains the same, which means the energy calculation after geometry optimization and convergence tests maintained equally effective. Therefore, though our original models of Td-WTe<sub>2</sub> were based on the first credible atomic positions in Pmn2<sub>1</sub> structure reported by Brown B. E.<sup>57</sup> in 1966, our depiction of the unit cell and K-paths for

band structure calculations have later been updated accordingly to Pmn2<sub>1</sub>, which remained space group number (31), point group C<sub>2v</sub>.

**Table 4.1.1. Experimental Td-WTe<sub>2</sub> Lattice Parameters from ICDD Database**

Reference	PDF#	Space Group	Lattice Parameters (Å)		
			a	b	c
Brixner L.H. et al, 1962 <sup>92</sup>	04-004-9139	(31) P21mn	14.028	3.495	6.27
Brown B.E., 1966 <sup>57</sup>	04-007-9333	(31) Pnm21	6.282	3.496	14.073
Opalovski A. A. et al, 1970	04-004-5951	(31) Pmn21	3.483	6.278	14.054
Obolonchik V.A. et al, 1972	04-003-6079	(31) Pmn21	3.489	6.285	14.080
Mentzen B.F. et al, 1976 <sup>96</sup>	04-003-2315	(31) Pmn21	3.483	6.265	14.043
Mar A., et al, 1992 <sup>55</sup>	04-007-0799	(31) Pmn21	3.477	6.249	14.018

The original crystal data and unit cell parameters of the 2H- and Td-WTe<sub>2</sub> initial crystal structures are listed in Table 4.1.2. The initial atomic coordinates of the tungsten and tellurium atoms in the 2H- and Td-WTe<sub>2</sub> unit cells are also included in Table 4.1.2. WTe<sub>2</sub> single crystal models in 2H and Td structure with their reciprocal space are shown in Figure 4.1.1.

**Table 4.1.2. 2H- and Td-WTe<sub>2</sub> initial crystal structures.**

2H Structure <sup>34,35</sup>			Td Structure <sup>57</sup>			
Crystal System	Hexagonal		Orthorhombic			
Space Group	P6 <sub>3</sub> /mmc		Pmn2 <sub>1</sub>			
Point Group	D <sub>6h</sub>		C <sub>2v</sub>			
Unit Cell Parameters						
	a(Å )	b(Å )	c(Å )	a(Å )	b(Å )	c(Å )
	3.60	3.60	14.18	3.50	6.28	14.07
Initial Coordinates						
Atoms	u	v	w	U	v	W
W 1	0.3333	0.6667	0.2500	0.5000	0.9005	0.0000
W 2	0.6667	0.3333	0.7500	0.0000	0.0995	0.5000
W 3		n/a		0.0000	0.5414	0.9851
W 4		n/a		0.5000	0.4586	0.4851
Te 1	0.3333	0.6667	0.6210	0.5000	0.2941	0.0965
Te 2	0.6667	0.3333	0.1210	0.5000	0.8517	0.3893
Te 3	0.6667	0.3333	0.3790	0.0000	0.7059	0.5965
Te 4	0.3333	0.6667	0.8790	0.0000	0.1483	0.8893
Te 5		n/a		0.0000	0.8002	0.1400
Te 6		n/a		0.0000	0.3559	0.3449
Te 7		n/a		0.5000	0.1998	0.6400
Te 8		n/a		0.5000	0.6441	0.8449

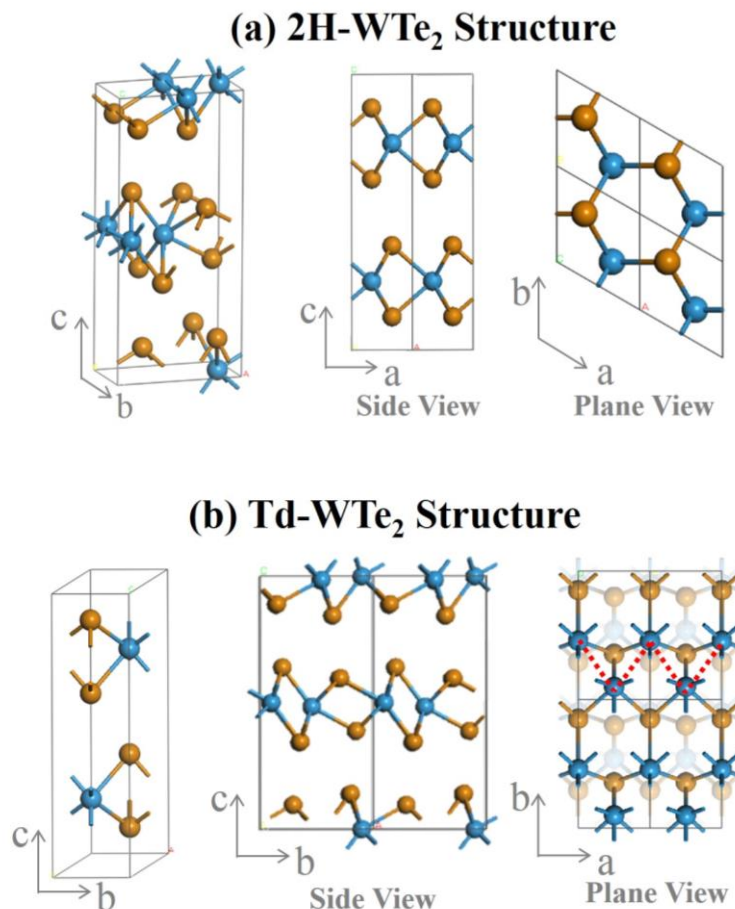


**Figure 4.1.1. Single crystal structures, side view and plane view of (a) hexagonal 2H-WTe<sub>2</sub>; (b) orthorhombic Td-WTe<sub>2</sub> theoretical models.**

Geometry optimization of the initial structures was followed by the calculation of their electronic structures, vibrational properties, as well as enthalpies of formation as function of pressure, within Density Functional Theory (DFT), as implemented in CASTEP<sup>99</sup> in Materials Studio, Accelrys (accelrys.com), as well as in Quantum Espresso 5.1.<sup>100</sup> The Local Density Approximation (LDA) as parameterized by Perdew and Zunger<sup>101,102</sup> was selected for exchange and correlation functional, and dispersion corrections were implemented following the semi-empirical Grimme method (LDA+DFT-D).<sup>103,104</sup> Norm-

conserving pseudopotentials were used for all the elements. The relaxed LDA coordinates of the tungsten and tellurium atoms in the 2H- and Td-WTe<sub>2</sub> unit cells are also included in the bottom part of Table 4.1.3. Since WTe<sub>2</sub> layers are bound by weak van der Waals (vdW) interaction, we also performed a structural optimization using the Grimme method for van der Waals corrections,<sup>103,104</sup> but it was observed that LDA yields a better description of the stacking distance, as summarized in Table 4.1.3. The relaxed WTe<sub>2</sub> models are further used for extract information of materials properties and vibration modes.

**Table 4.1.3. DFT Calculation results of WTe<sub>2</sub> in different crystal structures**

WTe <sub>2</sub> Structures	2H			Td		
Bulk Model	Lattice Parameters			Lattice Parameters		
	a	b	c	a	b	c
LDA CA-PZ	3.49	3.49	13.78	3.46	6.24	13.73

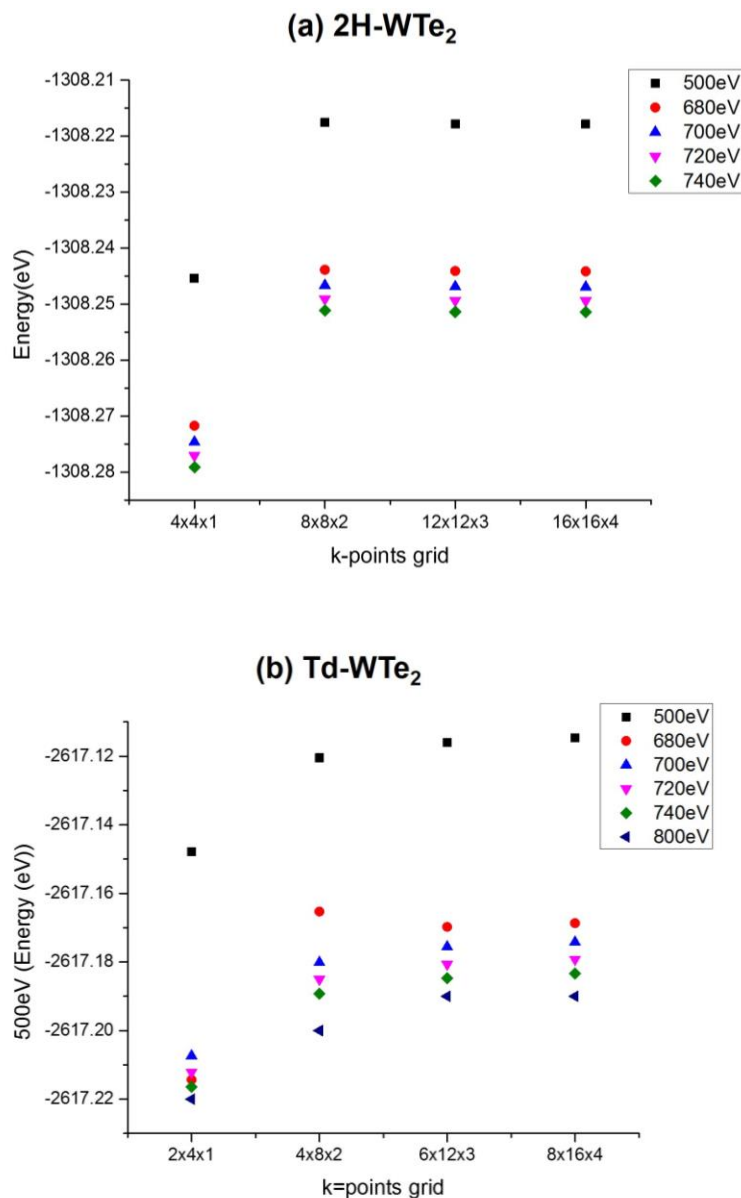
  

Atoms	Relaxed Coordinates					
	u	v	w	u	v	w
W 1	0.3333	0.6667	0.2500	0.5000	0.8998	0.0007
W 2	0.6667	0.3333	0.7500	0.0000	0.1002	0.5007
W 3		n/a		0.0000	0.5414	0.9845
W 4		n/a		0.5000	0.4586	0.4845
Te 1	0.3333	0.6667	0.6190	0.5000	0.2936	0.0965
Te 2	0.6667	0.3333	0.1190	0.5000	0.8526	0.3889
Te 3	0.6667	0.3333	0.3810	0.0000	0.7074	0.5964
Te 4	0.3333	0.6667	0.8810	0.0000	0.1474	0.8889
Te 5		n/a		0.0000	0.7976	0.1433
Te 6		n/a		0.0000	0.3547	0.3419
Te 7		n/a		0.5000	0.2024	0.6433
Te 8		n/a		0.5000	0.6453	0.8419

### 4.1.2 Convergence Study

The 2H-WTe<sub>2</sub> and Td-WTe<sub>2</sub> models have conducted convergence test in order to reach the optimum calculation time and settings on cut-off energy and k-points grid for further calculation. Total energies relaxed by LDA CA-PZ in CASTEP using combination of (1) cut-off energy of the plane wave basis set at 500eV, 680eV, 700eV, 720eV, 740eV, for both 2H- and Td-WTe<sub>2</sub>, and up to 800eV for Td-WTe<sub>2</sub>; with (2) Monkhorst-Pack k-points grid of from 2x4x1, 4x8x2, 6x12x3, to 8x16x4 for Td-WTe<sub>2</sub>; 4x4x1, 8x8x2, 12x12x3, 16x16x4 for 2H-WTe<sub>2</sub> sampling of the Brillouin zone are used for convergence analysis. Convergence test results on total energy for 2H- and Td-WTe<sub>2</sub> models are shown in Figure 4.1.3. The cut-off energy 740eV was chosen for both 2H- and Td-WTe<sub>2</sub> models from the lowest computation time, and lowest fluctuation in total energy results. Sampling size on k-points grids of 8x16x4 for Td-WTe<sub>2</sub> and 16x16x4 for 2H-WTe<sub>2</sub> were selected considering the balance between results validity and the cost of calculation time.





**Figure 4.1.3. The convergence results from low to high cutoff energy with small to large k-points grid for (a) 2H-WTe<sub>2</sub> and (b) Td-WTe<sub>2</sub>.**

Under these computational conditions the total energy and band gaps were converged to 0.1 meV. Geometrical optimizations were performed for both the LDA and LDA plus DFT-D functions until the structures reached configurations with energy differences of  $5 \times 10^{-6}$  eV/atom, and forces were less than 0.01 eV/Å.

### 4.3 Calculation Results and Discussion

#### 4.3.1 Crystal Structures

The 2H-WTe<sub>2</sub> structure (Figure 4.1.2(a)) has hexagonal symmetry. The upper and lower tellurium atoms are bonded to a central W atom, forming a trigonal prismatic arrangement similar to that found in 2H-MoS<sub>2</sub> and 2H-WSe<sub>2</sub>.<sup>21,105</sup> The Td-WTe<sub>2</sub> structure (Figure 4.1.2(b)) is similar to that of the 1T polytype, in which the upper tellurium atoms are rotated by 180° with respect to the lower tellurium atoms, forming W-centered octahedra. However, in Td-WTe<sub>2</sub> the tungsten atoms are shifted by 0.87 Å in the layer plane and 0.15 Å in the perpendicular direction (along the c-axis) from the center of the octahedron. This shift of tungsten atoms results from a shortened metal-metal distance in transition metal tellurides<sup>106</sup> due to strong intermetallic bonding.<sup>55,93</sup> As a consequence, the tungsten atoms are unequally spaced and form a zigzag chain along the a-axis (Figure 4.1.2(b)). The distances between tungsten atoms in Td-WTe<sub>2</sub> alternate along the b-axis at 2.862 and 4.394 Å, in contrast to the 2H phase where they are equally spaced at a distance of 3.6 Å. Additionally, the tellurium atoms are no longer coplanar, but instead exhibit a zigzag structure with 0.6 Å c-axis variation in atomic positions. Finally, the tungsten–tellurium bond lengths are also uneven at 2.719 and 2.815 Å, compared to a uniform 2.769 Å for 2H-WTe<sub>2</sub>. These changes in bonding environment result in the lowering of the lattice symmetry from hexagonal to orthorhombic. Te-W-Te angles in Figure 4.3.1 also shown within the Te layers are 75.7° and 83.3° for the upper Te layer and 81.9° and 80.2° for the lower Te layer; the analogous bond angle is 81.1° in 2H-WTe<sub>2</sub>. The upper Te-W-lower Te bond angles are 77.4°, 97.8° and 116.1° compared to equivalent 82.7° angles in the 2H structure.

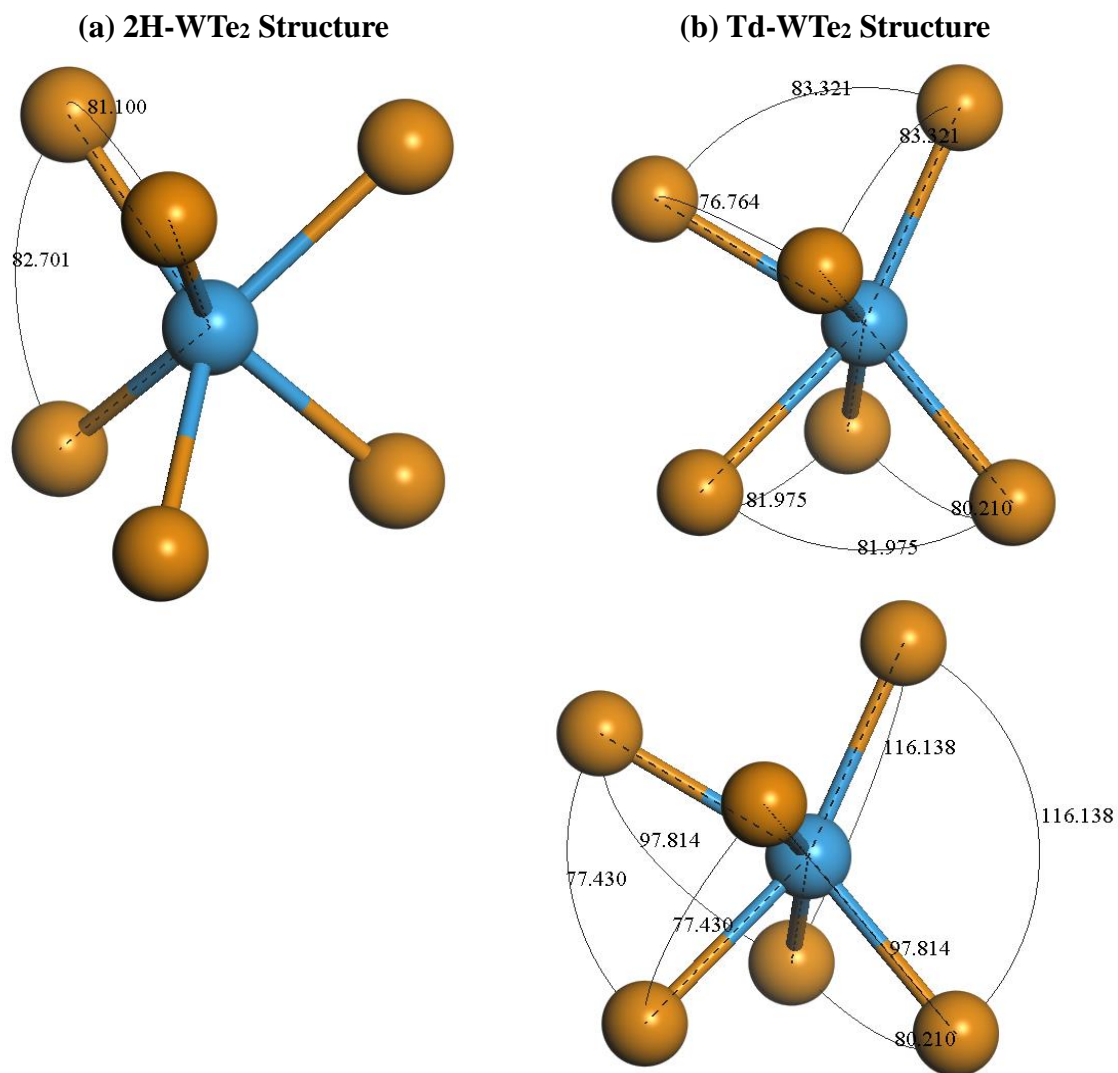


**Figure 4.3.1. Te-W-Te bond angles in the (a) 2H-WTe<sub>2</sub> and (b) Td-WTe<sub>2</sub> structures.**

The crystal structure plays a significant role in the characteristic electronic properties of WTe<sub>2</sub>. Based on the optimized structures of 2H- and Td-WTe<sub>2</sub>, we have calculated the electronic full band structures displayed in Figure 4.3.2, and band gap and magnified band structure details are summarized in Figure 4-6. The band structure and density of states

(DOS) of 2H-WTe<sub>2</sub> is shown in Figure 4.3.3(a) and (b). The *d*-orbitals of tungsten split into three different bands and the 2H-WTe<sub>2</sub> trigonal prismatic coordination gives rise to a calculated 0.702 eV bandgap. In contrast, the magnified band structure in Figure 4.3.3(c) of band-crossing, combined with the result of low DOS at the Fermi energy of bulk Td-WTe<sub>2</sub> in Figure 4.3.3(d) shows that it is a semimetal, with few bands crossing the Fermi energy in the three main axes of the Brillouin zone. The highest valence band bends upward while the lowest conduction band bends downward to form a 0.21 eV overlap, confirming the findings of Augustin *et al.*<sup>93</sup> A detailed calculation of the band structure around the crossing point in the  $\Gamma$ X segment shows an indirect band overlap of 0.3 eV, with a separation of 11 meV among the bands at their closest point (see inset in Figure 4.3.3(b)), which is well below the thermal energy at room temperature (25 meV).

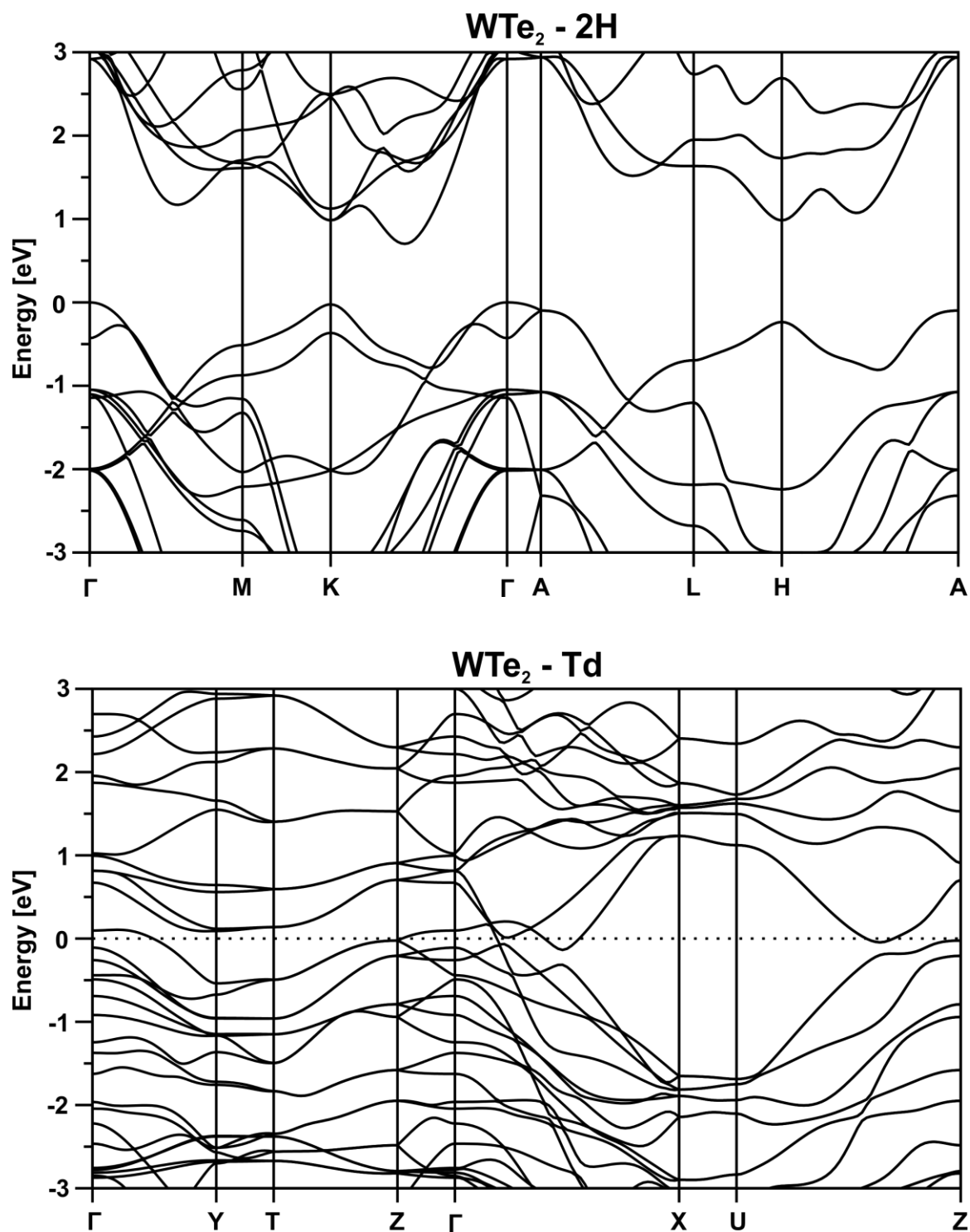
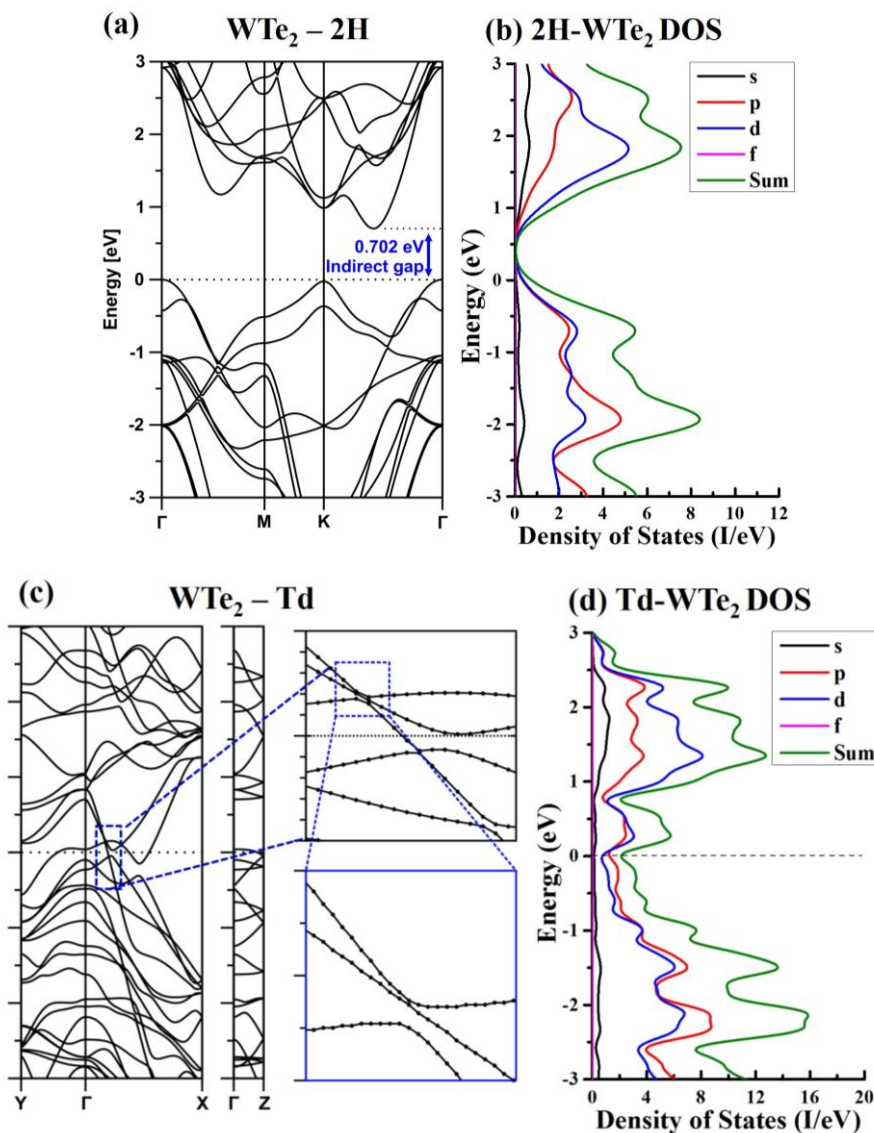


Figure 4.3.2. Full electronic band structure for the hexagonal (2H) phase (top), and the distorted tetragonal (Td) phase (bottom) of  $\text{WTe}_2$ .



**Figure 4.3.3.** The electronic band structures (a) and (b) density of states both indicate that bulk  $\text{WTe}_2$  in the 2H structure has an indirect 0.702 eV bandgap. Bulk  $\text{WTe}_2$  in the Td structure (c) has a 0.21 eV band overlap in  $\Gamma$ -X, and the density of states (d) reaches a minimum, but never goes to zero near Fermi level.

It is known that the local density approximation (LDA) in DFT tends to overbind chemical interactions, resulting in bonds (and lattice parameters) that are usually 1-2% shorter,<sup>107</sup> and for van der Waals interactions this overbinding can be slightly larger, and it

provides an excellent description of the vibrational properties. Our final lattice parameters listed in Table 4.3.1 were 3.46 (-1.14%), 6.24 (-0.6%), and 13.73 (-2.4%) for Td-WTe<sub>2</sub>, which are well within the expected accuracy for DFT-LDA. The LDA plus the semi-empirical Grimme method (LDA+DFT-D) employs a semi-empirical correction of the electrostatic potential that results in a larger overbinding in the c-axis, which leads to a smaller lattice parameter for c-axis. But when we check band structure in different pathways in Brillouin zone, results from DFT-D semi-empirical correction lead to a wider band separation, which could be a useful observation for resolving band overlap for van der Waal solid interaction in c-direction. Figure 4.3.4 displays the comparison between LDA and LDA plus DFT-D band structure in Brillouin zone path. The band structure of Td-WTe<sub>2</sub> models calculated by LDA+DFT-D ( $\Gamma$ -X in Figure 4.3.4(c) and  $\Gamma$ -S in Figure 4.3.4(f)) all show wider band separation than the results calculated by LDA ( $\Gamma$ -X in Figure 4.3.4(b) and  $\Gamma$ -S in Figure 4.3.4(d)); however, the results for c-axis lattice constant is smaller for LDA plus DFT-D (Table 4.3.1). As a result, DFT-D correction can be used for calculating band structure for solving overbinding caused by “pure” LDA, but may not be reasonable for semimetal Td-WTe<sub>2</sub> calculation. Hence we only employ the models geometrically optimized by LDA to state the crystal structure and further materials properties but not employing such corrections for semimetal Td-WTe<sub>2</sub>. Here we suggest that while there are other methods that might provide increased accuracy in van der Waals interactions, the high computational cost associated with these methods is not justified given that we already have an excellent agreement in bond lengths and stacking distance. The validity of a model resides in its capacity to explain and predict experimental phenomena, being careful to stay within the bounds and limitations of such model. In our case, we have been careful to stay within the bounds of DFT-LDA.

**Table 4.3.1. Comparison between LDA (CA-PZ) and LDA with semi-empirical Grimme method (LDA+DFT-D) calculation for results of the geometric optimized WTe<sub>2</sub> crystal lattice parameters and bandgap (E<sub>g</sub>) in 2H and Td crystal structures**

WTe <sub>2</sub> Structures	2H				Td			
	Lattice Parameters			Bandgap, E <sub>g</sub> (eV)	Lattice Parameters			Bandgap, E <sub>g</sub> (eV)
	a	b	c		a	b	c	
<b>LDA CA-PZ</b>	3.49	3.49	13.78	0.706	3.46	6.24	13.73	0
<b>LDA+DFT-D</b>	3.47	3.47	13.61	0.630	3.46	6.25	13.43	0

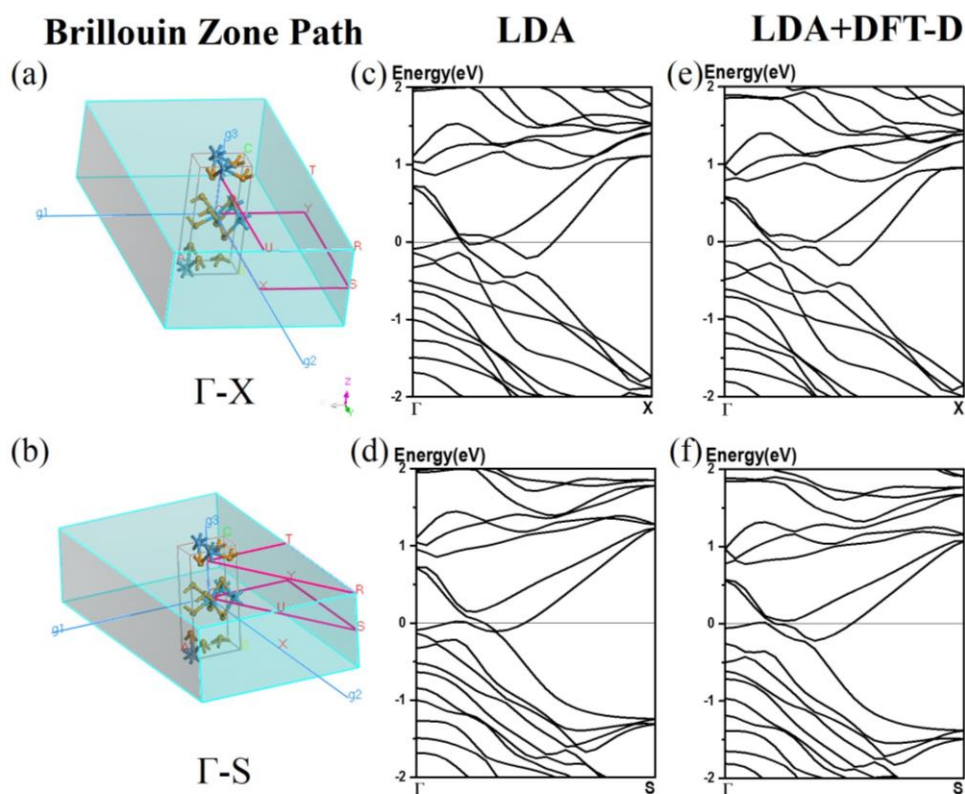


**Figure 4.3.4. Comparison of the band structure in different Brillouin Zone Path (a)  $\Gamma$ -X and (b)  $\Gamma$ -S with LDA and LDA plus DFT-D for Td-WTe<sub>2</sub>. Band separation from LDA to LDA plus DFT-D along different path can be observed when comparing (c) and (d) with (e) and (f).**



## 4.4 Materials Properties Calculation

### 4.4.1 X-ray Diffraction Patterns

We have analyzed our  $\text{WTe}_2$  experimental x-ray diffraction (XRD) patterns with the existed  $\text{WTe}_2$  diffraction patterns PDF#04-007-0799 in ICDD database, and confirmed the bulk  $\text{WTe}_2$  single crystal is orthorhombic crystal system. The theoretical XRD patterns of both Td- $\text{WTe}_2$  and 2H- $\text{WTe}_2$  are obtained from CASTEP results using relaxed models, shown in Figure 4.4.1 (b) and (c). They are then compared to experimental XRD pattern in Figure 4.4.1(a), showing the lattice planes (022) and (112) close to  $2\theta=32.5$ , and (023), (113), (024), and (122) across  $2\theta$  area from 35 to 42.5 from experimental XRD data closely matches with the theoretical results from our Td- $\text{WTe}_2$  model.

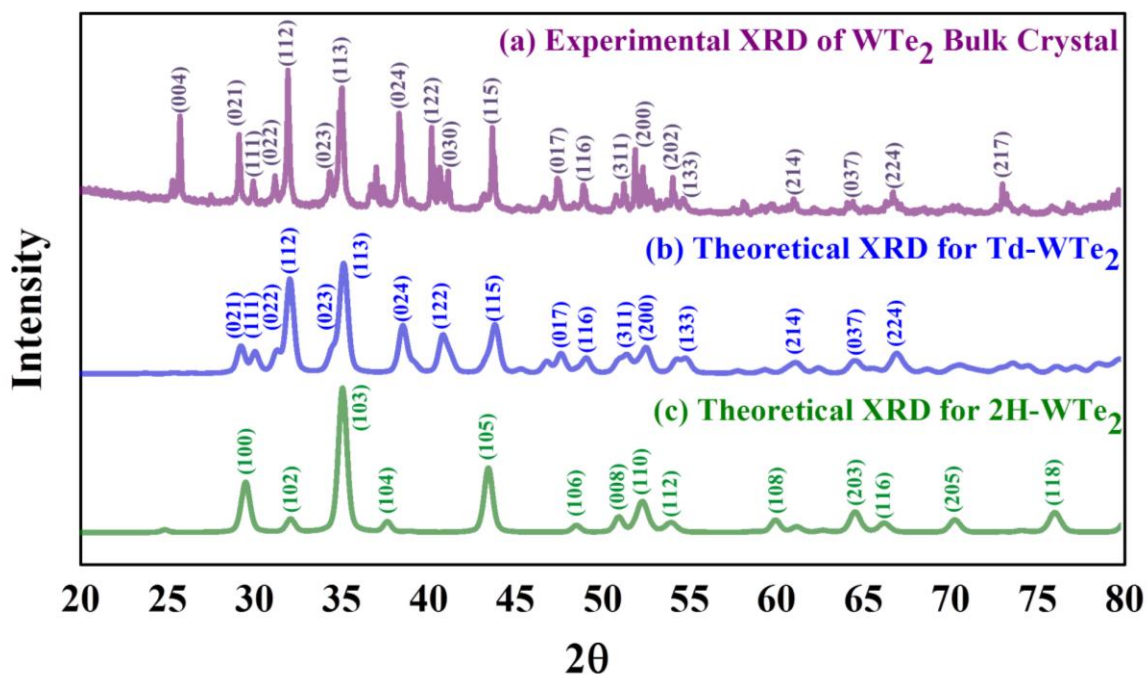


Figure 4.4.1. X-ray Diffraction Patterns for (a) experimental  $\text{WTe}_2$  bulk crystal; (b) theoretical Td- $\text{WTe}_2$ ; (c) theoretical 2H- $\text{WTe}_2$ .

#### 4.4.2 Raman Vibration Modes

We have used CASTEP to calculate Raman and IR active modes and spectrum. The cost of time (> 30 days) and resources was expensive to obtain successful output results for 2H- and Td-WTe<sub>2</sub>. For 2H-WTe<sub>2</sub> models, the Raman frequencies results using CASTEP are comparable to reported results<sup>25</sup> and refined by our calculation settings, listed in Table 4.4.2. However for Td-WTe<sub>2</sub>, even though we have obtained one successful result from CASTEP, Td-WTe<sub>2</sub> models have difficulties to reach convergence due to the band crossing and semimetal feature previously displayed in Figure 4.3.3. As a result, phonon frequencies and symmetry analysis of IR and Raman activities were calculated with DFPT<sup>89</sup> and listed in Table 4.4.2 in order to compare our experimental Raman spectrum for Td-WTe<sub>2</sub>. Vibration modes frequencies and motions analysis are used as the basis for peak fitting analysis for the experimental Raman results in Figure 3.3.1.

**Table 4.4.2. Calculated vibrational modes, symmetry classification, IR and Raman activities for 2H- and Td-WTe<sub>2</sub> structures. (A = active)**

2H-WTe <sub>2</sub>					Td-WTe <sub>2</sub>			
Mode	Frequency (cm <sup>-1</sup> )	Classification	IR- active	Raman- active	Frequency (cm <sup>-1</sup> )	Classification	IR- active	Raman- active
1					9	A <sub>1</sub>	A	A
2	28	E <sub>2g</sub>		A	25	B <sub>1</sub>	A	A
3	126	E <sub>1g</sub>		A	28	A <sub>2</sub>		A
4	183	A <sub>1g</sub>		A	73	A <sub>1</sub>	A	A
5	200	E <sub>2g</sub>		A	85	B <sub>1</sub>	A	A
6	201	E <sub>1u</sub>	A		91	B <sub>2</sub>	A	A
7	242	A <sub>2u</sub>	A		95	A <sub>2</sub>		A
8					115	A <sub>2</sub>		A
9					116	B <sub>2</sub>	A	A
10					119	A <sub>1</sub>	A	A
11					119	A <sub>2</sub>		A
12					121	B <sub>2</sub>	A	A
13					122	B <sub>1</sub>	A	A
14					127	B <sub>1</sub>	A	A
15					130	B <sub>1</sub>	A	A
16					133	A <sub>1</sub>	A	A
17					134	A <sub>1</sub>	A	A
18					137	A <sub>1</sub>	A	A
19					138	B <sub>1</sub>	A	A
20					159	B <sub>2</sub>	A	A
21					159	A <sub>2</sub>		A
22					164	B <sub>1</sub>	A	A
21					167	A <sub>2</sub>		A
22					168	B <sub>2</sub>	A	A
23					168	A <sub>1</sub>	A	A
24					181	B <sub>1</sub>	A	A
25					182	A <sub>1</sub>	A	A
26					216	A <sub>1</sub>	A	A
27					218	A <sub>1</sub>	A	A
28					220	B <sub>1</sub>	A	A
29					239	B <sub>1</sub>	A	A
30					239	A <sub>1</sub>	A	A

#### 4.5 Phase Transition of 2H- and Td- WTe<sub>2</sub>

To understand why the Td structure is favored, the enthalpies of formation of 2H and Td-WTe<sub>2</sub> were calculated within a pressure range near equilibrium, which is close to the condition of chemical vapor transport (CVT) synthesis. Under no experimental conditions that we are aware of has CVT been accomplished at greater than atmospheric pressure ( $1 \times 10^{-4}$  GPa). Traditionally, the synthesis occurs in the millitorr range ( $\sim 1 \times 10^{-8}$  GPa), therefore, the pressure range we have chosen is valid for describing the equilibrium properties of WTe<sub>2</sub>. We chose to extend the plot out to 0.6 GPa because it would cover all circumstances where WTe<sub>2</sub> could be grown at higher pressures (0.6 GPa = 87,000 psi =  $4.5 \times 10^6$  Torr = 5900 atm). As is evident from Figure 4.5.1, the enthalpy of formation for the Td structure is lower at equilibrium (zero pressure) by 0.58 eV per WTe<sub>2</sub> formula unit. This is also the case for non-equilibrium synthesis conditions up to at least 0.6 GPa.

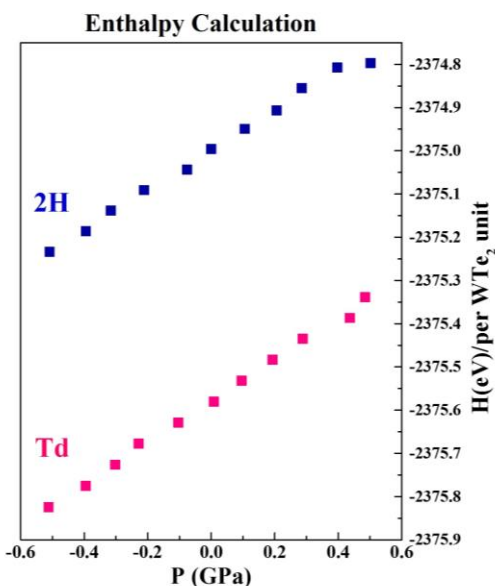


**Figure 4.5.1.** DFT calculation results indicates that the enthalpy of formation of the Td-WTe<sub>2</sub> phase is lower than that of the 2H phase, regardless of pressure, indicating it is the most stable form of bulk Td-WTe<sub>2</sub>.

Although pressure cannot promote phase transition of Td-WTe<sub>2</sub> to 2H-WTe<sub>2</sub>, it can induce superconductivity of WTe<sub>2</sub>. From recent study done by Pan et al.<sup>56</sup>, superconductivity can be introduced by applying a high pressure of 2.5GPa, and reach a maximum critical temperature ( $T_c$ ) at 7K at around 16.8GPa. Figure 4.5.2 summarized their findings of pressure-induced lattice constant strain (Figure 4.5.2(a)), and further boost the superconductivity.

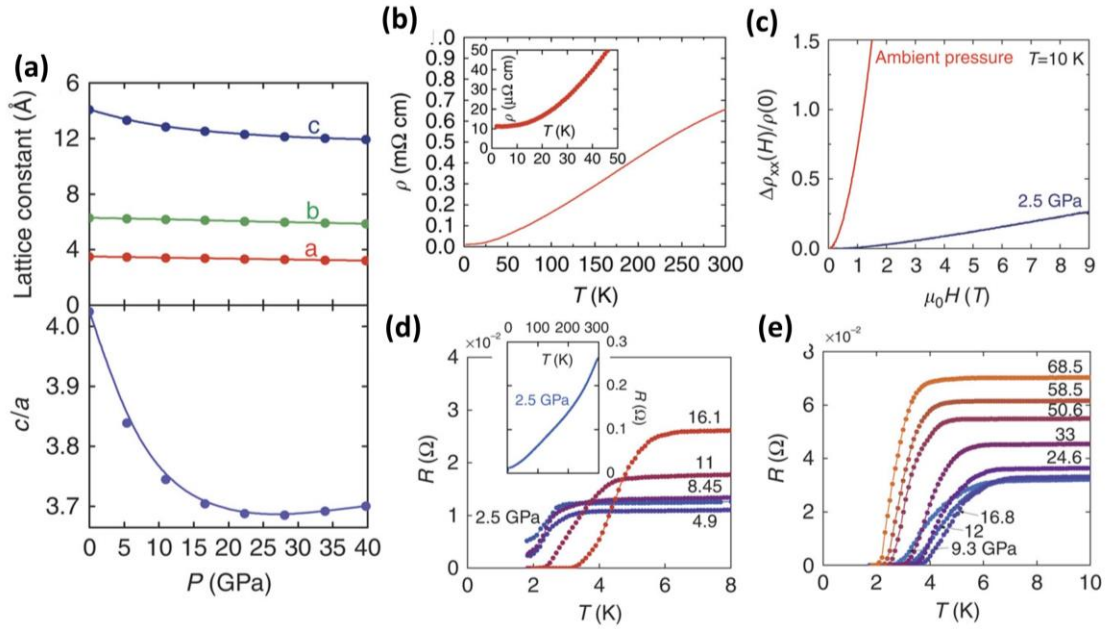


**Figure 4.5.2. Summary of pressure-induced superconductivity of Td-WTe<sub>2</sub>.** By applying a high pressure from 2.5GPa which causes lattice distortion and fermi level change, WTe<sub>2</sub> reached critical temperature around 2-3K at 2-4GPa, and increase to  $T_c$  of 7K at 16.8GPa.

## Chapter 5.

### Tungsten Ditelluride Thin Film Deposition

#### 5.1 WTe<sub>2</sub> Thin Film Materials

One of the crucial steps toward device application and electronics is to develop controlled production of large-area and high-quality WTe<sub>2</sub> thin film materials. Chemical vapor deposition (CVD) is a versatile and industry compatible technique which has been the research focus to bring atomically thin TMDs ready to use. However, tungsten tellurides has yet been studied via CVD methods. Within this work, a variety of CVD processes have been explored to approach atomically thin WTe<sub>2</sub> synthesis.

#### 5.2 Tellurization via Chemical Vapor Deposition Method

Transitional metal oxides have successfully been used for many monolayer TMD materials synthesis via CVD methods. Mo and W sources react with pure sulfur or selenium vapor for MoS<sub>2</sub>,<sup>71,108</sup> WS<sub>2</sub>,<sup>109</sup> and WSe<sub>2</sub><sup>110</sup> monolayer growth. These synthesis routes involves thermally evaporated chalcogen vapor are defined as sulfurization or selenization. Since we are targeting to thermally evaporate tellurium powder/shots for tellurium gas, we called these reactions “Tellurization.”

There are a variety of tungsten precursors could be used for TMD growth. WO<sub>3</sub> and W(CO)<sub>6</sub> were often chosen due to their easy access, low sublimation temperature and success for WSe<sub>2</sub><sup>110</sup> and WS<sub>2</sub><sup>109</sup> monolayer growth. Typical experimental setting is subliming the tungsten and chalcogen precursors at upstream, flow in with carrier gases and react at the hot-zone, then deposited on substrates at downstream. On the other hand,

WO<sub>3</sub> could also be prepared by thermal evaporation prior to the tellurization process, and the crystal structure could be controlled by the annealing temperature,<sup>111</sup> which gave us more options of controlling the tungsten precursor.

Since the sublimation temperature of tellurium is around 450°C, the upstream section of the hot-wall CVD furnace was used instead of pre-heated by a heat tape that was higher than sulfur and selenium sublimation. The partial pressure of tellurium vapor was calculated from the equation derived and tested by L. S. Brooks<sup>112</sup>:

$$\log P = \frac{-5960.2 \pm 14.5}{T} + 7.5999 \pm 0.0136 \quad \text{Equation 5.1}$$

where P is the partial pressure of tellurium in Torr, and T is the designed temperature in K. Hydrogen (H<sub>2</sub>) and argon (Ar) gas was used as carrier gas throughout the CVD growth processes.

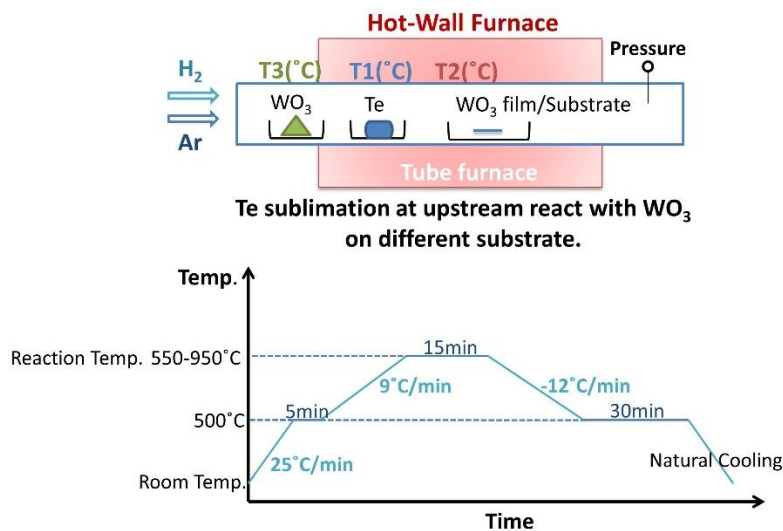


**Figure 5.2.1.** Experiments design and CVD furnace setting for WTe<sub>2</sub> synthesis by tellurization processes. The reaction took place at the hot-zone (T<sub>2</sub>), which is at the center of the furnace. Reaction temperature T<sub>2</sub> at hot-zone, carrier gases H<sub>2</sub>:Ar ratio and growth time are the designed variables for WTe<sub>2</sub> growth. WO<sub>3</sub> was chosen tungsten precursor for this particular schematic plot due to it can be either sublimed at upstream or pre-deposited on substrates for tellurization processes.



### 5.2.1 Control Factors for Tellurization

Figure 5.2.1 has shown the experiment factors for tellurization processes. The control variables for tellurization processes we would discuss includes:

- A. Reaction temperature, pressure and growth time
- B. Carrier gas and their ratio
- C. W and Te atomic ratio
- D. Powder tellurization vs. Thin film tellurization

will be discussed for its suitability of thin film  $\text{WTe}_2$  growth.

#### A. Reaction temperature and growth time

Reaction temperature ( $T_2$  in Figure 5.2.1) and pressure and pressure is one the of most control factor for CVD growth. Te sublimation temperature ( $T_1$  in Figure 5.2.1) was first decided from  $100^\circ\text{C}$  above the melting point of tellurium (M.P.=  $450^\circ\text{C}$ ) which is from  $550^\circ\text{C}$  to  $950^\circ\text{C}$ . Tellurium vapor pressure is 1.4 Torr to 15.28 Torr calculated from Equation 5.1 for from  $550^\circ\text{C}$  to  $950^\circ\text{C}$ . The variation of tellurium sublimation temperature was done by using different section in the same hot-wall tubular furnace. It was understood that there was no reaction nor Te deposition at low sublimation temperature possibly due to low vapor pressure. Thus the reaction temperature ( $T_2$ ) and Te sublimation temperature ( $T_1$ ) were controlled at the same temperature ( $T_1=T_2$ ) in the later experiments.

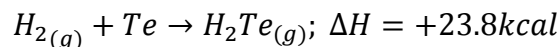
Reaction pressure means the overall designed pressure in the tubular furnace. We have tested the growth pressure down to our lower limit 0.1Torr to near-atmosphere 650Torr, and found 5-10 Torr gave better indication of tellurization with particulates deposition. For

many reports for  $\text{WS}_2$  and  $\text{WSe}_2$  CVD growth, near atmosphere condition gave better quality and large monolayer domains. From our observation, although larger overall pressure in the reaction chamber could extend the time for tellurium gas (or  $\text{H}_2\text{Te}$ ) stayed in the reaction zone; nonetheless, the carrier gas Ar and  $\text{H}_2$  filled in the reaction chamber also reduced the concentration of tellurium gases molecules, which reduced the chance for tellurization.

Growth time here means the time length the furnace stayed the reaction temperature. In our experiments, growth time varies from 15min to 4 hours with different reaction temperature excluding the ramping time. From the reports of  $\text{MoTe}_2$  CVD growth<sup>74,113</sup>, it is believed that a high ramp rate is helpful for keeping the telluride thin film materials on the substrate and prevent decomposition or phase transition in a heated environment.<sup>113</sup> Due to the low ramp rate at  $9^\circ\text{C}/\text{min}$  (for reaching temperature above  $500^\circ\text{C}$ ) of the furnace we used for tellurization, the overall growth time was affected by the low-period of ramping time. Our growth time for tellurization processes was narrowed down to 15mins for reaction temperature at  $850^\circ\text{C}$ .

#### B. Carrier gas and their ratio

Hydrogen gas ( $\text{H}_2$ ) and argon (Ar) were the carrier gases throughout  $\text{WTe}_2$  CVD processes and reports from  $\text{MoTe}_2$  synthesis.<sup>74,113</sup>  $\text{H}_2$  is usually used for cleaning, baking and carrying out the by-products from the CVD reaction. Although the mechanism of using  $\text{H}_2$  in CVD-grown transitional metal tellurides (especially  $\text{MoTe}_2$ ) are not yet be solved, it was believed that hydrogen telluride ( $\text{H}_2\text{Te}$ ) formation may be beneficial for tellurization processes.  $\text{H}_2\text{Te}$  is an unstable gas formed from an endothermic reaction<sup>114</sup>:



It was known flowing hydrogen with heated Te element could yield  $H_2Te$  with poor quality.<sup>115</sup> However, the instability of  $H_2Te$  could be useful for  $WTe_2$  formation above the  $H_2Te$  formation temperature 200°C.

#### C. W and Te atomic ratio

In our experimental setting, tungsten and tellurium atomic ratio was controlled by the molar ratio between the tungsten precursor and tellurium shots. For  $WO_3$  powder tellurization the W:Te ratio is the  $WO_3$ :Te molar ratio. For pre-deposited  $WO_3$  thin film tellurization, due to the  $WO_3$  deposited on the substrate may vary in each batch, these tellurization runs were assumed to have excess Te.

#### D. Powder tellurization vs. Thin film tellurization

In our experiment,  $WO_3$  was chosen as the first precursor for  $WTe_2$  CVD growth. Though  $WO_3$  has been very successful for  $WS_2/WSe_2$  monolayers through powder chalcogenization, our first trials indicated that this does not work for tellurization. Instead, of using  $WO_3$  powder, the majority of our experiments change to  $WO_3$  thin film tellurization. This technique was also used in  $MoO_3$  thin film tellurization and successfully carried out  $MoTe_2$  monolayer growth.<sup>74</sup> Tungsten thin films on Silicon substrates prepared by sputtering were also prepared for thin film tellurization.

### 5.3 Thin Film WO<sub>3</sub> Tellurization

The pre-deposited WO<sub>3</sub> on various substrates (Sapphire and Silicon substrates) were prepared by Kurt J. Lesker Lab-18 Evaporator with controlled thickness 10nm-50nm. The as-deposited WO<sub>3</sub> thin films were determined amorphous. WO<sub>3</sub> films can further annealed at 600°C for 30secs by Allwin21 Rapid Thermal Annealing (RTA) to obtain meta-stable hexagonal WO<sub>3</sub> phase.<sup>111,116</sup>

The optimal tellurization processes has been narrowed down to 850°C, 5Torr for 15min with 10sccm of H<sub>2</sub> and 50sccm of Ar after initial trials.

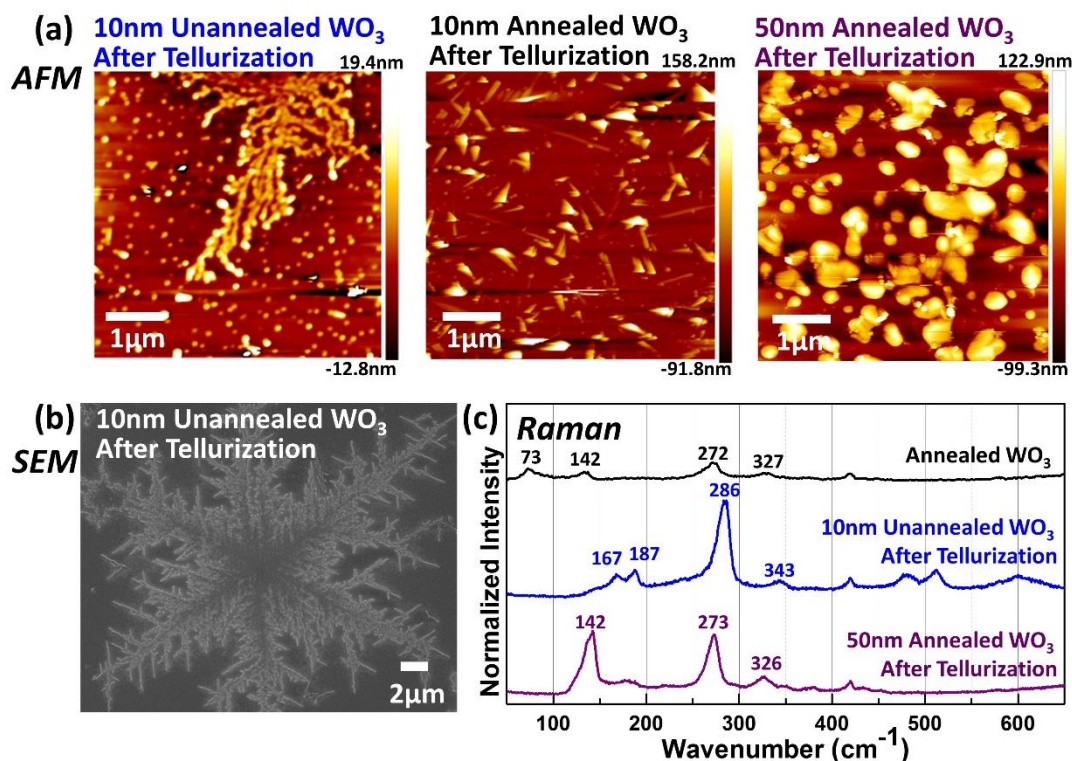


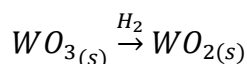
**Figure 5.3.1.** The (a) AFM images for 10nm amorphous and 10nm and 50nm annealed WO<sub>3</sub> after tellurization, The rods formed lateral aggregates in dendrite structure for 10nm amorphous sample, while only small rods spreading on annealed sample. 50nm annealed WO<sub>3</sub> after tellurization seemed to form larger crystalline without dendrite

**structure. (b) SEM images shows the full picture of the dendrite structure formed on 10nm amorphous WO<sub>3</sub> after tellurization. (c) Raman spectra comparison between the amorphous WO<sub>3</sub> and annealed WO<sub>3</sub> thin film after tellurization showed they have different crystalline aggregates after tellurization.**

Figure 5.3.1. showed the comparison of the results annealed and unannealed (amorphous) WO<sub>3</sub> thin films after tellurization. We have observed the large crystalline aggregates were formed on 10nm amorphous WO<sub>3</sub> after tellurization process. The crystals looked rectangular, rod-like crystalline aggregated laterally on the surface. The aggregates are big enough for collecting Raman spectrum and the signature at 147, 167 and 285 cm<sup>-1</sup> was observed. For 10nm annealed WO<sub>3</sub> samples, although there were rod-like crystals on the surface, they were not big enough for Raman spot size. Thus, 50nm annealed WO<sub>3</sub> samples were prepared and undergo a longer tellurization process that resulted in larger grain size on the substrate. From the Raman spectra we were able to determine that the amorphous WO<sub>3</sub> thin film was able to migrate on the surface and form crystal aggregates; while the annealed WO<sub>3</sub> underwent the deformation and recrystallization of WO<sub>3</sub>, resulted in enhanced peaks at 142, 272 and 326 cm<sup>-1</sup>.

We have compared the Raman spectrum from amorphous WO<sub>3</sub> thin film tellurization to bulk WTe<sub>2</sub> Raman and found no match. We have compared with the literature and found the Raman spectrum of 10nm amorphous WO<sub>3</sub> after tellurization very close to WO<sub>2</sub> (Figure 5.2.3) with a ~2cm<sup>-1</sup> shift. Although there was no the signature at lower wavenumber at 147 and 167cm<sup>-1</sup> on the literature, the peaks at 286, 342, 511cm<sup>-1</sup> did match the WO<sub>2</sub> Raman spectra. XPS was further used for verify the elemental composition of tellurized

10nm amorphous  $WO_3$  sample, and found no tellurium had deposited in any way (either pure tellurium or its compound) on the substrate. The result suggested that thermal reduction of  $WO_3$  was dominant reaction in the heated hydrogen environment: <sup>117</sup>



but no evidence of tellurization happened. The XRD results (Figure 5.3.3) also confirmed that monoclinic  $WO_2$  on the surface. The  $WO_2$  micro-rods migrated laterally and form snowflake-like aggregated structure on the substrates.

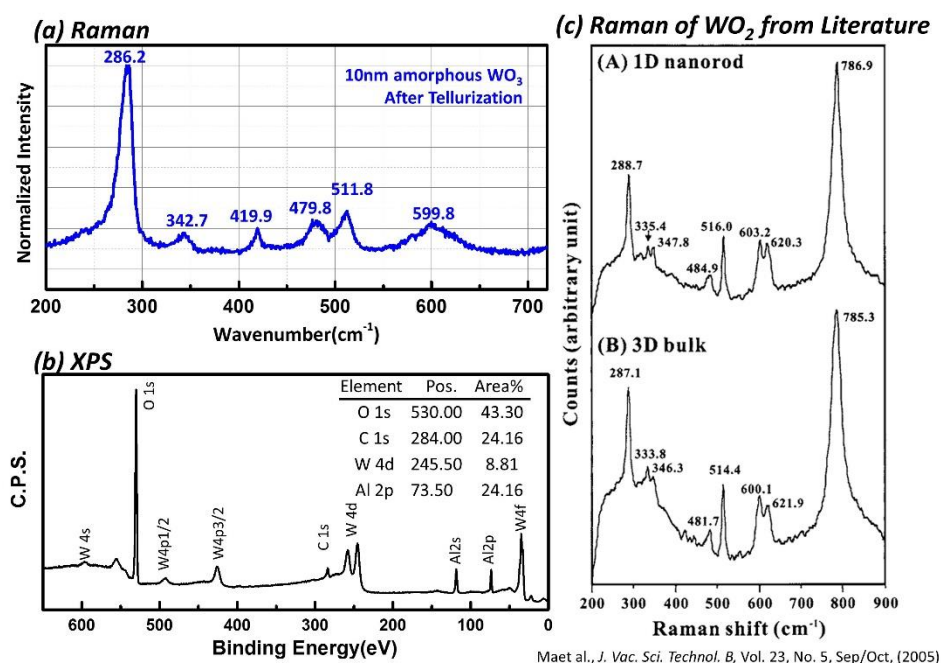


**Figure 5.3.2.** The (a) Raman Spectrum for the tellurized 10nm amorphous  $WO_3$  with the comparable range with (c)  $WO_2$  Raman in the literature. The peaks at 286.2, 342.7, 511.8 and 599.8 cm<sup>-1</sup> for our  $WO_3$  after tellurization were corresponding to the 288.7, 347.8, 516.9, and 603.2cm<sup>-1</sup> for  $WO_2$  nanocrystalline.<sup>117</sup> (b) XPS confirmed that there was no Te exist on the surface in any way, which indicated that no tellurization but thermal reduction happened for  $WO_3$  thin film.

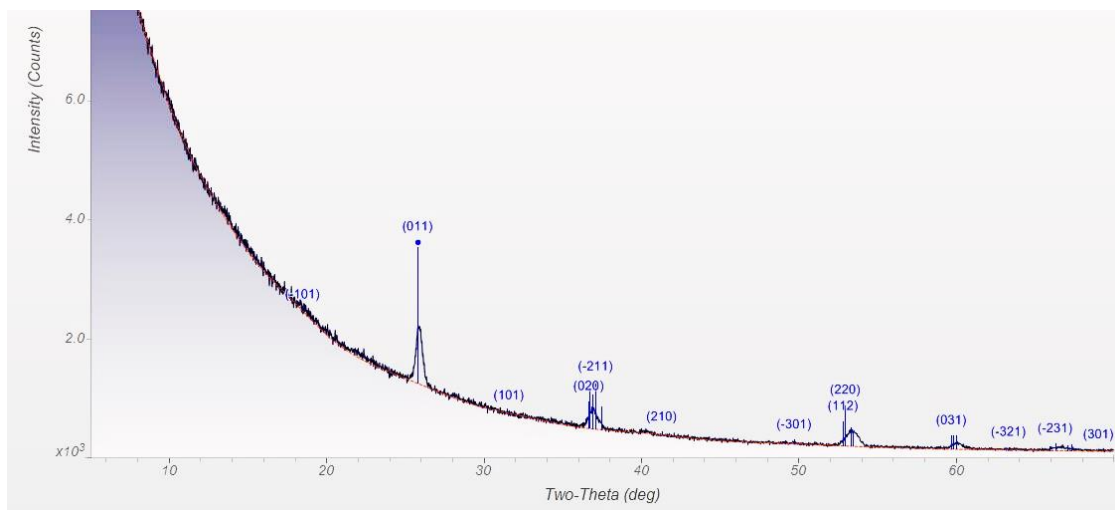


**Figure 5.3.3. The XRD patterns of 10nm  $WO_3$  after tellurization and overlay with the lattice planes of  $WO_2$  crystal in the ICDD database.**

Many trials including (1) changing carrier gas, (2) close boat, (3) static CVD system with extended growth time, (4)  $WO_2$  tellurization have been done to test the ability of  $WO_3$  as precursor for  $WTe_2$  growth. Nonetheless, there is no indication of tellurization for these trials. Thermal reduction of  $WO_3$  is still the favorable reaction for  $WO_2$ , and  $WO_2$  is relatively stable up till  $1530^\circ\text{C}$  according to W-O binary phase diagram. There was no sign of O-to-Te ion exchange reaction for  $WO_2$  even at the  $1100^\circ\text{C}$  limit of the furnace. Change of tungsten source was the key to move forward for  $WTe_2$  growth.

On the other hand, in order to be able to recognize possible Te deposition after tellurization process, we have investigated the Raman signature for pure Te. Surprisingly we found 5 $\mu\text{m}$  of tellurium oxides ( $TeO_2$ ) on the surface of tellurium shots. In order to prevent more oxygen involve with tellurization, we developed a process of etching by using 50vol% nitric acid ( $HNO_3$ ) for 5mins and followed by 25vol% hydrochloride acid ( $HCl$ ) for 1min to remove the tellurium oxide layer on the Te shots for the further studies. This

etching process needs to be done right before the tellurization because the oxidation of Te would happen really fast after etching. Figure 5.3.4 show the oxidation of Te after etching.

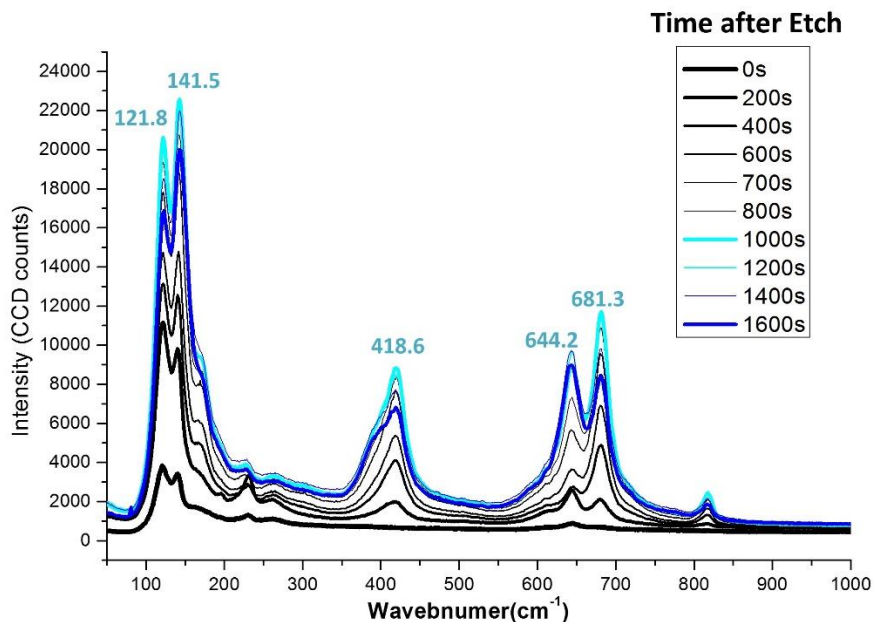


**Figure 5.3.4.** The Raman spectra of oxidation on Te surface after etching process. Te oxidation happened right after wet etch process and form a layer of TeO<sub>2</sub> on the surface. Raman signature indicates that the TeO<sub>2</sub> layer was  $\alpha$ -TeO<sub>2</sub>.

#### 5.4 Vapor Phase Tellurization

Tungsten hexacarbonyl ( $\text{W}(\text{CO})_6$ ) was selected due to it is also a precursor in powder form, and its low sublimation temperature (M.P.=120°C, B.P.=170°C). It also has been reported used for TMD monolayer growth. Tellurization of  $\text{W}(\text{CO})_6$  was carried out by  $\text{W}(\text{CO})_6$  powder evaporation at upstream of the furnace, and Te at the hot-zone, and substrates at downstream (Figure 5.4.1).



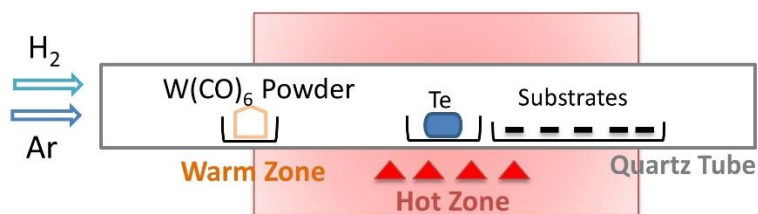


**Figure 5.4.1. Schematic plot for  $W(CO)_6$  powder tellurization processes.**

The control variables for vapor phase tellurization were similar to the  $WO_3$  thin film tellurization. The difference is that the tungsten precursor was vaporized and react with tellurium vapor at hot-zone. The test runs at  $850^\circ\text{C}$  for 30min growth showed there were small crystal-like particulates on the surface. OM images in Figure 5.4.2 has showed the particulates were spreading out all over the substrate, and FESEM images showed the nucleation cites in the crystals. Raman spectra told us that the particulates are crystals with strong vibration intensities. The peak position at  $161.5$  and  $210.5\text{ cm}^{-1}$  were not  $TeO_2$ , crystalline Te or  $WO_2$  from Raman analysis. We were not able to tell specifically if this was  $WTe_2$  crystals due to lack of standard bulk  $WTe_2$  sampels.

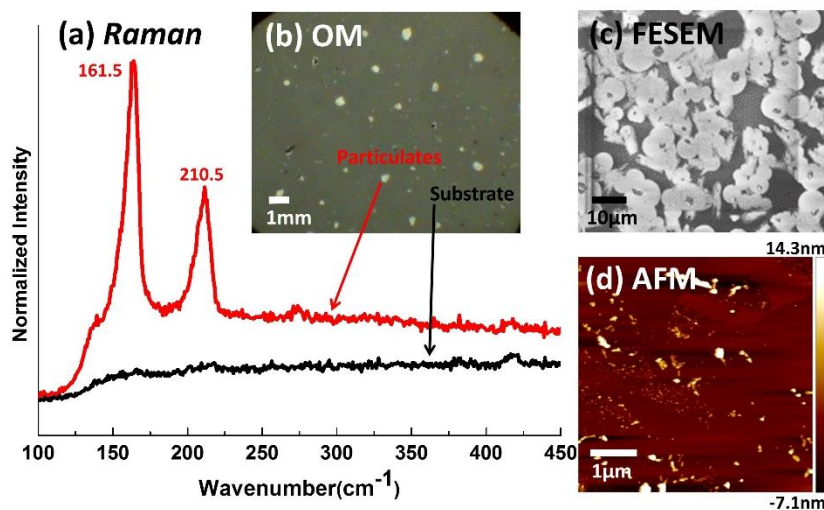


**Figure 5.4.2. (a) Raman; (b) OM; (c) FESEM; (d) AFM characterization for vapor phase tellurization of  $\text{W}(\text{CO})_6$ . The particulates were crystalized on sapphire substrates at  $750^\circ\text{C}$  with 30min tellurization time.**

Further analysis was not done after the bulk  $\text{WTe}_2$  crystals were synthesized. Figure 5.4.3 showed the comparison between the crystal grown by  $\text{W}(\text{CO})_6$  vapor phase tellurization stimulated by 488nm incident laser, and bulk  $\text{WTe}_2$  characterized by 488nm and 647nm incident laser. The early characterization was done at WiTEC Raman System with 488nm incident laser and 600 grating. The first Raman spectrum was also obtained by WiTEC system with 488nm incident laser and same grating settings. From 5.4.3, we are able to tell right now that the  $\text{W}(\text{CO})_6$  tellurization was successful. The small particulates on the substrates are now proven to be small  $\text{WTe}_2$  crystals.

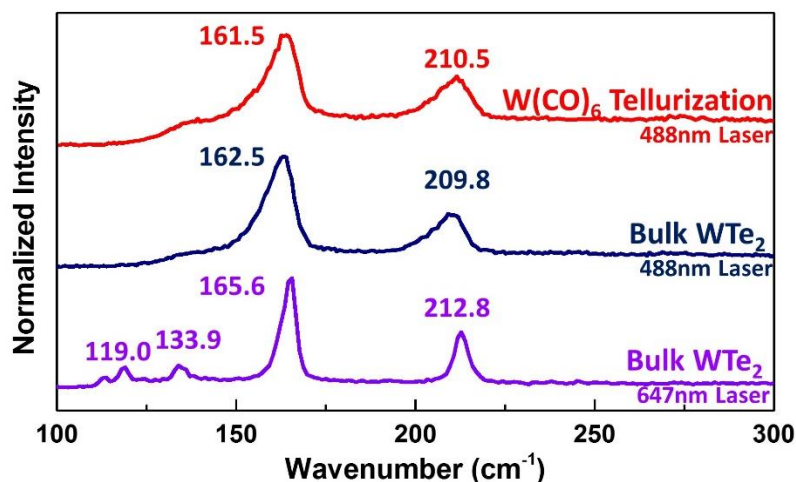


**Figure 5.4.3. Raman Spectra comparing the Raman from small crystals in Figure 5.4.2 from W(CO)<sub>6</sub> tellurization, and two spectra from bulk WTe<sub>2</sub> obtained by CVT. There are two bulk WTe<sub>2</sub> Raman spectra for the difference of incident laser would reveal more vibration modes with a lower excitation energy. The unknown peaks at 161 and 211 cm<sup>-1</sup> from W(CO)<sub>6</sub> tellurization are now identified as the combination of B<sub>2</sub> and A<sub>1</sub> modes at 165cm<sup>-1</sup>, and B<sub>1</sub> mode at near 212 cm<sup>-1</sup> for bulk-WTe<sub>2</sub>. (Details about vibration modes of bulk-WTe<sub>2</sub> in Figure 3.3.1.)**

Instead of using W(CO)<sub>6</sub> powder for tellurization, W(CO)<sub>6</sub> is also used as metal-organic precursor in MOCVD processes. With the MOCVD setting, the usage, partial vapor pressure, flow-in timing of W(CO)<sub>6</sub> precursor can be accurately controlled in during synthesis. Figure 5.3.4. demonstrates the schematic plot for the HPCVD system for W(CO)<sub>6</sub> vapor phase tellurization. Different entering time for W(CO)<sub>6</sub> were tested for the purpose testing a tellurium-rich environment would be useful for WTe<sub>2</sub> formation or not. But no deposition was observed on the substrates regarding to the variation of W(CO)<sub>6</sub> entering time. Pure hydrogen carrier gas and hydrogen and nitrogen gas mixture were

tested with excess tellurium on the susceptor. Results suggested that pure hydrogen environment will carry out all the components that could be sublimed in the system including Te gas and decomposed tungsten precursors fragments. Reaction carried out with mixture of  $N_2$  and  $H_2$  was similar to  $W(CO)_6$  tellurization with particulates on substrates. However, the surface characterization was not completed due to size is too small for Raman and XRD measurements. The introduction of diethyl-telluride precursor later provided a more reactive factor for tellurium instead of tellurization with small amount of hydrogen gas.

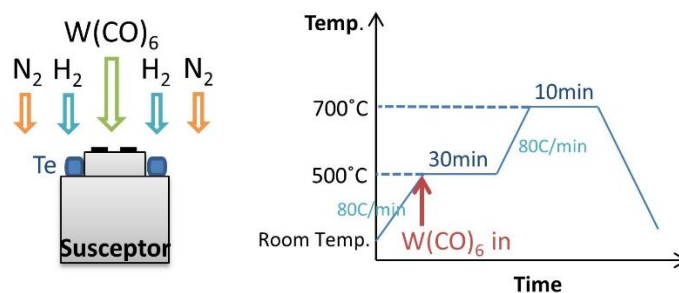


**Figure 5.4.4. MOCVD schematic plot, and the temperature profile for tellurization with controlled  $W(CO)_6$ . The carrier gas for  $W(CO)_6$  is always  $H_2$  gas. The addition of  $N_2$  gas was useful to carry out some crystal-like particulate deposited on the substrate (not shown here).**

## Chapter 6.

### Conclusion and Future Work

In this thesis, we presented a combined experimental and theoretical study of tungsten ditelluride ( $\text{WTe}_2$ ).

$\text{WTe}_2$  was synthesized by two major techniques: chemical vapor transport (CVT) for bulk  $\text{WTe}_2$ , and chemical vapor deposition (CVD) for thin film  $\text{WTe}_2$ . Bulk  $\text{WTe}_2$  synthesized via CVT method crystallized at near-thermal equilibrium condition, and was physically exfoliated for properties investigation. In Chapter 3, we confirmed that  $\text{WTe}_2$  is a TMD crystalized in distorted 1T structure (Td) for it is thermodynamically favorable relative to the 2H polymorph. In Section 3.1 and 3.2, we provided detailed verification process using x-ray diffraction (XRD) and x-ray photoelectron spectroscopy (XPS) to confirm the bulk crystal product. Raman signature of Td- $\text{WTe}_2$  was first obtained for future references in Section 3.3, where our DFT calculation in Section 4.4 offered detailed information about the vibration modes of  $\text{WTe}_2$ , and proved that the out-of-plane vibrational modes involve atomic motions at angles that are displaced from the c-axis direction because the distorted octahedral bonding in Td- $\text{WTe}_2$ . AFM, SEM images in Section 3.4 offer the morphology and single thickness of  $\text{WTe}_2$  which could be beneficial for exfoliation processes.

Regarding to electrical properties of  $\text{WTe}_2$ , we have experimentally verified that Td- $\text{WTe}_2$  behaves as a metal, and has yet explained strong dependence of the resistivity on the thickness of multilayer flakes in Section 3.5. Our theoretical calculation results in Section

4.3 showed a 0.21 eV indirect band overlap from the  $\Gamma$  to X direction in the band structure of Td-WTe<sub>2</sub>, indicating that Td-WTe<sub>2</sub> is a semimetallic TMD material.

We have also evaluated the stability of thin flakes by XPS and Raman in Section 3.6, and found that care must be taken to ensure that oxidation does not occur, as the surface of Td-WTe<sub>2</sub> is sensitive to ambient air. The phase transition of Td and 2H phase WTe<sub>2</sub> was discussed in Section 4.5 that it is physically impossible to induce transition from Td-WTe<sub>2</sub> to 2H-WTe<sub>2</sub> with pressure.

We also explored synthesis routes for growing WTe<sub>2</sub> thin film materials by CVD. In Section 5.2, we have proved that tellurization of tungsten oxide (WO<sub>3</sub>) vapor would not obtain any deposition at downstream. Tellurization of WO<sub>3</sub> thin films is possible, however, the hydrogen reduction of WO<sub>3</sub> would be dominant reaction and form 2D WO<sub>2</sub>. By changing the tungsten source to metal-organic precursor, W(CO)<sub>6</sub>, we are able to synthesize WTe<sub>2</sub> layers via vapor phase tellurization. Further investigation should be done for exploring the possibility to stabilize thin layered WTe<sub>2</sub> grown by this method.

Despite many exciting results found for WTe<sub>2</sub> in this research, many questions still remain unanswered and require additional work to approach the ultimate goal of monolayer WTe<sub>2</sub> for device application. In addition to the recent boom for studying the properties and the application regarding to magnetoresistance and superconductivity of Td-WTe<sub>2</sub>.<sup>94,118–122</sup> Structural wisely, more efforts need to put on (1) phase transition pathways studies for WTe<sub>2</sub>, (2) lattice strain on WTe<sub>2</sub>, (3) substrate effect for thin layered WTe<sub>2</sub> deposition, (4) chalcogen ion doping, (5) tungsten co-chalcogen TMDs (WSe<sub>x</sub>Te<sub>2-x</sub>, etc) and (6) Transitional metal tellurides (Mo<sub>x</sub>W<sub>1-x</sub>Te<sub>2</sub>, etc.) growth.

Lithiation which was used for exfoliation and to induce phase transition in the in many other TMDs systems.<sup>123–127</sup> This method can could potentially cause a change in electron

counts for the  $d$ -orbitals<sup>124–126</sup> that leads to destabilization of the original crystal structure. This was studied by multiple groups on MoS<sub>2</sub> materials for 2H to 1T structural change, and could potentially induce phase transition of WTe<sub>2</sub> from Td to 1T structure. This can also help open another application for WTe<sub>2</sub> materials on energy storage devices based on its layered structure and conductivity as electrode materials.

## References

1. Novoselov, K. S. *et al.* Electric field effect in atomically thin carbon films. *Science (New York, N.Y.)* **306**, 666–9 (2004).
2. Novoselov, K. S. *et al.* Two-dimensional atomic crystals. *Proceedings of the National Academy of Sciences of the United States of America* **102**, 10451–10453 (2005).
3. Lee, K. H. *et al.* Large-scale synthesis of high-quality hexagonal boron nitride nanosheets for large-area graphene electronics. *Nano letters* **12**, 714–8 (2012).
4. Wang, Q. H., Kalantar-Zadeh, K., Kis, A., Coleman, J. N. & Strano, M. S. Electronics and optoelectronics of two-dimensional transition metal dichalcogenides. *Nature nanotechnology* **7**, 699–712 (2012).
5. Radisavljevic, B., Radenovic, A., Brivio, J., Giacometti, V. & Kis, A. Single-layer MoS<sub>2</sub> transistors. *Nature nanotechnology* **6**, 147–50 (2011).
6. Remskar, M. *et al.* First demonstration of two-dimensional WS<sub>2</sub> transistors exhibiting 10<sup>5</sup> room temperature modulation and ambipolar behavior. in *70th Device Research Conference* 187–188 (IEEE, 2012).  
doi:10.1109/DRC.2012.6257042
7. Lam, K.-T., Cao, X. & Guo, J. Device Performance of Heterojunction Tunneling Field-Effect Transistors Based on Transition Metal Dichalcogenide Monolayer. *IEEE Electron Device Letters* **34**, 1331–1333 (2013).
8. Szabo, A., Koester, S. J. & Luisier, M. Metal-dichalcogenide hetero-TFETs: Are they a viable option for low power electronics? in *72nd Device Research*



*Conference* 19–20 (IEEE, 2014). doi:10.1109/DRC.2014.6872279

9. Ilatikhameneh, H. *et al.* Tunnel Field-Effect Transistors in 2D Transition Metal Dichalcogenide Materials. 7 (2015). at <<http://arxiv.org/abs/1502.01760>>
10. Kang, J., Tongay, S., Zhou, J., Li, J. & Wu, J. Band offsets and heterostructures of two-dimensional semiconductors. *Applied Physics Letters* **102**, 012111 (2013).
11. Gong, C. *et al.* Band alignment of two-dimensional transition metal dichalcogenides: Application in tunnel field effect transistors. *Applied Physics Letters* **103**, 053513 (2013).
12. Li, M. (Oscar), Esseni, D., Snider, G., Jena, D. & Grace Xing, H. Single particle transport in two-dimensional heterojunction interlayer tunneling field effect transistor. *Journal of Applied Physics* **115**, 074508 (2014).
13. Yin, Z. *et al.* Single-layer MoS<sub>2</sub> phototransistors. *ACS nano* **6**, 74–80 (2012).
14. Perea-López, N. *et al.* Photosensor Device Based on Few-Layered WS<sub>2</sub> Films. *Advanced Functional Materials* **23**, 5511–5517 (2013).
15. Perkins, F. K. *et al.* Chemical vapor sensing with monolayer MoS<sub>2</sub>. *Nano letters* **13**, 668–73 (2013).
16. Lu, Y., Goldsmith, B. R., Kybert, N. J. & Johnson, A. T. C. DNA-decorated graphene chemical sensors. *Applied Physics Letters* **97**, 083107 (2010).
17. Wang, L. *et al.* Functionalized MoS<sub>2</sub> nanosheet-based field-effect biosensor for label-free sensitive detection of cancer marker proteins in solution. *Small (Weinheim an der Bergstrasse, Germany)* **10**, 1101–5 (2014).

18. Pumera, M. & Loo, A. H. Layered transition-metal dichalcogenides (MoS<sub>2</sub> and WS<sub>2</sub>) for sensing and biosensing. *TrAC Trends in Analytical Chemistry* **61**, 49–53 (2014).
19. Lee, J., Wang, Z., He, K., Shan, J. & Feng, P. X.-L. High frequency MoS<sub>2</sub> nanomechanical resonators. *ACS nano* **7**, 6086–91 (2013).
20. Kaul, A. B. Nano-electro-mechanical-systems (NEMS) and energy-efficient electronics and the emergence of two-dimensional layered materials beyond graphene. in *Proc. SPIE 8725, Micro- and Nanotechnology Sensors, Systems, and Applications V* (eds. George, T., Islam, M. S. & Dutta, A. K.) 872502 (International Society for Optics and Photonics, 2013). doi:10.1117/12.2016432
21. Chhowalla, M. *et al.* The chemistry of two-dimensional layered transition metal dichalcogenide nanosheets. *Nature chemistry* **5**, 263–75 (2013).
22. Kumar, A. & Ahluwalia, P. K. Electronic transport and dielectric properties of low-dimensional structures of layered transition metal dichalcogenides. *Journal of Alloys and Compounds* **587**, 459–467 (2014).
23. Srivastava, S. & Avasthi, B. Layer type tungsten dichalcogenide compounds: their preparation, structure, properties and uses. *Journal of materials science* **20**, 3801–3815 (1985).
24. Butler, S. Z. *et al.* Opportunities in Two-Dimensional Materials Beyond Graphene. *ACS Nano* **7**, 2898–2926 (2013).
25. Ding, Y. *et al.* First principles study of structural, vibrational and electronic properties of graphene-like MX<sub>2</sub> (M=Mo, Nb, W, Ta; X=S, Se, Te) monolayers. *Physica B: Condensed Matter* **406**, 2254–2260 (2011).

26. Hsu, A. *et al.* Large-Area 2-D Electronics: Materials, Technology, and Devices. *Proceedings of the IEEE* **101**, 1638–1652 (2013).
27. Jena, D. Tunneling Transistors Based on Graphene and 2-D Crystals. *Proceedings of the IEEE* **101**, 1585–1602 (2013).
28. Jena, D. Tunneling Transistors Based on Graphene and 2-D Crystals. *Proceedings of the IEEE* **101**, 1585–1602 (2013).
29. Jariwala, D., Sangwan, V. K., Lauhon, L. J., Marks, T. J. & Hersam, M. C. Emerging device applications for semiconducting two-dimensional transition metal dichalcogenides. *ACS nano* **8**, 1102–20 (2014).
30. Ghosh, R. K. & Mahapatra, S. Monolayer Transition Metal Dichalcogenide Channel-Based Tunnel Transistor. *IEEE Journal of the Electron Devices Society* **1**, 175–180 (2013).
31. Fiori, G. *et al.* Electronics based on two-dimensional materials. *Nature Nanotechnology* **9**, 768–779 (2014).
32. Kośmider, K. & Fernández-Rossier, J. Electronic properties of the MoS<sub>2</sub>-WS<sub>2</sub> heterojunction. *Physical Review B* **87**, 075451 (2013).
33. Terrones, H., López-Urías, F. & Terrones, M. Novel hetero-layered materials with tunable direct band gaps by sandwiching different metal disulfides and diselenides. *Scientific reports* **3**, 1549 (2013).
34. Kumar, A. & Ahluwalia, P. K. Electronic structure of transition metal dichalcogenides monolayers 1H-MX<sub>2</sub> (M = Mo, W; X = S, Se, Te) from ab-initio

theory: new direct band gap semiconductors. *The European Physical Journal B* **85**, 186 (2012).

35. Kumar, A. & Ahluwalia, P. K. Semiconductor to metal transition in bilayer transition metals dichalcogenides MX<sub>2</sub> ( M = Mo, W; X = S, Se, Te). *Modelling and Simulation in Materials Science and Engineering* **21**, 065015 (2013).
36. Ye, M., Winslow, D., Zhang, D., Pandey, R. & Yap, Y. Recent Advancement on the Optical Properties of Two-Dimensional Molybdenum Disulfide (MoS<sub>2</sub>) Thin Films. *Photonics* **2**, 288–307 (2015).
37. Heine, T. Transition metal chalcogenides: ultrathin inorganic materials with tunable electronic properties. *Accounts of chemical research* **48**, 65–72 (2015).
38. Splendiani, A. *et al.* Emerging photoluminescence in monolayer MoS<sub>2</sub>. *Nano letters* **10**, 1271–5 (2010).
39. Xiao, D., Liu, G.-B., Feng, W., Xu, X. & Yao, W. Coupled Spin and Valley Physics in Monolayers of MoS<sub>2</sub> and Other Group-VI Dichalcogenides. *Physical Review Letters* **108**, 196802 (2012).
40. Kuc, A., Zibouche, N. & Heine, T. Influence of quantum confinement on the electronic structure of the transition metal sulfide TS<sub>2</sub>. *Physical Review B* **83**, 245213 (2011).
41. Wilson, J., Salvo, F. Di & Mahajan, S. Charge-density waves and superlattices in the metallic layered transition metal dichalcogenides. *Advances in Physics* **24**, 37–41 (1975).
42. Revolinsky, E. & Beerntsen, D. Electrical Properties of the MoTe<sub>2</sub>–WTe<sub>2</sub> and MoSe<sub>2</sub>–WSe<sub>2</sub> Systems. *Journal of Applied Physics* **35**, 2086 (1964).

43. Yun, W. S., Han, S. W., Hong, S. C., Kim, I. G. & Lee, J. D. Thickness and strain effects on electronic structures of transition metal dichalcogenides: 2H-MX<sub>2</sub> semiconductors (M = Mo, W; X = S, Se, Te). *Physical Review B* **85**, 033305 (2012).
44. Perfetti, L. *et al.* Spectroscopic signatures of a bandwidth-controlled Mott transition at the surface of 1T-TaSe<sub>2</sub>. *Physical review letters* **90**, 166401 (2003).
45. Liu, Y. *et al.* Superconductivity induced by Se-doping in layered charge-density-wave system 1T-TaS<sub>2</sub>-xSex. *Applied Physics Letters* **102**, 192602 (2013).
46. Ubaldini, A., Jacimovic, J., Ubrig, N. & Giannini, E. Chloride-Driven Chemical Vapor Transport Method for Crystal Growth of Transition Metal Dichalcogenides. *Crystal Growth & Design* **13**, 4453–4459 (2013).
47. Fourcaudot, G., Gourmala, M. & Mercier, J. Vapor phase transport and crystal growth of molybdenum trioxide and molybdenum ditelluride. *Journal of Crystal Growth* **46**, 132–135 (1979).
48. Lezama, I. G. *et al.* Surface transport and band gap structure of exfoliated 2H-MoTe<sub>2</sub> crystals. *2D Materials* **1**, 021002 (2014).
49. Lee, H. N. S. The Low-Temperature Transport Properties of NbSe<sub>2</sub>. *Journal of Applied Physics* **40**, 602 (1969).
50. Al-Hilli, A. a. & Evans, B. L. The preparation and properties of transition metal dichalcogenide single crystals. *Journal of Crystal Growth* **15**, 93–101 (1972).
51. Binnewies, M., Glaum, R., Schmidt, M. & Schmidt, P. Chemical Vapor Transport

Reactions - A Historical Review. *Zeitschrift für anorganische und allgemeine Chemie* **639**, 219–229 (2013).

52. Mercier, J. Recent developments in chemical vapor transport in closed tubes. *Journal of Crystal Growth* **56**, 235–244 (1982).
53. *Binary Alloy Phase Diagrams, 2nd Edition*. (ASM International, 1990). at [http://www.asminternational.org/web/san-diego-chapter/search/-/journal\\_content/56/10192/57718G/PUBLICATION](http://www.asminternational.org/web/san-diego-chapter/search/-/journal_content/56/10192/57718G/PUBLICATION)>
54. Knop, O. & Haraldsen, H. A NOTE ON THE SYSTEM WOLFRAM-TELLURIUM. *Canadian Journal of Chemistry* 1142–1145 (1956). at <http://www.nrcresearchpress.com/doi/pdf/10.1139/v56-149>>
55. Mar, A., Jobic, S. & Ibers, J. A. Metal-metal vs tellurium-tellurium bonding in WTe<sub>2</sub> and its ternary variants TaIrTe<sub>4</sub> and NbIrTe<sub>4</sub>. *Journal of the American Chemical Society* **114**, 8963–8971 (1992).
56. Pan, X.-C. *et al.* Pressure-driven dome-shaped superconductivity and electronic structural evolution in tungsten ditelluride. *Nature communications* **6**, 7805 (2015).
57. Brown, B. E. The crystal structures of WTe<sub>2</sub> and high-temperature MoTe<sub>2</sub>. *Acta Crystallographica* **20**, 268–274 (1966).
58. Kabashima, S. Electrical Properties of Tungsten-Ditelluride WTe<sub>2</sub>. *Journal of the Physical Society of Japan* **21**, 945–948 (1966).
59. Callanan, J. E., Hope, G. A., Weir, R. D. & Jr., E. F. W. Thermodynamic properties of tungsten ditelluride (WTe<sub>2</sub>) I. The preparation and lowtemperature heat capacity at temperatures from 6K to 326K. *The Journal of Chemical Thermodynamics* **24**, 627–638 (1992).

60. Weir, R. D. Thermophysics of advanced engineering materials. *Pure and Applied Chemistry* **71**, 1215–1226 (1999).
61. Donley, M. S., Murray, P. T. & McDevitt, N. T. Synthesis and Characterization of MoS<sub>2</sub> Thin Films Grown by Pulsed Laser Evaporation. *MRS Proceedings* **140**, 277 (2011).
62. Skrabalak, S. E. & Suslick, K. S. Porous MoS<sub>2</sub> synthesized by ultrasonic spray pyrolysis. *Journal of the American Chemical Society* **127**, 9990–1 (2005).
63. Regula, M., Ballif, C., Moser, J. H. & Lévy, F. Structural, chemical, and electrical characterisation of reactively sputtered WS<sub>x</sub> thin films. *Thin Solid Films* **280**, 67–75 (1996).
64. Liu, K.-K. *et al.* Growth of large-area and highly crystalline MoS<sub>2</sub> thin layers on insulating substrates. *Nano letters* **12**, 1538–44 (2012).
65. Tan, L. K. *et al.* Atomic layer deposition of a MoS<sub>2</sub> film. *Nanoscale* **6**, 10584–8 (2014).
66. Kong, D. *et al.* Synthesis of MoS<sub>2</sub> and MoSe<sub>2</sub> Films with Vertically Aligned Layers. *Nano Letters* **13**, 1341–1347 (2013).
67. Zhan, Y., Liu, Z., Najmaei, S., Ajayan, P. M. & Lou, J. Large-area vapor-phase growth and characterization of MoS<sub>2</sub> atomic layers on a SiO<sub>2</sub> substrate. *Small (Weinheim an der Bergstrasse, Germany)* **8**, 966–71 (2012).
68. Shanmugam, M., Bansal, T., Durcan, C. A. & Yu, B. Schottky-barrier solar cell based on layered semiconductor tungsten disulfide nanofilm. *Applied Physics*

*Letters* **101**, 263902 (2012).

69. Laskar, M. R. *et al.* Large area single crystal (0001) oriented MoS<sub>2</sub>. *Applied Physics Letters* **102**, 252108 (2013).
70. Lee, Y.-H. *et al.* Synthesis and transfer of single-layer transition metal disulfides on diverse surfaces. *Nano letters* **13**, 1852–7 (2013).
71. Lee, Y.-H. *et al.* Synthesis of large-area MoS<sub>2</sub> atomic layers with chemical vapor deposition. *Advanced materials (Deerfield Beach, Fla.)* **24**, 2320–5 (2012).
72. Mann, J. *et al.* Facile growth of monolayer MoS<sub>2</sub> film areas on SiO<sub>2</sub>. *The European Physical Journal B* **86**, 226 (2013).
73. Najmaei, S. *et al.* Vapour phase growth and grain boundary structure of molybdenum disulphide atomic layers. *Nature materials* **12**, 754–9 (2013).
74. Zhou, L. *et al.* Large-Area Synthesis of High-Quality Uniform Few-Layer MoTe<sub>2</sub>. *Journal of the American Chemical Society* **137**, 11892–11895 (2015).
75. Hofmann, W. K. Thin films of molybdenum and tungsten disulphides by metal organic chemical vapour deposition. *Journal of Materials Science* **23**, 3981–3986 (1988).
76. Chung, J.-W., Dai, Z. R. & Ohuchi, F. S. WS<sub>2</sub> thin films by metal organic chemical vapor deposition. *Journal of Crystal Growth* **186**, 137–150 (1998).
77. Lee, W. Y., Besmann, T. M. & Stott, M. W. Preparation of MoS<sub>2</sub> thin films by chemical vapor deposition. *Journal of Materials Research* **9**, 1474–1483 (2011).



78. Imanishi, N. Synthesis of MoS<sub>2</sub> Thin Film by Chemical Vapor Deposition Method and Discharge Characteristics as a Cathode of the Lithium Secondary Battery. *Journal of The Electrochemical Society* **139**, 2082 (1992).
79. Li, X.-L., Ge, J.-P. & Li, Y.-D. Atmospheric pressure chemical vapor deposition: an alternative route to large-scale MoS<sub>2</sub> and WS<sub>2</sub> inorganic fullerene-like nanostructures and nanoflowers. *Chemistry (Weinheim an der Bergstrasse, Germany)* **10**, 6163–71 (2004).
80. Carmalt, C. J., Parkin, I. P. & Peters, E. S. Atmospheric pressure chemical vapour deposition of WS<sub>2</sub> thin films on glass. *Polyhedron* **22**, 1499–1505 (2003).
81. Boscher, N. D., Carmalt, C. J., Palgrave, R. G., Gil-Tomas, J. J. & Parkin, I. P. Atmospheric Pressure CVD of Molybdenum Diselenide Films on Glass. *Chemical Vapor Deposition* **12**, 692–698 (2006).
82. Eichfeld, S. M. *et al.* Highly scalable, atomically thin WSe<sub>2</sub> grown via metal-organic chemical vapor deposition. *ACS nano* **9**, 2080–7 (2015).
83. Kuech, T. F. Low Temperature CVD Growth of Epitaxial HgTe on CdTe. *Journal of The Electrochemical Society* **128**, 1142 (1981).
84. Das, S., Robinson, J. A., Dubey, M., Terrones, H. & Terrones, M. Beyond Graphene: Progress in Novel Two-Dimensional Materials and van der Waals Solids. *Annual Review of Materials Research* **45**, 150514142752001 (2014).
85. Wagner, C. D. & Joshi, A. The auger parameter, its utility and advantages: a review. *Journal of Electron Spectroscopy and Related Phenomena* **47**, 283–313 (1988).
86. Powell, C. J. Recommended Auger parameters for 42 elemental solids. *Journal of*

*Electron Spectroscopy and Related Phenomena* **185**, 1–3 (2012).

87. NIST X-ray Photoelectron Spectroscopy (XPS) Database, Version 3.5. at  
<<http://srdata.nist.gov/xps/>>
  
88. Moulder, J. F. *Handbook of X-ray Photoelectron Spectroscopy*. (Physical Electronics Division, Perkin-Elmer Corp., 1993). at  
<<http://doi.wiley.com/10.1002/sia.740030412>>
  
89. Refson, K. Variational density-functional perturbation theory for dielectrics and lattice dynamics. *Physical Review B* **73**, 155114 (2006).
  
90. Schroder, D. K. *Semiconductor Material and Device Characterization, 3rd version*. (Wiley-IEEE Press, 2006).  
doi:<http://dx.doi.org.ezaccess.libraries.psu.edu/10.1002/0471749095>
  
91. Callister, W. D. & Rethwisch, D. G. *Materials Science and Engineering: An Introduction*. (Wiley Global Education, 2010). at  
<<http://www.wiley.com/WileyCDA/WileyTitle/productCd-EHEP000300.html>>
  
92. Brixner, L. H. Preparation and properties of the single crystalline AB<sub>2</sub>-type selenides and tellurides of niobium, tantalum, molybdenum and tungsten. *Journal of Inorganic and Nuclear Chemistry* **24**, 257–263 (1962).
  
93. Augustin, J. *et al.* Electronic band structure of the layered compound Td-WTe<sub>2</sub>. *Physical Review B* **62**, 10812–10823 (2000).
  
94. Ali, M. N. *et al.* Large, non-saturating magnetoresistance in WTe<sub>2</sub>. *Nature* **514**, 205–208 (2014).

95. Vinogradov, A. V., Lomonov, V. A., Pershin, Y. A. & Sizova, N. L. Growth and some properties of TeO<sub>2</sub> single crystals with a large diameter. *Crystallography Reports* **47**, 1036–1040 (2002).
96. Mentzen, B. F. & Sienko, M. J. Preparation and x-ray study of mixed-anion tungsten dichalcogenides. *Inorganic Chemistry* **15**, 2198–2202 (1976).
97. The International Centre for Diffraction Data - ICDD - a non-profit scientific organization dedicated to collecting, editing, publishing, and distributing powder diffraction data. at <<http://www.icdd.com/>>
98. *International Tables for Crystallography*. **D**, (International Union of Crystallography, 2013).
99. Clark, S. J. *et al.* First principles methods using CASTEP. *Zeitschrift für Kristallographie* **220**, 567–570 (2005).
100. Giannozzi, P. *et al.* QUANTUM ESPRESSO: a modular and open-source software project for quantum simulations of materials. *Journal of physics. Condensed matter : an Institute of Physics journal* **21**, 395502 (2009).
101. Perdew, J. P. Self-interaction correction to density-functional approximations for many-electron systems. *Physical Review B* **23**, 5048–5079 (1981).
102. Turkowski, V., Kabir, A., Nayyar, N. & Rahman, T. S. Dynamical mean-field theory for molecules and nanostructures. *The Journal of chemical physics* **136**, 114108 (2012).
103. Grimme, S. Semiempirical GGA-type density functional constructed with a long-range dispersion correction. *Journal of computational chemistry* **27**, 1787–99 (2006).

104. Ortmann, F., Bechstedt, F. & Schmidt, W. Semiempirical van der Waals correction to the density functional description of solids and molecular structures. *Physical Review B* **73**, 205101 (2006).
105. Bromley, R. A., Murray, R. B. & Yoffe, A. D. The band structures of some transition metal dichalcogenides. III. Group VIA: trigonal prism materials. *Journal of Physics C: Solid State Physics* **5**, 759–778 (1972).
106. Brown, B. E. The crystal structures of NbTe<sub>2</sub> and TaTe<sub>2</sub>. *Acta Crystallographica* **20**, 264–267 (1966).
107. Kohn, W. & Sham, L. J. Self-Consistent Equations Including Exchange and Correlation Effects. *Physical Review* **140**, A1133–A1138 (1965).
108. Yu, Y. *et al.* Controlled scalable synthesis of uniform, high-quality monolayer and few-layer MoS<sub>2</sub> films. *Scientific reports* **3**, 1866 (2013).
109. Gutiérrez, H. R. *et al.* Extraordinary Room-Temperature Photoluminescence in Triangular WS<sub>2</sub> Monolayers. *Nano letters* **13**, 3447–54 (2013).
110. Huang, J.-K. *et al.* Large-Area Synthesis of Highly Crystalline WSe<sub>2</sub> Monolayers and Device Applications. *ACS nano* (2013). doi:10.1021/nn405719x
111. Jayatissa, A. H., Dadi, A. & Aoki, T. Nanocrystalline WO<sub>3</sub> films prepared by two-step annealing. *Applied Surface Science* **244**, 453–457 (2005).
112. Brooks, L. S. The Vapor Pressures of Tellurium and Selenium. *Journal of the American Chemical Society* **74**, 227–229 (1952).

113. Park, J. C. *et al.* Phase-Engineered Synthesis of Centimeter-Scale 1T'- and 2H-Molybdenum Ditelluride Thin Films. *ACS Nano* **9**, 6548–6554 (2015).
114. Gunn, S. R. The Heats of Formation of H<sub>2</sub>Se and H<sub>2</sub>Te. Correlations of Simple Covalent Hydrides 1. *The Journal of Physical Chemistry* **68**, 949–952 (1964).
115. Text-book of inorganic chemistry. Edited by J. Newton Friend, D.Sc., Ph.D., F.I.C. Vol. VII. Part II. Sulphur, Selenium, and Tellurium. By R. H. Vallance, M.Sc., F.I.C., D.F. Twiss, D.Sc., F.I.C., and Miss A. R. Russell, B.Sc., A.I.C. Pp. xxviii + 420. Lo. *Journal of the Society of Chemical Industry* **50**, 713–713 (1931).
116. Usta, M., Kahraman, S., Bayansal, F. & Çetinkara, H. a. Effects of annealing on morphological, structural and electrical properties of thermally evaporated WO<sub>3</sub> thin films. *Superlattices and Microstructures* **52**, 326–335 (2012).
117. Ma, Y.-R., Lin, C.-M., Yeh, C.-L. & Huang, R.-T. Synthesis and characterization of one-dimensional WO<sub>2</sub> nanorods. *Journal of Vacuum Science & Technology B: Microelectronics and Nanometer Structures* **23**, 2141 (2005).
118. Cai, P. L. *et al.* Drastic Pressure Effect on the Extremely Large Magnetoresistance in WTe<sub>2</sub>: Quantum Oscillation Study. *Physical Review Letters* **115**, 057202 (2015).
119. Kang, D. *et al.* Superconductivity emerging from a suppressed large magnetoresistant state in tungsten ditelluride. *Nature communications* **6**, 7804 (2015).
120. Alekseev, P. S. *et al.* Magnetoresistance in two-component systems. (2014). at <<http://arxiv.org/abs/1410.4982>>
121. Thoutam, L. R. *et al.* Temperature-Dependent Three-Dimensional Anisotropy of

the Magnetoresistance in WTe 2. *Physical Review Letters* **115**, 046602 (2015).

122. Lv, H. Y. *et al.* Perfect charge compensation in WTe 2 for the extraordinary magnetoresistance: From bulk to monolayer. *EPL (Europhysics Letters)* **110**, 37004 (2015).
123. Eda, G. *et al.* Photoluminescence from chemically exfoliated MoS<sub>2</sub>. *Nano letters* **11**, 5111–6 (2011).
124. Voiry, D., Mohite, A. & Chhowalla, M. Phase engineering of transition metal dichalcogenides. *Chem. Soc. Rev.* **44**, 2702–2712 (2015).
125. Eda, G. *et al.* Coherent atomic and electronic heterostructures of single-layer MoS<sub>2</sub>. *ACS nano* **6**, 7311–7 (2012).
126. Fan, X. *et al.* Fast and Efficient Preparation of Exfoliated 2H MoS<sub>2</sub> Nanosheets by Sonication-Assisted Lithium Intercalation and Infrared Laser-Induced 1T to 2H Phase Reversion. *Nano letters* **15**, 5956–60 (2015).
127. Cheng, Y. *et al.* Origin of the phase transition in lithiated molybdenum disulfide. *ACS nano* **8**, 11447–53 (2014).